UNIVERSITY OF BELGRADE

FACULTY OF TECHNOLOGY AND METALLURGY

Gordana D. Marković

DEVELOPMENT AND DESIGN OF NEW TITANIUM ALLOYS USING ADVANCED COMPUTATIONAL METHODS

Doctoral Dissertation

Belgrade, 2026.

УНИВЕРЗИТЕТ У БЕОГРАДУ

ТЕХНОЛОШКО-МЕТАЛУРШКИ ФАКУЛТЕТ

Гордана Д. Марковић

РАЗВОЈ И ДИЗАЈН НОВИХ ЛЕГУРА ТИТАНА ПРИМЕНОМ НАПРЕДНИХ РАЧУНАРСКИХ МЕТОДА

докторска дисертација

Београд, 2026.

Supervisors:

_____

Dr Vaso Manojlović, Associate Professor,

University of Belgrade, Faculty of Technology and Metallurgy

_____

Dr Jovana Ružić, Senior Research Associate,

University of Belgrade, Vinča Institute of Nuclear Sciences

Members of Committee:

_____

Dr. Željko Kamberović, Full Professor
University of Belgrade, Faculty of Technology and Metallurgy

_____

Dr Stefan Dikić, Assistant Professor,

University of Belgrade, Faculty of Technology and Metallurgy

_____

Dr Gvozden Jovanović, Research Associate
Institute for Technology of Nuclear and Mineral Raw Materials, Belgrade

_____

Dr Francisco Javier Dominguez Gutierrez, Associate Professor

National Centre For Nuclear Research (NCBJ), Otwock, Poland

Date: _____

Candidate:

Gordana D. Marković

Acknowledgements

First and foremost, I would like to express my sincere gratitude to my supervisors, Dr Vaso Manojlović and Dr Jovana Ružić, for their guidance, support, and trust throughout my doctoral research. I am particularly grateful to Dr Vaso Manojlović for his help with the development and application of machine learning methods, and to Dr Jovana Ružić for her support in planning and carrying out the experimental part of this work.

I am especially grateful to Dr Francisco Javier Dominguez Gutierrez for his continuous scientific support throughout my doctoral research, his invaluable help with molecular dynamics simulations and their interpretation, and for the many discussions, suggestions, and insights that helped connect the different parts of this work.

I would like to thank Dr Gvozden Jovanović for his help with quantitative analysis, his careful review of the dissertation, and his valuable suggestions. I am also grateful to the members of the committee, Dr Željko Kamberović, Dr Stefan Dikić, Dr Gvozden Jovanović, and Dr Francisco Javier Dominguez Gutierrez, for their time, comments, and suggestions, which contributed to the final form of this dissertation.

I gratefully acknowledge the Institute for Technology of Nuclear and Other Mineral Raw Materials in Belgrade for its institutional support and the Ministry of Science, Technological Development and Innovation of the Republic of Serbia for supporting my research. Part of this research was carried out during a research stay in Warsaw supported by COST Action CA21121 – European Network for the Mechanics of Matter at the Nano-Scale. I am particularly grateful to Dr Łukasz Kurpaska for hosting my research stay and for his support and valuable contribution to this work.

I would also like to express my sincere gratitude to the colleagues who supported me throughout different stages of this research: Dr Iwona Jóźwik for her assistance with EBSD analysis; Dr Kamil Cichocki, Dr Krzysztof Muszka, and Dr Krzysztof Pajor for their help with alloy processing; and Dr Karol Frydrych for his assistance with the preparation of phase diagrams. Their expertise, support, and willingness to help contributed greatly to the completion of this work.

Finally, I would like to thank my parents, Jelena and Dragan, my sister Zorica, my husband Aleksa, and my dear friend Jelena for their love, patience, understanding, and unconditional support throughout all the years that led to this dissertation.

Abstract

The development of titanium alloys with reduced Young's modulus similar to the bone's modulus is an important challenge in metallic biomaterials, as the stiffness mismatch between an implant and bone can contribute to bone resorption. This research work is focused on the use of machine learning to predict low-modulus titanium alloys, followed by experimental validation of selected compositions.

A literature-based database of biocompatible titanium alloys was compiled to model Young's modulus, yield strength, and ultimate tensile strength. The Young's modulus model was based on 240 experimental records. With validation grouped by source publication, the Random Forest model achieved a coefficient of determination of 0.417 and a mean absolute error of 11.50 GPa, with d-orbital energy and β-phase stability descriptors showing the highest importance.

Based on the predictions, Ti–6.2Mo–xSn (x = 5, 10 and 15 wt.%) alloys were produced by arc melting and experimentally characterized. The alloys exhibited high relative density, homogeneous composition, and predominantly α-lamellar microstructure. The Young's modulus decreased from 101.02 GPa for Ti–6.2Mo to 79.26, 85.31, and 83.65 GPa with 5, 10, and 15 wt.% Sn, respectively. Nanoindentation, microstructural analysis, atomistic simulations, and thermodynamic calculations were used to obtain and analyse the results.

Obtained results demonstrate that machine learning can guide the selection of low-modulus titanium alloys, while their final properties also depend on microstructure and processing.

Keywords: titanium alloys; Ti–Mo–Sn alloy design; machine learning; nanoindentation; Young's modulus; α-lamellar microstructure.

Scientific field: Technical Sciences

Scientific subfield: Metallurgical engineering

Сажетак

Развој легура титана са Јанговим модулом еластичности који је приближан модулу еластичности кости представља значајан изазов у области металних биоматеријала, јер разлика у крутости између импланта и кости може допринети ресорпцији коштаног ткива. У овој студији испитана је примена машинског учења за предвиђање легура титана са одговарајућим модулом еластичности, након чега су одабрани састави експериментално потврђени.

На основу података из литературе формирана је база биокомпатибилних легура титана за моделовање Јанговог модула, границе течења и затезне чврстоће. Модел Јанговог модула заснован је на 240 експерименталних записа. При провери модела, у којој су подаци груписани према доступним публикацијама, модел случајних шума остварио је коефицијент детерминације од 0,417 и средњу апсолутну грешку од 11,50 GPa, при чему су највећи значај имали енергија d-орбитале и дескриптори стабилности β фазе.

На основу предвиђања изабране су легуре Ti–6,2Mo–xSn (x = 5, 10 и 15 мас.%), добијене електролучним топљењем. Легуре су имале високу релативну густину, хомоген састав и претежно α-ламеларну микроструктуру. Јангов модул снижен је са 101,02 GPa за Ti–6,2Mo на 79,26, 85,31 и 83,65 GPa за легуре са 5, 10 и 15 мас.% Sn. Наноиндентација, анализа микроструктуре, атомистичке симулације и термодинамички прорачуни коришћени су за добијање и тумачење резултата.

Добијени резултати показују да машинско учење може усмерити избор легура титана са Јанговим модулом еластичности приближним Јанговом модулу еластичности кости, док њихова коначна својства зависе и од микроструктуре и поступка израде.

Кључне речи: легуре титана; Ti–Mo–Sn систем; машинско учење; наноиндентација; Јангов модул; α-ламеларна микроструктура.

Научна област: Техничке науке

Ужа научна област: Металуршко инжењерство

Content

1. Introduction

1.1 Titanium as a biomaterial

Titanium has been used in medicine since the 1950s, and demand has risen in recent decades (Sarraf et al., 2022). It is used to replace damaged tissue, ranging from dental components to large structural components used in hip or knee replacements (Marin and Lanzutti 2023) (Figure 1.1). The material must be capable of withstanding mechanical stress for several decades and maintaining safe contact with the biological system in which it is situated (Sivakumar et al., 2026).

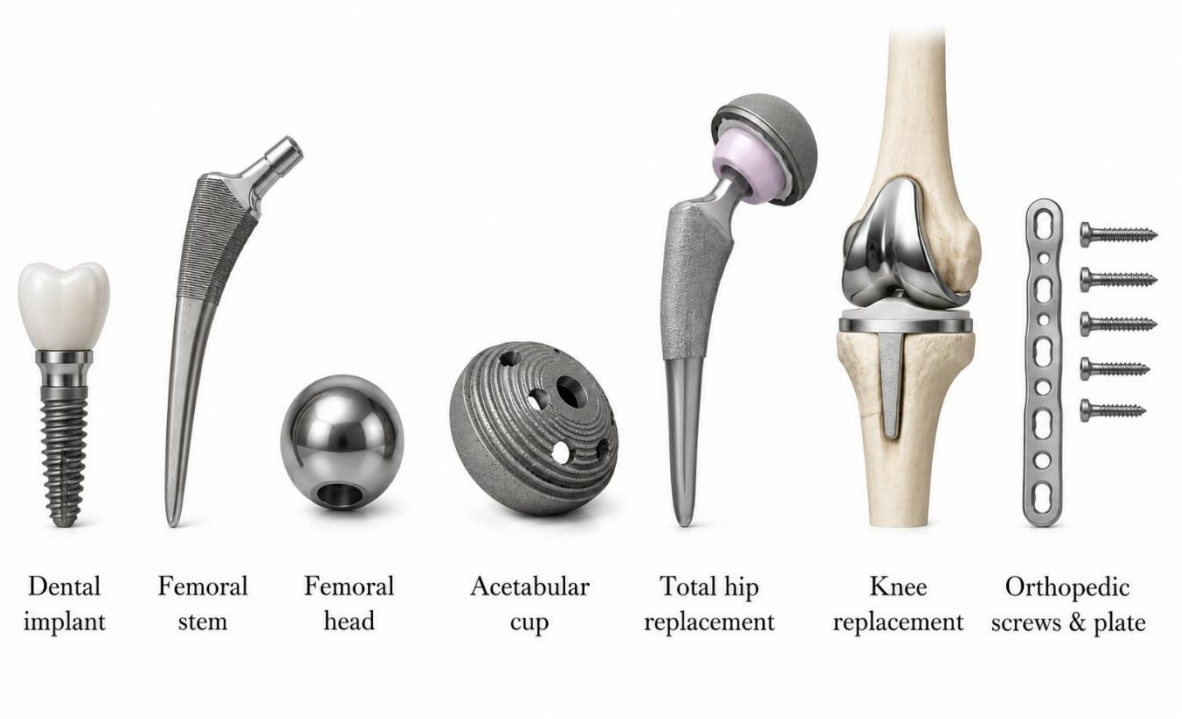

Figure 1.1. Examples of titanium-based medical implants used in dental and orthopedic applications.

Various types of materials have been tested for this purpose over time. Polymers and ceramics have proven to be excellent biomaterials in a variety of applications, but their performance under load-bearing conditions is inadequate (Vaiani et al., 2023). The most pronounced requirement in these conditions is the combination of strength and stiffness (Spataru et al., 2024). Among metallic materials, stainless steel and cobalt-chromium alloys were among the first to be used for orthopedic implants (Marin and Lanzutti 2025). Over time, certain problems have been identified, including higher stiffness than bone and the release of metal ions into the surrounding environment (Mohapatra et al., 2025).

The biggest advantage of titanium and its alloys is the exceptional balance of properties. They have an excellent strength-to-density ratio, very good corrosion resistance, and a significantly lower Young's modulus compared to all the previously stated material groups (Leyens and Peters 2006). When exposed to air or body fluids, an oxide layer forms spontaneously on the surface and remains stable under most conditions. This is one of the reasons titanium alloys retain their functionality over a long period. Of course, this barrier is not absolute and can be compromised under certain conditions (Bocchetta et al., 2021). More on this will be discussed in the following chapters.

Despite the significant advantages over the previously mentioned materials, there is still a need to further improve their properties. The Ti-6Al-4V alloy, the predominantly used titanium alloy in biomedical applications, has shown some limitations. Its Young's modulus remains elevated in comparison to that of bone (Niinomi and Nakai 2011). There is also concern about the release of aluminum and vanadium, which have been associated with various health issues (Siemers et al.,

2018). These limitations motivate the development of new titanium alloys with more desirable properties and represent one of the main driving forces behind this work.

1.2 Biocompatibility and corrosion resistance

Biocompatibility is one of the basic requirements for biomaterials. It describes how the material behaves in contact with biological tissue over a long period of time (Niinomi and Nakai 2011). There are 5 criteria established by the International Standards Organization that an implant must meet: non-toxic, non-thrombogenic, non-carcinogenic, non-antigenic, and non-mutagenic (Huzum et al., 2021; Ratner, 2001; Markovic et al., 2023). Whether the material meets these requirements depends on many factors, including the material's composition, the surface in direct contact with tissues, and the environment in which the implant is placed (Ratner 2001). Body fluids contain water, dissolved oxygen, proteins, and many other ions, such as the ever-present chloride ions, which are associated with increased corrosion. It is important to note that corrosion is difficult to avoid entirely with metallic biomaterials. Various electrochemical and biological processes occur on the surface under constant, cyclical mechanical loading. Even the slightest corrosion can cause ion release, with negative effects that only become apparent after many years (Eliaz 2019).

Titanium and its alloys perform well in this respect, mainly because of the thin oxide layer that forms on the surface, which is mainly composed of TiO_2 (Wheelis et al. 2018). This layer forms spontaneously and tends to remain stable under most conditions. If locally damaged, it reforms. Titanium is therefore more accurately described as corrosion-resistant, since complete immunity to corrosion cannot be expected in physiological environments (Oliveira and Guastaldi, 2008; Tsuchiya et al., 2022; Kotsakis et al., 2024; Shemtov-Yona et al., 2025). This distinction is important because the protective oxide layer can be compromised by mechanical loading or by local environmental conditions that differ from those in the surrounding bulk fluid.

Such conditions can develop, for example, in small gaps between implant components or other confined geometries. In the chloride-containing environment of body fluids, local breakdown of the passive film can lead to pitting and crevice corrosion, particularly at modular junctions (Apaza-Bedoya et al., 2017; Eliaz, 2019; Chen et al., 2023). When mechanical loading and corrosion act simultaneously, repeated micromotion can further disrupt the passive layer and accelerate metal ion release, a process known as tribocorrosion (Gaur et al., 2022). Thus, despite the generally high corrosion resistance of titanium, the long-term behavior of an implant also depends on its composition and on the elements that may be released when the protective surface layer is disturbed.

In this context, the role of alloying elements should also be considered. Alloying is necessary from a mechanical standpoint, but it introduces additional variables in terms of biological response (Niinomi 2008). Not all elements behave in the same way under physiological conditions. Vanadium, which is part of the widely used Ti–6Al–4V alloy, is considered toxic in its elemental form and in some of its oxide states, while aluminum has been associated with neurological effects after prolonged exposure (Gomes et al. 2011). As a result, the alloying elements used in biomedical titanium alloys are now classified according to their physiological impact. Depending on their biological response, elements can be broadly grouped as non-cytotoxic, cytotoxic, or neutral (Table 1.1) (Liang 2020). This classification has become one of the key criteria in biomedical titanium alloy design, together with mechanical performance. These factors guided the selection of alloying elements in the present work.

Table 1.1. Titanium alloying elements classification according to biological response (Liang 2020).

Category	Elements
Non-cytotoxic	Ti, Nb, Zr, Ta, Sn, Mo
Cytotoxic	V, Al, Ni, Co, Cu, Cr
Neutral	Fe, Mn, W

Biocompatibility is often discussed primarily in terms of chemical stability, but this is only part of the picture. The selection of alloying elements must simultaneously account for their biological response and their influence on mechanical behavior. Conventional alloys such as Ti–6Al–4V illustrate this compromise well. Owing to its good corrosion resistance and favorable strength, Ti–6Al–4V has a long clinical record in load bearing orthopedic devices, such as hip and knee endoprosthesis components and bone plates, as well as in dental implants. Nevertheless, two concerns remain. The first is biological and relates to the potential toxicity of aluminum and vanadium ions released during long term exposure to the physiological environment. The second is mechanical: its Young's modulus is significantly higher than that of bone, which can lead to stress shielding and long term complications, as discussed in Section 1.3.

Therefore, the design of new biomedical titanium alloys requires simultaneous control of biological response, corrosion resistance and mechanical compatibility. This has shifted attention toward Ti-based systems containing elements such as Nb, Zr, Ta, Mo and Sn, which combine acceptable biological response with the possibility of reducing elastic modulus.

1.3 Mechanical compatibility and stress shielding

The mechanical requirements for an orthopedic implant are not limited to sufficient strength against fracture. The implant must also have an elastic stiffness compatible with bone, because excessive mismatch in Young’s modulus changes the load transfer between the implant and surrounding tissue. Therefore, a material may be strong enough to withstand mechanical loading, but still cause long-term complications if its Young’s modulus is substantially higher than that of the bone it replaces (Chmielewska and Dean 2024).

Bone is not a uniform material. Its stiffness varies between cortical and trabecular regions and depends on the direction of loading due to its anisotropic structure (Limzider et al. 2025). Cortical bone, which is the primary structural component of long bones and the tissue most directly affected in hip and knee arthroplasty, has an elastic modulus in the range of 10 to 30 GPa (Beisekenov et al., 2025). When a metallic implant with much higher stiffness is placed in contact with bone, the load is no longer distributed as it would be in healthy tissue. The implant takes over a larger share of the mechanical load, and the bone around it is exposed to less stress than it normally experiences (Paul et al., 2026). According to Wolff's law, reduced mechanical stimulation around a stiff implant promotes bone remodeling and may gradually result in local bone resorption (Frost 1994). Over time, this leads to a loss of bone mass around the implant, compromising fixation stability and may potentially lead to aseptic loosening. This is one of the leading causes of long-term implant failure (Frost 1994; Paul et al., 2026). A schematic representation of stress shielding and the resulting bone resorption around the implant is shown in Figure 1.2.

The extent of stress shielding depends on how large the difference in Young’s modulus actually is. Looking at the values reported for common orthopedic materials, the gap is substantial. Cobalt-chromium alloys reach around 200-253 GPa (Fratila et al., 2023; Smith et al., 2024), stainless steel 316L around 214 GPa (Luo et al., 2018). Titanium alloys are lower, but the distance from cortical bone (10-30 GPa) is still far from negligible. Commercially pure titanium has a modulus of approximately ~103–105, and Ti-6Al-4V, the most widely used titanium alloy in orthopedics, has a

modulus of approximately 110 GPa (Niinomi and Nakai 2011). Even at these values, the mismatch with cortical bone remains three to ten times higher, depending on the reference.

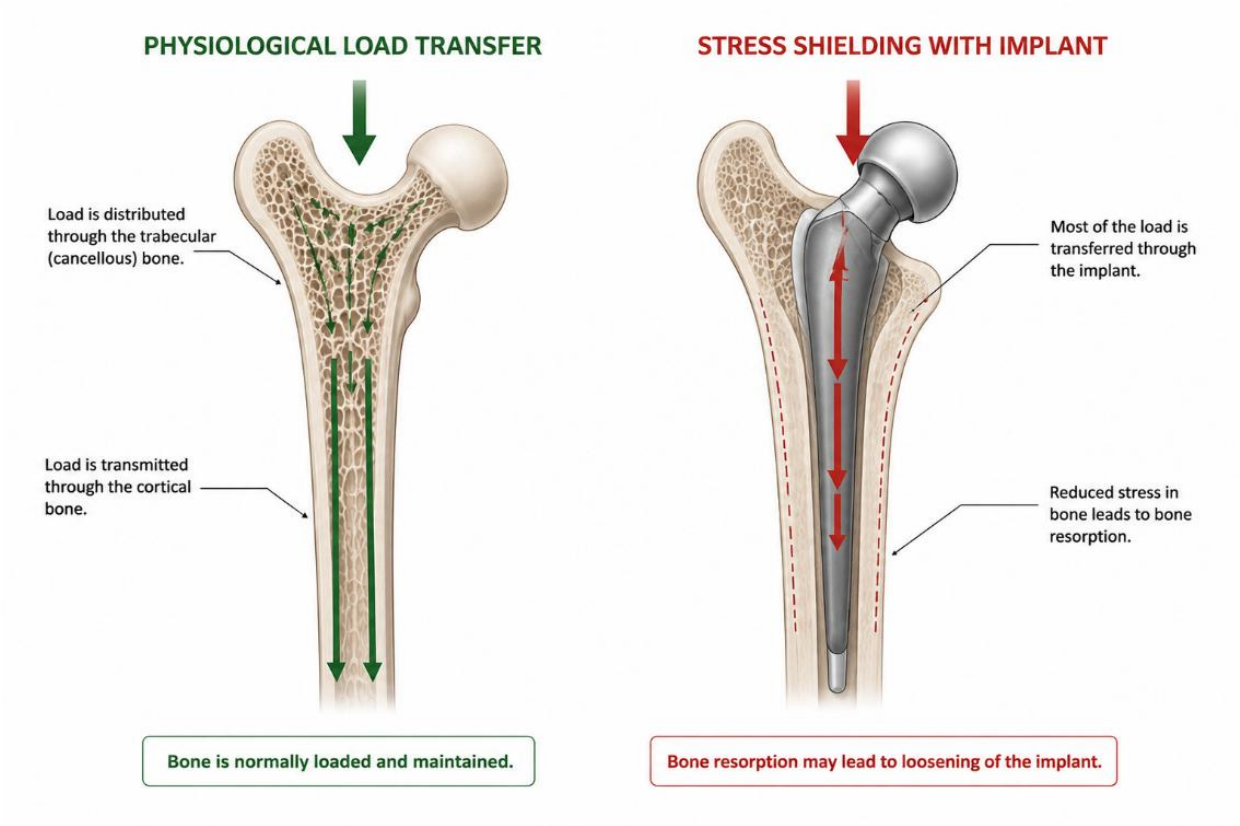

Figure 1.2. Schematic illustration of stress shielding around a metallic implant and the resulting bone resorption.

The most direct way to reduce the mismatch is to bring the implant's Young's modulus close to that of bone (Niinomi and Nakai 2011). Generally, β-type titanium alloys exhibit lower Young's modulus than α or α+β alloys because the body-centered cubic structure is mechanically less stiff than the hexagonal close-packed one. This is one of the main directions in current research on titanium alloys for biomedical applications, and it provides the context for the present work. However, predicting which compositions will produce a reduced Young's modulus remains complex, especially in multicomponent titanium alloys, where phase stability and mechanical behavior result from the combined influence of alloy chemistry, processing history and microstructural evolution. These relationships are discussed in more detail in the following chapters.

1.4 Motivation for low-modulus alloys design

The main motivation for developing low-modulus titanium alloys is to reduce the stiffness mismatch between metallic implants and bone, which is the primary cause of the stress shielding described in the previous section. Even the most widely used titanium alloys are still several times stiffer than cortical bone. Reducing their elastic modulus further, without sacrificing strength, corrosion resistance, or biocompatibility, remains an important goal in biomedical alloy design.

One major direction toward this goal is the design of metastable β-type compositions, since β-Ti alloys generally exhibit lower elastic modulus than α and α+β alloys. However, the final modulus is not controlled by phase constitution alone, but also by alloy chemistry, processing history, microstructure, texture and possible transformation mechanisms. Nb, Mo, Zr, Ta, and Sn have all been examined from this angle, with mixed results when both stiffness and strength are considered.

Progress in this area has not been straightforward. Lowering the Young's modulus often reduces strength, and the relationships among composition, phase stability, and resulting properties

are not always easy to predict. This becomes even more pronounced in ternary systems. The combined effect of multiple alloying elements on the titanium matrix is not simply additive, and trends observed in binary alloys do not necessarily carry over once a third element is introduced. As a result, relying solely on experimental exploration quickly becomes inefficient. Machine learning offers a different approach to this problem. Applied to titanium alloy databases, this kind of model can point toward compositions worth investigating, ones that are predicted to show a lower elastic modulus, prior to experimental synthesis. The experimental work still has to happen, but it starts from a more informed position.

Among the possible low-modulus systems, alloys that combine a β-stabilizer with a nominally neutral element are of particular interest, because their behavior cannot be predicted from binary data alone. Ti–Mo–Sn is one such system: Mo is a well-established β-stabilizer, while Sn is usually classified as neutral and has no known cytotoxic effects. The combined effect of Mo and Sn on phase stability and elastic modulus in the ternary system, however, is not obvious from the individual Ti–Mo and Ti–Sn binaries. Some studies suggest that Sn does not behave as strictly neutral and may contribute to β stabilization and alter transformation pathways when combined with Mo (Li et al., 2023). Systems of this type remain difficult to predict, which makes the relationship between composition and elastic modulus in such alloys one of the open questions that motivate the modelling and experimental work presented in the following chapters.

1.5 Scope and objectives

The objective of this research is to develop and experimentally validate a predictive approach for the design of new titanium alloys with reduced Young's modulus and potential biomedical applications. The central aim is to support the selection of alloy compositions that can reduce the stiffness mismatch between metallic implants and bone, while retaining the advantages of titanium-based biomaterials.

To this end, the work combines materials-informatics tools with experimental validation. Machine-learning models are used to relate alloy composition and composition-derived descriptors to the main mechanical properties, with Young's modulus as the primary target. The models are then applied to explore multicomponent composition spaces and to identify candidate regions associated with a lower predicted elastic modulus.

The experimental part of the work tests whether computationally selected compositions show the expected mechanical behavior, and examines how phase constitution, microstructure and crystallographic features influence the measured elastic behavior. In this way, the thesis evaluates the predictive ability of the models and, at the same time, highlights the limitations of composition-based alloy design when microstructural effects are not explicitly included.

The remainder of the study is organized as follows. Chapter 2 (Background and literature review) covers the metallurgical background and the existing approaches to titanium alloy design. Chapter 3 (Materials and methods) describes the construction of the alloy database, the machine-learning methodology and the experimental procedures. (Results and discussion) presents the predictive models, the selection of candidate compositions and their experimental characterization, together with the interpretation of the obtained results. Chapter 5 (Conclusions) summarizes the main findings and outlines directions for future work.

2. Background and literature review

2.1 Crystal structure and phase transformations in titanium

2.1.1 α and β phases of titanium

Under atmospheric pressure, pure titanium exists in two main equilibrium forms. At room temperature it is stable as the α phase, with a hexagonal close-packed (HCP) structure and a c/a ratio of approximately 1.587, slightly below the ideal value of 1.633 (Farrokhi 2026; Fan 2016). Above approximately 882 °C it transforms into the β phase, with a body-centered cubic (BCC) structure, which persists up to the melting point (McQuillan 1949; Lütjering and Williams 2003). This transformation temperature, known as the β-transus, is a key parameter in titanium alloy processing and phase-stability control (Seagle 2019). In titanium alloys, additional metastable phases may also appear depending on composition and processing history.

The two structures differ significantly in their mechanical behaviour. The BCC β phase provides a larger number of potential slip systems and is therefore generally more ductile than the HCP α phase, whose plastic deformation is more orientation-dependent because fewer slip systems are easily activated (Lütjering and Williams 2003). The β phase can also exhibit a lower Young's modulus, particularly in metastable β titanium alloys. These crystallographic differences form the basis for understanding the relationship between phase constitution, processing history and mechanical properties in titanium alloys, and they are one reason why β-stabilized compositions are of particular interest for low-modulus alloy design. The main crystallographic differences between α- and β-titanium are shown schematically in Figure 2.1 (Quan et al., 2017).

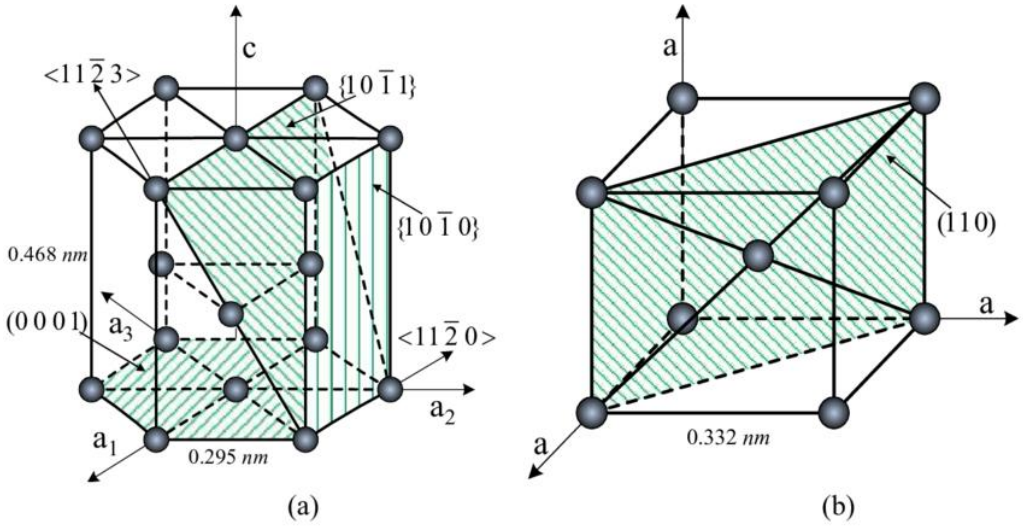

Figure 2.1. Schematic representation of α-Ti (HCP) and β-Ti (BCC) crystal structures with their characteristic slip systems. The larger number of available slip systems in the β phase contributes to its greater capacity for plastic deformation compared with α phase (Quan et al., 2017).

2.1.2 β-transus temperature and phase stability

The α↔β transformation temperature introduced in the previous section represents the β-transus of pure titanium. In alloys, this temperature changes with chemical composition and becomes one of the main indicators of phase stability. For this reason, the β-transus is used to evaluate how alloying elements and thermal history influence the final phase constitution after processing.

Because of that, the temperature of 882°C is more than just a physical constant. It serves as the starting point for understanding phase stability in all titanium alloys. The role of each alloying element in titanium alloys is commonly discussed through its influence on the β-transus temperature, either by stabilizing the α phase or by extending the stability range of the β phase.

The transformation between α and β is reversible, but the final microstructure after cooling does not depend only on temperature. Cooling rate also matters. During slow cooling, the transformation is diffusion-controlled and the new α phase forms gradually inside the parent β grains, following the Burgers orientation relationship (Shang et al., 2024). With rapid quenching, diffusion is suppressed. Depending on alloy composition, the high-temperature β phase may either be retained as metastable β or transform martensitically to α′ or α" phases (Bignon et al., 2021).

Martensitic products formed during rapid cooling preserve a crystallographic relationship with the parent β phase, but their distorted lattice and metastable character can lead to mechanical behavior that differs from equilibrium α-Ti. Because of that, two alloys with the same nominal composition can still show different phase distributions and different elastic responses if their thermal histories are not the same.

The β-transus therefore depends strongly on alloy composition rather than being a fixed material constant (Reddy et al., 2014). Elements that raise the β-transus stabilize the α phase to higher temperatures, while those that lower it expand the β phase field toward room temperature and make β retention after cooling more likely (Seagle 2019). Neutral elements usually have a smaller direct influence on the transus itself, although they can still affect phase stability indirectly through their interaction with other alloying elements (Nnamchi and Obayi 2020).

In practice, this means that the final phase constitution cannot be predicted only from composition or only from processing conditions. Both have to be considered together. Small differences in alloy chemistry or cooling conditions are often enough to change whether the final structure is α, α+β, metastable β, or martensitic α′.

2.1.3 Role of alloying elements (α-, β-stabilizers and neutral elements)

Alloying elements in titanium are classified according to their effect on the β-transus temperature. Those that raise it stabilize α phase, those that lower it stabilize the β phase, while a third group has comparatively little effect on the transformation temperature itself (Kolli and Devaraj 2018). The main α-stabilizing, β-stabilizing, and neutral alloying elements are summarized in Table 2.1. Although this classification is useful for understanding the general role of individual alloying elements, it is primarily based on binary Ti systems and does not fully capture the more complex interactions that emerge in multicomponent alloys. The characteristic effects of these groups on phase stability and phase boundaries in binary Ti systems are illustrated schematically in Figure 2.2.

Table 2.1. Classification of alloying elements in titanium alloys (Markovic et al., 2023).

***α*-stabilizers**	**Neutral stabilizers**	***β*-stabilizers**
Al, O, N, C, Ga	Sn, Zr, Hf,	Mo, V, Nb, Ta, Fe, Cr, Mn, Ni, Co, W

Alpha-stabilizing elements extend α phase field to higher temperatures. Aluminum is the most important of these, and it is present in a large fraction of commercial titanium alloys, including Ti-6Al-4V (Beese, 2018). Interstitial elements such as oxygen, nitrogen, and carbon also belong to this category and are strong stabilizers even at concentrations on the order of a few hundred parts per million (Pesode and Barve 2023). As a result, oxygen pickup during processing is not a minor contamination issue but a variable that meaningfully shifts phase boundaries and influence microstructural evolution (Ren et al., 2025). In β-type alloys, small additions of α-stabilizers are sometimes included deliberately, since they suppress the formation of the embrittling isothermal ω phase during aging (Brumbauer et al., 2024).

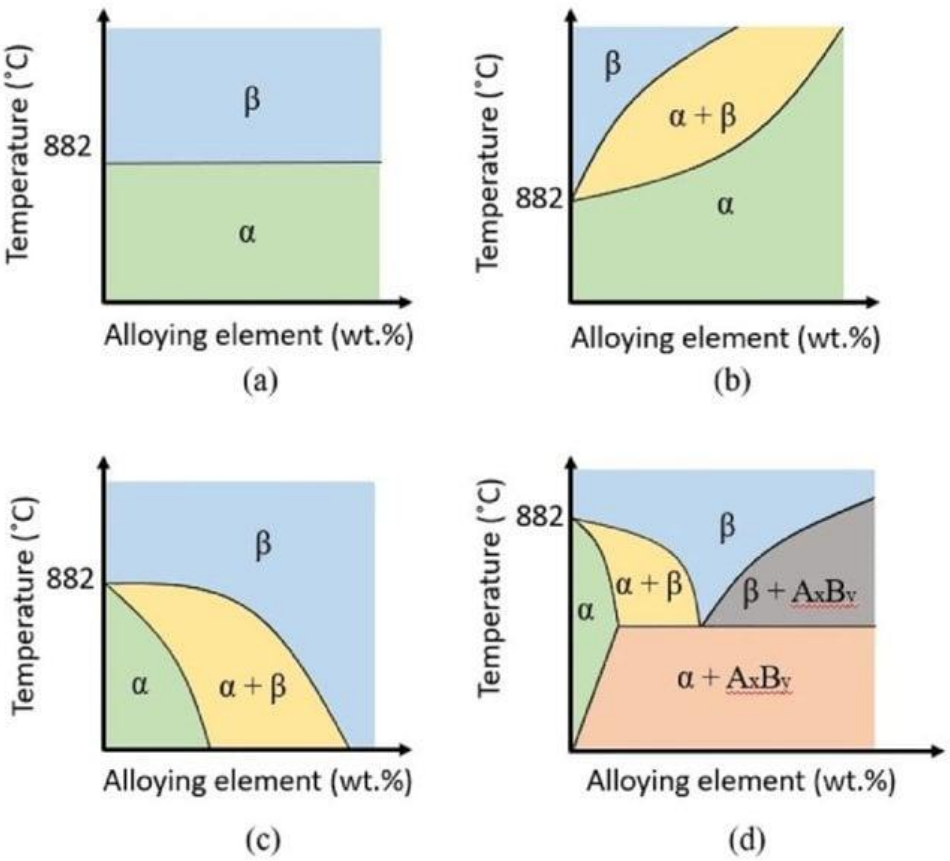

Figure 2.2. Schematic classification of alloying elements in titanium according to their influence on phase stability and the β-transus temperature in Ti-based binary systems: (a) neutral elements, (b) α-stabilizing elements, (c) isomorphous β-stabilizers, and (d) eutectoid β-stabilizers (adapted from Ahmad et al. 2020).

Beta-stabilizing elements are divided into two groups depending on the shape of their binary phase diagram with titanium. Isomorphous elements, including molybdenum, niobium, vanadium, tantalum, and tungsten, have complete or near-complete miscibility with β-Ti and lower the β-transus continuously with increasing concentration (Koul and Breedis 1970; Kolli and Devaraj 2018). To fully retain the metastable β phase after quenching from the single-phase field, a minimum concentration of each element is required. The required concentrations vary significantly. Molybdenum needs only 10 wt.%, while niobium and tantalum require 36 wt.% and 45 wt.%, respectively, to achieve the same effect (Kolli and Devaraj 2018). This means that the stabilizing potency of isomorphous elements is not interchangeable, which has direct consequences for alloy design (Kolli and Devaraj 2018; Irimescu et al. 2024).

Eutectoid elements, including iron, chromium, manganese, cobalt, copper, and silicon, have limited solid solubility in titanium and produce a eutectoid reaction in their binary phase diagrams with Ti (Ahmad et al. 2020). In general, these stabilizers are more effective per unit weight than their isomorphous counterparts. For example, iron requires only 3.5 wt.% and chromium 6.5 wt.% to maintain the β phase (Kolli and Devaraj 2018). The trade-off is a greater tendency toward intermetallic compound formation, which can compromise ductility and make processing more sensitive to composition control.

Neutral elements, principally zirconium and tin, do not shift the β-transus significantly in either direction. They are added to titanium alloys primarily because they alter the kinetics of ω-phase formation during aging, thereby stabilizing the β phase against decomposition. Tin also affects superelastic properties in some alloy systems by suppressing the athermal ω phase and lowering the martensite start temperature (Kolli & Devaraj 2018). Therefore, calling them neutral is somewhat misleading.

2.2 Deformation mechanisms in titanium alloys

2.2.1 Slip in α-titanium

Plastic deformation in α-titanium proceeds by dislocation glide on a limited set of crystallographic systems. The primary slip direction is ⟨a⟩, corresponding to the shortest lattice vector in the hexagonal structure. Slip occurs mainly on basal $\{0001\}$, prismatic $\{10\bar{1}0\}$, and pyramidal $\{10\bar{1}1\}$ planes. Prismatic ⟨a⟩ slip is the primary deformation mode in α-titanium, while basal ⟨a⟩ slip acts as a secondary system; the principal slip and twin systems of α-titanium are shown schematically in Figure 2.3 (Emelianova et al., 2025). However, these systems do not provide enough independent deformation modes to accommodate arbitrary plastic deformation in a polycrystal. As a result, deformation along the c-axis requires activation of ⟨c+a⟩ slip on pyramidal systems, such as $\{10\bar{1}1\}\langle 11\bar{2}3\rangle$ or $\{11\bar{2}2\}\langle 11\bar{2}3\rangle$, which are associated with significantly higher critical resolved shear stresses.

Because of that, the c/a ratio becomes important. In α-Ti, it is approximately 1.587, slightly below the ideal HCP value of 1.633, which affects the relative stability of slip systems and shifts their activation energies relative to those of other HCP metals.

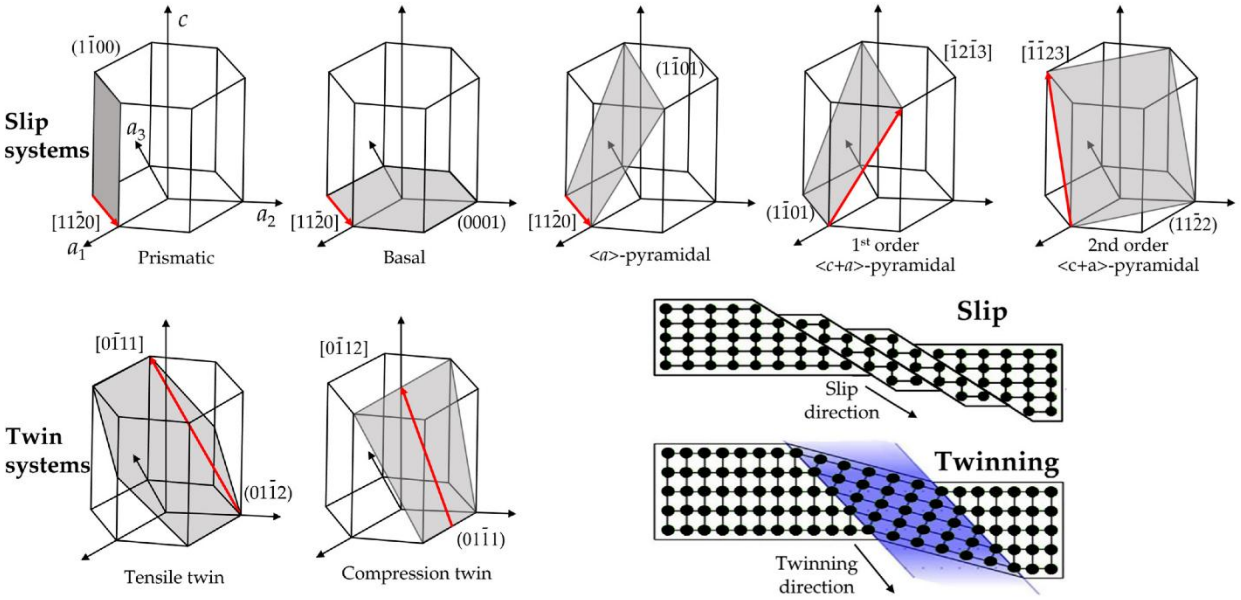

Figure 2.3. Slip and twin systems in α-titanium (adapted from Emelianova et al., 2025).

More generally, the orientation dependence of slip makes the mechanical behaviour of polycrystalline α-Ti inherently anisotropic. This anisotropy can be modified through alloying, which changes the relative contribution and stability of individual deformation mechanisms and underlies the structure–property relationships discussed in the following sections.

2.2.2 Twinning and phase transformations

When dislocation slip alone cannot accommodate the imposed strain, titanium can activate additional deformation mechanisms. Among these, mechanical twinning is particularly important in α-Ti, while martensitic phase transformations can become relevant in alloys containing metastable β phase. Twinning is an important deformation mechanism in HCP metals and becomes active when the available slip systems are insufficient (Christian and Mahajan, 1995). Twinning in α-Ti occurs on several crystallographic systems, most commonly on $\{10\bar{1}2\}\langle 10\bar{1}1\rangle$ tensile twins, but also on $\{10\bar{1}1\}$, $\{11\bar{2}1\}$, and $\{11\bar{2}2\}$ systems, depending on the stress state and crystallographic orientation (Banerjee and Williams, 2013; Fitzner et al., 2016). Twinning can also be triggered by the internal

stresses generated during the β→α transformation on cooling, so that cooling rate alone may activate it even in pure titanium (Lu et al. 2023).

In alloys with sufficient β-stabilizing content to retain metastable β at room temperature, an additional deformation mechanism becomes relevant. Under applied stress, the metastable β phase can transform martensitically to the orthorhombic α" phase through a diffusionless, shear-dominated mechanism. This stress-induced martensitic transformation, referred to as SIM α", is distinct from the thermally induced α' martensite that forms during rapid quenching. The transformation, together with additional twinning of the α" product that can accompany it, contributes to the high work-hardening capacity of such alloys (Chen et al. 2021).

An important feature of the β→α" transformation is its reversibility, which provides the basis for the superelastic behavior observed in some near-β Ti alloys. Its activation is sensitive to composition, temperature, and strain rate, meaning that the same alloy can deform through different mechanisms under different testing conditions. More generally, the operative deformation mechanism in titanium alloys depends on phase stability, crystallographic orientation, temperature, stress state, and processing history.

2.2.3 Structure-property relationship

The deformation mechanism that operates in a given titanium alloy is not fixed by composition alone. It reflects the combination of phase stability, phase volume fraction, and microstructural geometry, all of which can be tuned through alloying and processing. Because of that, the relationship between structure and mechanical properties in titanium alloys is considerably more complex than in single-phase metals. In alloys where the β phase is fully stable, deformation proceeds by conventional dislocation slip. As β phase stability decreases toward the metastable range, stress-induced transformations and twinning become energetically accessible, and the dominant mechanism shifts accordingly (Figure 2.4) (Zhao et al. 2022; Fu et al., 2024).

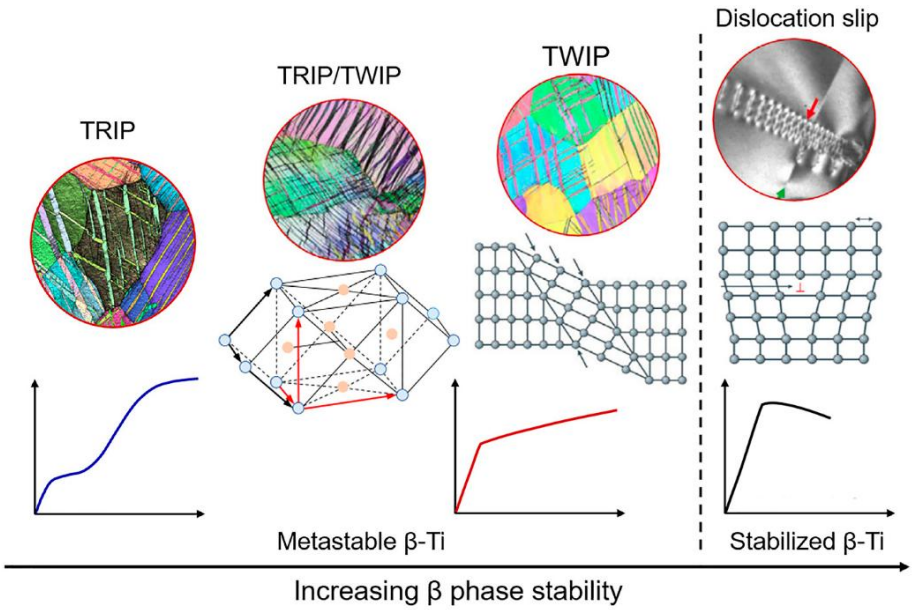

Figure 2.4. Variation of deformation mechanisms as a function of β-phase stability in β-Ti alloys (Zhao et al. 2022).

Kolli and Devaraj summarized this progression in terms of molybdenum equivalency: as MoE decreases from values characteristic of stable β alloys toward those of near-β alloys, the active mechanism sequence runs from slip through twinning and ω-phase formation to α″-martensite formation, with considerable overlap between adjacent regimes (Kolli and Devaraj 2018). Molybdenum equivalency is therefore a useful indicator of β-phase stability, and the mechanical properties can be modified through compositional changes along the MoE scale; it is not by itself

sufficient to predict the elastic modulus, yield strength, or work-hardening behaviour, since these properties also depend on the microstructure that develops during processing.

The Young's modulus is particularly sensitive to this. The β phase has a lower intrinsic modulus than α, and among the metastable phases, α'' has a lower modulus than α' (Lee et al., 2002; Ruzic et al., 2018). Alloys designed to sit near the boundary between metastable β and SIM α'' transformation can achieve modulus values approaching those of cortical bone, which is the primary motivation for this class of alloys in biomedical applications. The difficulty is that the same composition window that gives a low Young's modulus also tends to yield a low yield strength, because the stress-induced transformation accommodates strain without requiring large dislocation densities. Reconciling low modulus with adequate strength is a central design challenge in Ti alloys for implants.

Phase stability and phase constitution, however, are only part of the picture. For a given phase assembly, the mechanical behavior is further governed by the microstructural geometry, including the volume fractions of the constituent phases (α, β, α'' and ω), the grain size, and the morphology of α phase, in particular whether it is equiaxed or lamellar and the thickness and orientation of α lamellae. Crystallographic texture adds a further layer of anisotropy, since the strong orientation dependence of slip in α-Ti carries over to the polycrystal. Interstitial elements, especially oxygen, shift phase boundaries and strengthen α phase even at low concentrations. In addition, processing-induced features such as porosity in powder-metallurgy and additively manufactured alloys, together with the defect structure inherited from thermomechanical treatment, can dominate the measured properties (Lütjering and Williams 2003; Banerjee and Williams 2013; Ren et al. 2025).

These microstructural descriptors are rarely available in a quantitative form in the literature, which limits how directly they can be incorporated into composition-based property models. For this reason, the predictive models developed in this work rely on the information that is consistently reported, namely composition, processing route, and composition-derived descriptors, while the role of the microstructure is assessed experimentally. The EBSD, MIPAR, and nanoindentation analyses presented in later chapters link the local elastic response of the synthesized alloys to their phase constitution, α-lamellar morphology, and crystallographic orientation, and thereby help interpret the difference between the predicted and measured behavior.

2.2.4 Atomistic perspective on deformation mechanisms in α-titanium

Experimental techniques can characterize deformation products after the fact, but the nucleation events that initiate plasticity happen on length and time scales that are difficult or impossible to access directly. Molecular dynamics simulation helps fill this gap by providing atomic-resolution trajectories of the deformation process from its earliest stages. Such simulations of single crystalline α-Ti show that the onset of plasticity is strongly orientation-dependent and can involve localized structural rearrangements beneath the indenter in addition to conventional dislocation activity. This makes atomistic modeling a useful complement to experiments, because the modulus extracted from a nanoindentation load–displacement curve reflects both elastic anisotropy and any subsurface rearrangement that precedes conventional plasticity, and this response varies between grains of different orientation. The detailed atomistic analysis of these orientation-dependent mechanisms, and its connection to the experimental nanoindentation of the present alloys, is developed in Chapter 4 (Section 4.9).

2.3 Design approaches for titanium alloys

Because the relationships among composition, phase stability, and mechanical behavior in titanium alloys are highly complex, several approaches have been developed to guide alloy design. These methods differ not only in their theoretical background but also in the type of information they provide. Some are intended mainly to estimate phase stability and to identify whether a given composition is likely to form α, β, or metastable structures, while others aim to establish deeper

relationships between composition, electronic structure, processing, and mechanical properties such as Young's modulus.

The simplest approaches are based on empirical or semi-empirical parameters derived from binary alloy systems, including Mo equivalency, electron-to-atom ratio (e/a), and d-electron theory. These methods provide relatively fast estimates of β-phase stability and trends in elastic behavior, but their predictive capability is limited in multicomponent systems, where interactions between alloying elements are often nonlinear. More advanced computational approaches, such as CALPHAD and first-principles calculations, incorporate thermodynamic or quantum-mechanical descriptions of the system and can offer more detailed insight into phase equilibria, transformation behavior and elastic properties. High-throughput experimentation extends this idea experimentally by generating and screening large compositional spaces in relatively short time.

More recently, machine learning approaches have introduced a different strategy. Instead of relying solely on predefined physical descriptors or phase stability criteria, machine learning models search for statistical relationships within large datasets and can consider many compositional and processing variables simultaneously. This makes them particularly attractive for multicomponent titanium alloys, where conventional empirical trends are often insufficient to describe the resulting phase constitution and mechanical behavior. Their reliability, however, depends strongly on the quality and representativeness of the underlying data and descriptors. These approaches are complementary rather than interchangeable. Empirical parameters allow rapid screening, thermodynamic and first-principles methods add physical depth, and machine learning can explore large composition spaces, but none of them fully captures the combined effect of composition, processing, and microstructure on the mechanical behavior. This is the main reason the present work combines data driven prediction with experimental validation, an approach developed in the following subsections.

2.3.1 Empirical and semi-empirical design parameters

Empirical and semi-empirical design parameters are widely used in titanium alloy development because they provide rapid estimates of phase stability and expected mechanical behavior directly from composition. These approaches reduce complex alloy chemistry to simplified descriptors, such as molybdenum equivalency, the electron-to-atom ratio, and d-electron parameters. Although useful for screening and comparison, their predictive capability is limited in multicomponent alloys, where interactions between alloying elements, processing history, and microstructure strongly influence the final phase constitution and mechanical properties.

2.3.1.1 Composition based design - Mo equivalence method ([Mo]eq)

In the previous sections, it was shown that different alloying elements influence the α↔β transformation temperature in different ways, and that the addition of β-stabilizing elements lowers this temperature. When more than one β stabilizer is present, their combined effect is usually expressed through the concept of Mo equivalence. In practice, this means that the contribution of each alloying element is normalized to molybdenum, which is taken as the reference element **(**Molchanova and Glazunov 1965; Korkmaz and Erdoğan 2026)**.** The coefficient assigned to each element indicates its effectiveness for stabilizing the β phase relative to Mo. More precisely, it corresponds to the ratio between the critical concentration of Mo, commonly taken as 10 wt.% for retaining a fully metastable β phase after quenching, and the concentration of the specified element required to achieve the same effect (Bania 1994).

The concept originates from the way β-stabilizing elements modify Ti-based phase diagrams. The addition of β-stabilizers effectively extends the β-phase field to lower temperatures, which is why their effect can be summarized by a single parameter. This is often illustrated using binary Ti–M phase diagrams (Figure 2.5), where the shift of the β/(α+β) boundary provides a direct measure of β stabilization (Wang et al. 2015)**.**

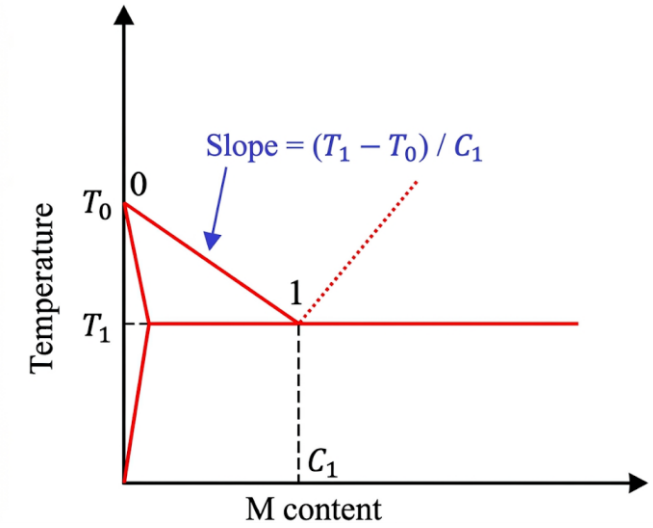

Figure 2.5. Schematic representation of the effect of β-stabilizing elements on the β-phase field in Ti-based alloys, illustrated through the shift of the β/(α+β) boundary in binary phase diagrams (Wang et al. 2015).

Since aluminum was originally a component of many titanium alloys, it was also included in the first Mo equivalence expressions as an element that reflects the tendency for α-phase stabilization in β-Ti alloys. The Mo equivalence proposed by Bania is given by Equation (1) (Bania 1994):

$$[Mo]eq_B = Mo + 0.67\,V + 0.44\,W + 0.28\,Nb + 0.22\,Ta + 2.9\,Fe + 1.6\,Cr + 0.77\,Cu + 1.11\,Ni + 1.43\,Co + 1.54\,Mn + 0.0\,Sn + 0.0\,Zr - 1.0\,Al\ (wt\%). \quad (1)$$

Over time, several modified expressions have been proposed. Zhou introduced a revised form in which the coefficients were further adjusted (Equation (2)) (Zhou 2000), while Wang extended the approach by including additional alloying elements such as Zr and Sn, and defining two expressions depending on whether the composition is given in weight or atomic fractions (Equations (3) and (4)) (Wang et al. 2015).

$$[Mo]eq\_Z = Mo + 0.74\,V + 0.5\,W + 0.39\,Nb + 0.28\,Ta + 2.2\,Fe + 1.69\,Cr + 0.85\,Cu + 1.22\,Ni + 1.57\,Co + 1.69\,Mn + 0.0\,Sn + 0.0\,Zr - 1.0\,Al\ (wt\%). \quad (2)$$

$$[Mo]eq\_W = Mo + 1.25\,V + 0.59\,W + 0.28\,Nb + 0.22\,Ta + 1.93\,Fe + 1.84\,Cr + 1.51\,Cu + 2.46\,Ni + 2.67\,Co + 2.26\,Mn + 0.3\,Sn + 0.47\,Zr + 3.01\,Si - 1.47\,Al\ (wt\%). \quad (3)$$

$$[Mo]eq_W = Mo + 0.74\,V + 1.01\,W + 0.23\,Nb + 0.3\,Ta + 1.23\,Fe + 1.1\,Cr + 1.09\,Cu + 1.67\,Ni + 1.81\,Co + 1.42\,Mn + 0.38\,Sn + 0.34\,Zr + 0.99\,Si - 0.57\,Al\ (at\%). \quad (4)$$

Mo equivalence values are often used to classify titanium alloys. Values in the range of 5–10 are typically associated with near-β alloys, values between 10 and 30 with metastable β alloys, and values above 30 with stable β compositions. These limits, however, should not be treated as strict boundaries (Cotton et al. 2015).

The agreement between projected and observed phase equilibrium is generally best for binary systems. In more complex alloys, the situation becomes less straightforward. For example, the Ti–24Nb–4Zr–7.9Sn alloy has a Mo equivalence of 6.7 wt.%, which is below the commonly cited threshold of 10 wt.%, yet a single β phase can still be obtained after quenching (Cotton et al. 2015).

This shows a more general limitation of the Mo equivalence approach. The concept is primarily derived from binary phase diagrams, where the effect of each element is considered independently. In multi-component systems, interactions between alloying elements are not necessarily additive, and their combined effect on phase equilibrium may differ from what is expected based on simple summation. As a result, alloys with similar Mo equivalence values do not always exhibit the same phase constitution.

2.3.1.2 Electron-to-atom ratio (e/a) method

The electron-to-atom ratio (e/a) is a semi-empirical descriptor used to relate alloy composition to phase stability and elastic behavior in titanium alloys. It is calculated as the composition-weighted average number of valence electrons per atom:

$$\frac{e}{a} = \sum c_i * \ v_i, \tag{5}$$

where c_i is the atomic fraction of element *i*, and v_i is its number of valence electrons.

In several metastable β-Ti alloy systems, e/a has been associated with changes in β-phase stability, ω-phase formation, and elastic modulus (Tiwari and Ramanujan 2001).

Titanium is a transition metal with a partially filled outer electron shell, which allows it to form solid solutions with a wide range of substitutional alloying elements, provided that the atomic size mismatch remains sufficiently small according to the Hume–Rothery criteria (Keppens 2008). The stability of the α and β phases is influenced by the number of valence electrons contributed by the alloying elements, which is directly related to their position in the periodic table (Liang 2020). In several metastable β-Ti alloy systems, a decrease in e/a has been associated with a reduction in elastic modulus, reaching a minimum just before the formation of the ω phase (Figure 2.6), after which it begins to increase again (Liang 2020).

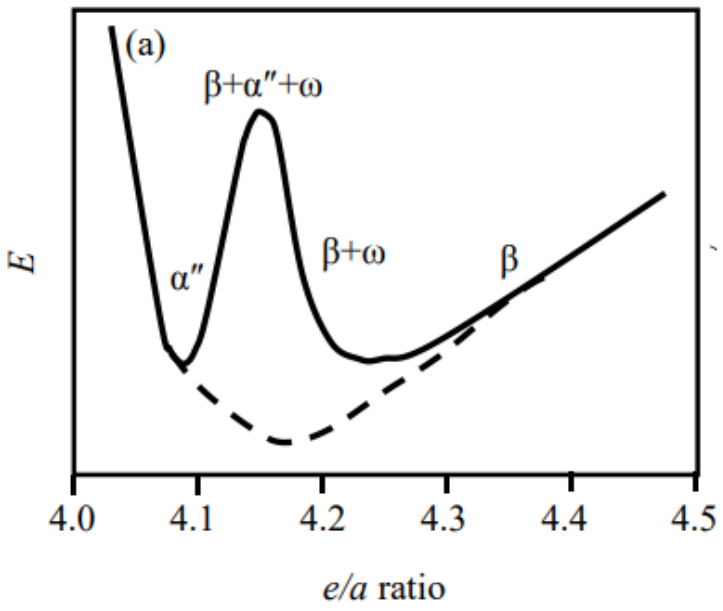

Figure 2.6. Young's modulus of multicomponent titanium alloys as a function of the e/a ratio (Liang 2020).

Most studies have focused on binary systems, making it difficult to directly extrapolate the observed relationship between Young's modulus and e/a to multicomponent titanium alloys. Although many studies report a minimum in elastic modulus at e/a ≈ 4.2, this value is not universally accepted. In addition, there is still no clear consensus on whether the valence electrons of interstitial elements such as oxygen should be included in the calculation of the e/a ratio (Tane et al. 2008; Tane et al. 2011**;** Stráský et al. 2017).

2.3.1.3 d-electron concept

The d-electron concept represents one of the theoretical approaches used in the design of titanium alloys (Li et al., 2023). It is based on molecular orbital theory, and the results are typically presented using Bo–Md diagrams, which allow estimation of phase stability, dominant deformation mechanisms, and expected ranges of elastic modulus (Figure 2.7). The parameter Bo represents the bond order, i.e., the strength of covalent bonding between titanium and the alloying elements. Higher Bo values indicate stronger interatomic bonding. The parameter Md corresponds to the average energy level of the d orbitals and is related to both atomic radius and electronegativity. In multicomponent alloys, Bo and Md are expressed as composition-weighted average values. Both parameters depend on the atomic fractions of the constituent elements and the corresponding Bo and Md values for each element (Abdel-Hady et al., 2006). This d-electron (Bo–Md) approach was originally developed by Morinaga and co-workers (Morinaga et al., 1988).

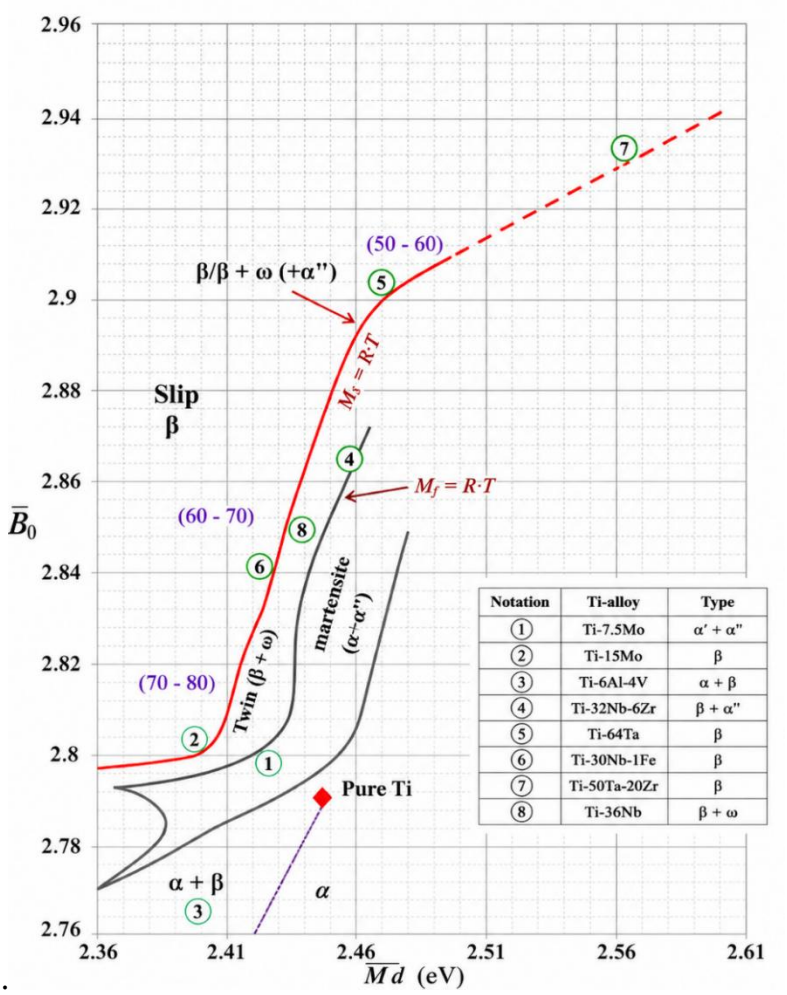

Figure 2.7. Extended Bo–Md diagram showing regions of phase stability, dominant deformation mechanisms, and the corresponding Young's modulus ranges for titanium alloys (Abdel-Hady et al., 2006).

Titanium alloys can deform through different mechanisms depending on their phase stability. As the stability of the β phase increases, the dominant deformation mechanism shifts from twinning to dislocation slip, while metastable β alloys tend to exhibit behavior at the boundary between these mechanisms. Although this approach has been successfully used in the design of low-modulus titanium alloys, it also has several limitations. First, the set of alloying elements must be defined in advance, since similar Bo and Md values can be achieved using different combinations of elements and compositions (Liang 2020). Second, there is no universal threshold that guarantees a minimum elastic modulus, as the optimal range depends on the specific alloy system and the resulting phase constitution (Liang 2020; Bahl et al., 2021). In addition, the effects of α-stabilizing and neutral elements are not completely captured by this model, even though such elements, including oxygen, tin, and zirconium, are able to significantly influence β-phase stability. The model also provides only approximate estimates of elastic modulus rather than exact values. Finally, the decrease in elastic modulus with increasing Bo and Md values is not always observed, particularly in more complex alloy systems (Bahl et al., 2021).

2.3.2 High-throughput experimentation in alloy development

Conventional alloy development is typically based on preparing and testing a relatively small number of compositions within a single alloy system. As the number of possible multicomponent compositions increases, such an approach becomes increasingly slow and experimentally demanding. High-throughput experimental methods were developed to accelerate the exploration of large compositional spaces by enabling simultaneous synthesis and characterization of many alloy compositions within a single experimental workflow (Cawse 2001; Liu et al. 2019).

One of the most commonly used approaches is combinatorial thin-film deposition, where multiple alloying elements are deposited onto a substrate in order to generate continuous compositional gradients. Different strategies have been reported, including co-sputtering, sequential deposition, and composition-spread methods (Cawse 2001). Another important approach is the diffusion-multiple method, in which several metallic components are joined and annealed to produce compositionally graded regions through interdiffusion (Liu et al. 2019).

Characterization of such compositionally complex samples usually requires localized experimental techniques, including electron probe microanalysis (EPMA), X-ray diffraction (XRD), X-ray fluorescence (XRF), scanning electron microscopy (SEM), electron backscatter diffraction (EBSD), and nanoindentation measurements (Liu et al. 2019). More recently, high-throughput experiments have increasingly been combined with computational modeling, automated workflows, and machine learning approaches (Gao et al,, 2025). Vecchio et al. proposed a high-throughput rapid experimental alloy development (HT-READ) framework integrating additive manufacturing, automated characterization, and machine-learning-assisted optimization within a closed-loop workflow (Figure 2.8) (Vecchio et al. 2021).

Although high-throughput methods can rapidly map large compositional spaces, they also have limitations. Local measurements on thin films or diffusion couples may not fully represent bulk behavior, and the microstructures formed in these geometries can differ from those of conventionally processed alloys. For this reason, the present work relies on experimentally synthesized bulk Ti alloys together with microstructure-sensitive nanoindentation measurements.

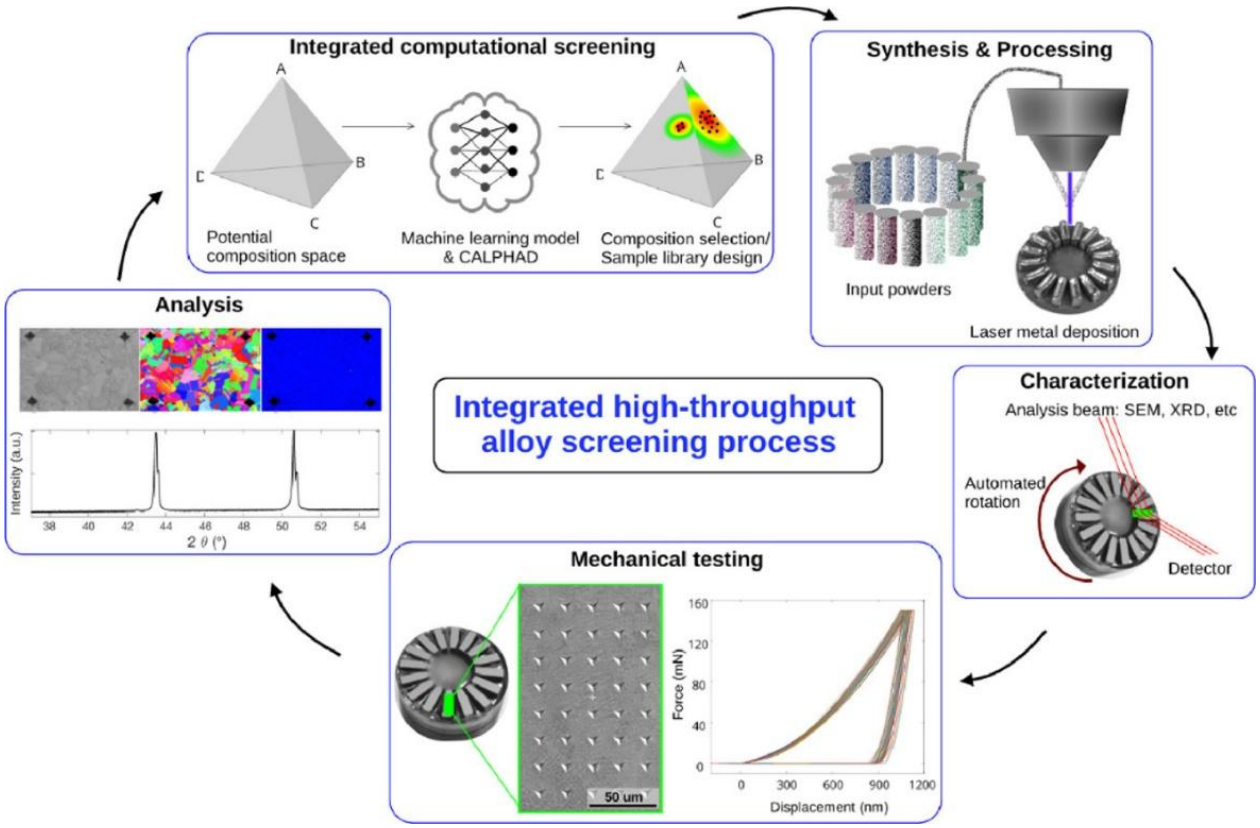

Figure 2.8. The integrated high-throughput rapid experimental alloy development (HT-READ) process, combining computational screening, synthesis, characterization, mechanical testing, and analysis in a closed-loop workflow (Vecchio et al., 2021).

2.3.3 Computer-based approaches

Computational alloy design approaches are increasingly used to guide the development of titanium alloys before experimental synthesis. These methods can reduce the number of trial-and-error experiments by predicting phase equilibria, phase stability, electronic structure, and composition-property relationships across complex alloy systems. In titanium alloy development, the most widely used computational approaches include CALPHAD-based thermodynamic modelling, first-principles calculations, and machine-learning-based prediction models.

2.3.3.1 CALPHAD methodology

The CALPHAD (Calculation of Phase Diagrams) approach is a thermodynamic method used for calculating phase equilibria and phase stability in complex alloy systems (Kroupa, 2013; Kattner, 2016). The calculations are based on Gibbs free energy functions of individual phases, where the stable phase under given conditions corresponds to the state with the lowest free energy. Thermodynamic descriptions developed for binary and ternary systems are gradually combined into larger databases, allowing calculations in multicomponent alloys (Kroupa, 2013).

The reliability of CALPHAD predictions strongly depends on the quality and completeness of the thermodynamic database. Modern databases include assessed binary and ternary systems and account for both stable and metastable phases. This allows not only the prediction of equilibrium phase diagrams, but also the estimation of phase fractions, transformation temperatures, and metastable equilibria in complex materials systems (Kattner, 2016).

One of the main advantages of the CALPHAD approach is its usefulness to multicomponent systems, in which experimental investigation of phase equilibria becomes more complex and time-consuming. In such cases, CALPHAD calculations can narrow the compositional domain and guide alloy design

before experimental synthesis (Kroupa, 2013). This is possible because CALPHAD relies on assessed thermodynamic databases to compute the Gibbs free energy of the individual phases, from which the stable phases, their volume fractions, and the phase boundaries can be obtained as a function of composition and temperature (Kattner, 2016; Kattner, 2020). By mapping phase stability in this way, the method identifies the compositions and heat-treatment windows likely to yield the target phase constitution, such as a retained or metastable β phase, so that experimental effort can be focused on the most promising regions. In this context, CALPHAD is used primarily as a phase-stability screening tool, rather than for direct prediction of mechanical properties such as elastic modulus. The method is therefore widely used within state-of-the-art computational alloy design strategies and Integrated Computational Materials Engineering (ICME) frameworks (Perrut, 2015; Kattner, 2016). In practice, CALPHAD calculations are frequently combined with experimental approaches such as diffusion couples and compositional-gradient methods. Ding et al. (2021), for example, combined CALPHAD calculations with diffusion couple technology to study titanium alloys, demonstrating how thermodynamic modeling can be used in conjunction with experimental screening to investigate phase stability and alloy properties more efficiently.

2.3.3.2 First principles calculations

The first-principles calculations are based on the principles of quantum mechanics and allow to calculate the material properties directly from the atomic structure of the system without the necessity of experimentally fitted parameters (Hermann and Kurzydłowski, 2019). The most often used approach for such calculations in the field of materials science is the density functional theory (DFT). One of the main reasons of its broad application is the possibility of treating relatively large systems at a reasonable computational cost in comparison to other quantum-mechanical methods (van Mourik et al., 2014).

In general, DFT calculations involve the construction of an atomic model, geometry optimization, determination of the electronic ground state, and subsequent calculation of material properties from the obtained electronic structure. For the prediction of elastic properties, small strains are typically applied to the optimized crystal structure and the resulting stress or energy changes are used to determine the elastic constants. These constants can then be converted into macroscopic elastic parameters through appropriate averaging schemes (Figure 2.9).

Density functional theory calculations are widely used to investigate the phase stability and elastic behavior of titanium alloys, particularly in the computational design of β-Ti alloys (Raabe et al., 2007; Karre et al., 2015). Elastic constants are commonly calculated by applying small strains to the equilibrium crystal structure and evaluating the resulting changes in stress or total energy (Golesorkhtabar et al., 2013). From the obtained elastic constants, the bulk modulus, shear modulus and Young's modulus can be estimated using the Voigt–Reuss–Hill approximation (Ikehata et al. 2004). Besides elastic response, first-principles calculations are widely used to investigate formation energies, phase stability, and the connection between electronic structure and mechanical behavior (Raabe et al., 2007; Karre et al., 2015).

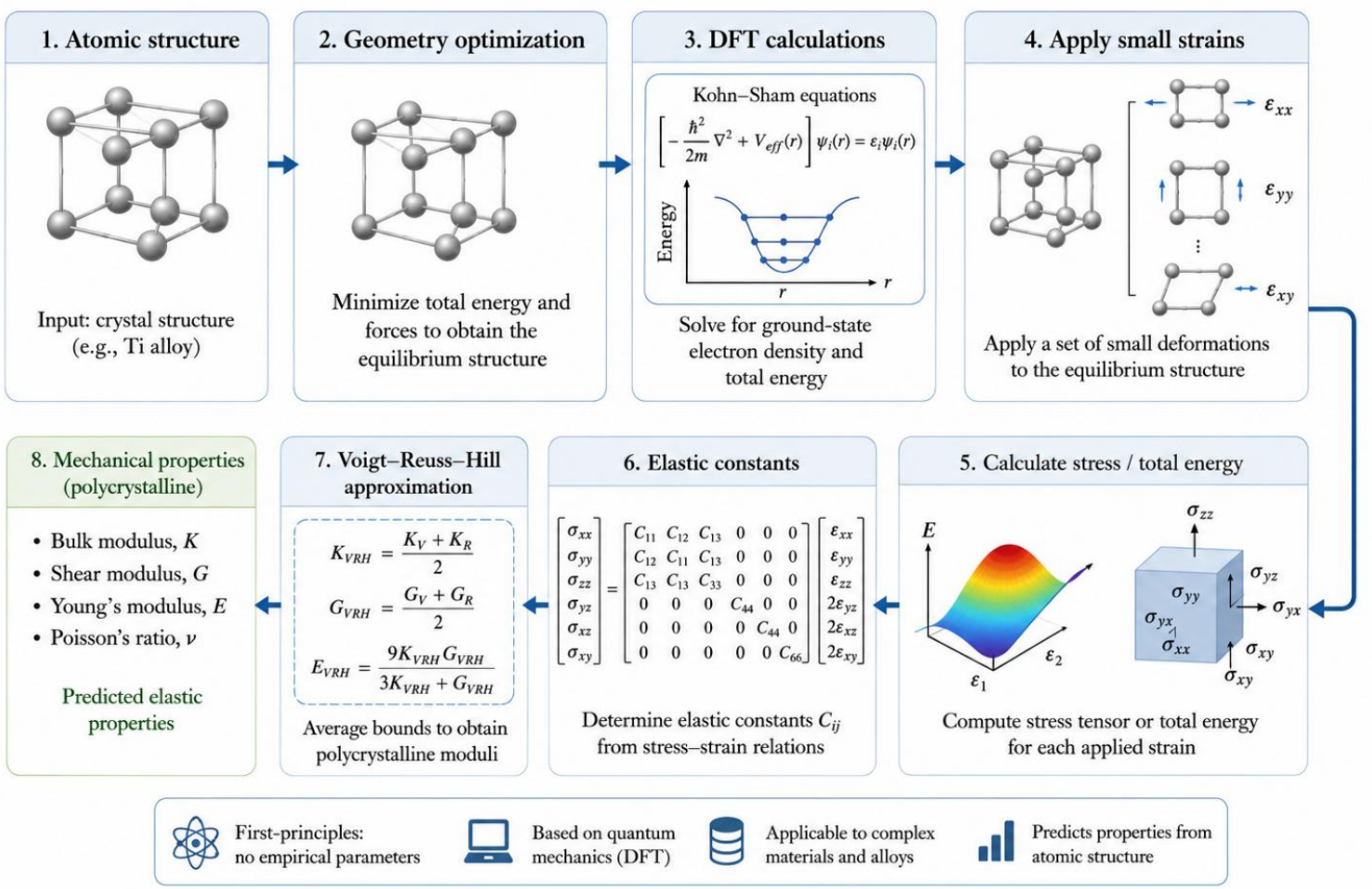

Figure 2.9. Schematic representation of the density functional theory workflow used for the prediction of elastic properties.

2.3.3.3 Machine-learning based alloy design

Machine learning approaches have become increasingly common in titanium alloy design, particularly in systems where relationships between composition, phase stability, processing history, and mechanical properties are difficult to describe using conventional empirical approaches alone (Wu et al., 2020; Zou et al., 2021; Niu et al., 2023; Liu et al., 2025; Zhang et al. 2025). Instead of relying only on simplified descriptors or extensive experimental trial-and-error, machine learning models can identify patterns within large datasets and use them to estimate material properties for unexplored compositions (Ramprasad et al., 2017). The general workflow used in machine learning-based materials design is schematically shown in Figure 2.10.

In practice, the workflow consists of several connected stages, including data collection, preprocessing, descriptor selection, model training, validation, and prediction. Data may originate from published literature, public databases, experimental measurements, or theoretical calculations. Commonly used materials science databases include the National Institute for Materials Science (NIMS), Materials Project (MP), and Materials Platform for Data Science (MPDS) (Liu et al., 2022), while integrated informatics platforms connecting data, descriptors, and models have also been developed (Wang et al., 2023).

The quality and representativeness of the dataset often have a greater influence on model performance than the choice of the machine-learning algorithm itself (Ramprasad et al. 2017). Experimental data collected from different studies frequently involve variations in processing conditions, heat treatment procedures, testing methodologies, and sample preparation, all of which may introduce additional scatter into the dataset. Because of that, preprocessing usually includes removal of inconsistent entries, handling of missing values, normalization, and outlier analysis.

Another important step is descriptor selection. In titanium alloy design, descriptors are commonly derived from alloy composition, electronic structure, atomic size mismatch, or phase stability parameters. However, many of these variables are strongly correlated with one another. This becomes particularly important in multicomponent systems, where changes in one alloying element may simultaneously influence several descriptors. As a result, distinguishing the individual contribution of specific variables is often not straightforward (Liu et al., 2022).

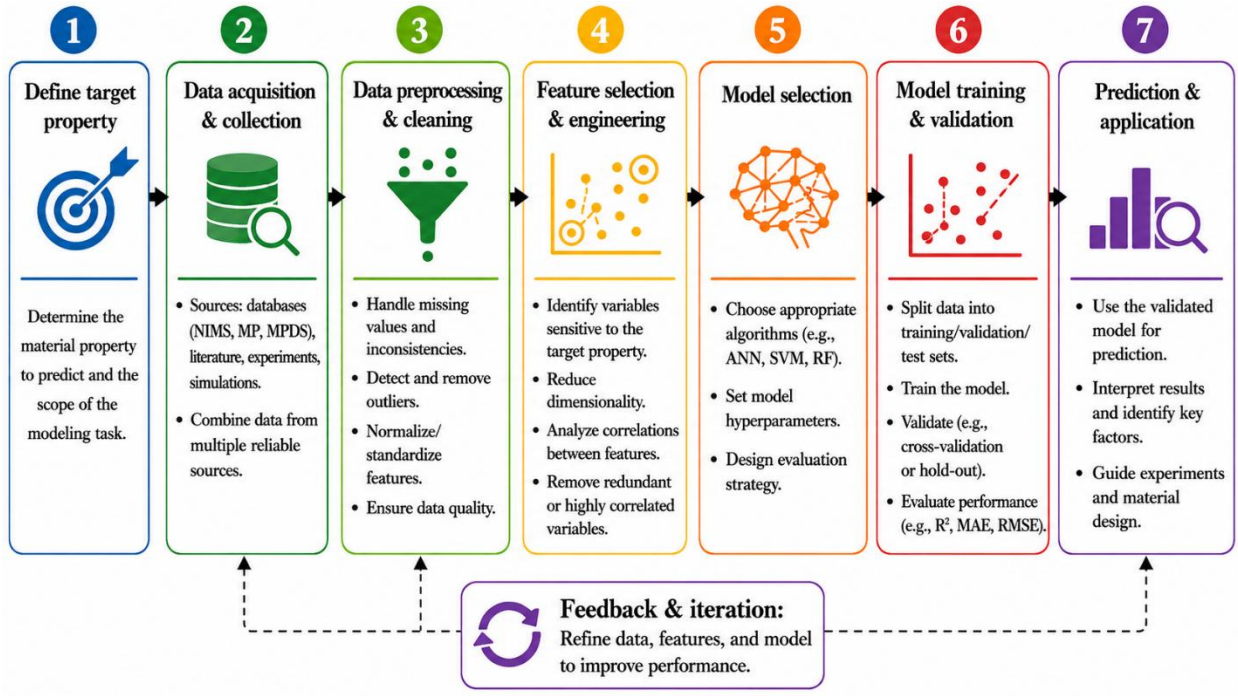

Figure 2.10. General workflow used in machine learning-based materials design, including data collection, preprocessing, descriptor selection, model training, validation, and prediction.

Various machine learning algorithms have been applied for titanium alloy prediction, including artificial neural networks, support vector machines, random forests, and gradient boosting approaches. After training and validation, the resulting models can be used to estimate mechanical properties for unexplored alloy compositions and to identify regions of compositional space potentially associated with desirable behavior, such as reduced elastic modulus (Liu et al., 2022).

The reliability of machine-learning predictions is, however, strongly constrained by the data from which the models are built. Titanium alloy datasets assembled from the literature are often small and heterogeneous, contain incomplete processing information, and include correlated descriptors, which increases the risk of unreliable predictions when the model is extrapolated outside the compositional region represented in the training set. Most composition-based models also lack explicit microstructural descriptors. Machine learning is therefore best regarded as a tool for screening and prioritizing candidate compositions, while experimental validation remains necessary, because the final properties also depend on phase constitution, processing history, texture, and microstructure.

2.3.4 Advanced experimental design for multicomponent alloys

The development of titanium alloys generally involves three interconnected stages: compositional design, processing design, and experimental validation.

In multicomponent alloy development, the experimental design problem differs from conventional factorial experimentation because alloy compositions are mixture systems. In a ternary alloy, the component fractions are constrained by the condition $x_1 + x_2 + x_3 = 1$, so the compositional space is represented by a two-dimensional simplex, commonly shown as a Gibbs triangle. Since changing the amount of one component necessarily changes the relative amounts of the others, mixture designs are more appropriate than standard factorial designs for exploring alloy composition spaces. Classical mixture-design methods, such as simplex-lattice and simplex-centroid designs, provide systematic ways to select experimental compositions within this constrained space.

More recent approaches extend this logic from one-step experimental planning to sequential, model-guided alloy design. In active learning and Bayesian optimization, an initial model is trained on the available data and then used to suggest the next most informative composition to synthesize or calculate, balancing exploration of poorly known regions with exploitation of promising compositions. This strategy is particularly relevant for alloy development, where each melting, heat treatment, and characterization step is experimentally expensive, so that machine learning can be used as a tool for the rational selection of future experiments.

The first stage focuses on compositional design. In practice, the development of new titanium alloys rarely begins from completely unexplored compositional spaces. Instead, a common approach is to start with a well-defined binary system and then change the concentration of the already existing alloying elements or add a new alloying element. Examples include the extension of the Ti–Nb, Ti–Mo and Ti–Zr systems into more complex ternary and multicomponent alloys (Li et al., 2020; Cardoso et al., 2022; Chen et al., 2017; Martins Junior et al., 2024). This approach allows researchers to build on their existing knowledge of phase stability and mechanical behavior while systematically evaluating the effect of newly introduced alloying additions. Simultaneously, it simplifies interpretation of the experimental results since the effect of a single variable can be assessed with respect to a well-understood baseline composition.

Once a suitable composition has been selected, processing design becomes equally important. The final microstructure of titanium alloys is controlled not only by composition but also by processing history. Parameters such as melting route, thermomechanical treatment, heat treatment temperature, holding time and cooling rate directly influence phase transformations, grain morphology, crystallographic texture and phase fractions.

Thus, alloys of the same nominal composition can have quite different microstructures and mechanical properties when processed under different conditions (Žitňanský and Čaplovič, 2004; Banumathy et al., 2011; Zhou and Luo, 2011; Kuroda et al., 2020).

The final step is the experimental validation and optimization of the performance of the material. Depending on the intended application, characterization may include phase analysis, microstructural examination, mechanical testing, corrosion assessment, and biocompatibility evaluation. The experimental results are subsequently used to verify the initial design assumptions and to establish relationships between composition, processing conditions, microstructure, and material properties.

The present work follows this general design philosophy. A Ti–Mo–Sn alloy system, which has received comparatively limited attention in the context of low-modulus biomedical titanium alloys, was selected as a case study for experimental validation of machine-learning predictions. Rather than optimizing an already established alloy family, the objective was to evaluate the ability of the developed model to identify compositions exhibiting reduced elastic modulus.

For this purpose, a series of Ti–6.2Mo–xSn wt.% (x = 5, 10, 15) alloys was synthesized and characterized experimentally. The main objective of the present work was the validation of the predicted elastic behavior. Since elastic properties in titanium alloys are strongly affected by phase constitution and microstructure, additional characterization techniques were used to better understand the observed response. The phase composition was characterized by X-ray diffraction, whereas microstructural features, crystallographic characteristics, and local elastic properties were investigated by scanning electron microscopy, electron backscatter diffraction, and nanoindentation, respectively. These analyses allowed the predictive ability of the machine-learning model to be assessed and provided insights into the structural factors affecting the measured elastic modulus.

3. Materials and methods

3.1 Database construction

The database was developed to collect published mechanical-property data for titanium alloys in a form suitable for statistical analysis and machine learning. The starting point was the dataset described by Manojlović and Marković (2023) and deposited in the Zenodo repository (record 7802694). This dataset was extended with additional data from the literature, while the existing records were rechecked against the original publications. The database used in this work therefore represents an extended and revised version of the previously published dataset, and this final version is archived as a new version of the same Zenodo record (Manojlović and Marković, 2026).

Each database record represents a specific combination of alloy composition, processing state, and publication. The same nominal alloy composition can therefore appear in several records when different heat treatments, deformation states, specimens, or measurements are reported. These records were kept separately because they represent different experimental conditions. Each record was assigned a unique identifier, allowing the reported values to be traced back to the corresponding alloy and publication.

The collected information was divided into five groups. The first contains the alloy designation and elemental composition in both weight and atomic percent. The second describes the production route and thermomechanical treatment, including casting, rolling, forging, solution treatment, ageing, annealing, quenching, treatment temperature and time, and deformation, where this information was available. The third group contains Young's modulus and the other reported mechanical properties: yield strength, ultimate tensile strength, elongation, and hardness. The fourth contains information related to the measurement, while the fifth contains the bibliographic reference and the digital object identifier, when available.

For the measurement data, the physical quantity reported in the original publication was recorded separately from the experimental method used to determine it. Young's modulus, reduced indentation modulus, and modulus obtained from compression of a short specimen were therefore treated as different quantities. Similarly, tensile testing, ultrasonic or dynamic testing, and indentation were recorded as measurement methods. In this way, data obtained using different experimental techniques could be retained in the database without treating different elastic quantities as the same modelling target.

The reported values were entered using the units defined by the database schema and checked against the corresponding text, tables, and figures in the original publication. Alloy designations were retained to preserve traceability, while the elemental columns provided the numerical compositions used in the subsequent calculations. If an element was not included in the reported nominal composition, its content was entered as zero. For interstitial elements, however, a value of zero only indicates that no content was reported and available for the calculation and does not imply its complete physical absence. The treatment of these values during feature construction is described in Section 3.3.

Missing processing information was retained as missing rather than replaced by assumed values. Thus, a missing treatment temperature or time indicates that no usable numerical value was reported in the original source and does not imply that the material was untreated. Boolean reporting indicators were later introduced for selected processing variables to distinguish missing information from an explicitly reported zero value.

The database was finalized before the statistical and predictive analyses were performed, and all results presented in Chapter 4 were obtained using the same fixed version. Any subsequent correction or addition to the database would therefore require a new version and re-evaluation of the corresponding results.

3.2 Data preprocessing along with dataset refinement

The database was further refined to define a consistent domain for modelling while retaining titanium alloys with unusual but physically plausible properties. The selection criteria were based on the measured quantity, material form, data completeness, and information available in the primary source. Model prediction errors were not used as a criterion for including or excluding records.

Young's modulus was selected as the primary modelling target. A record was included when the original source explicitly reported Young's modulus or an equivalent elastic modulus measured by a method intended to determine this quantity. Reduced indentation modulus, Er, was retained in the complete database as a separate measurand but was not used as Young's modulus. Conversion of Er to specimen Young's modulus requires the specimen Poisson ratio and the elastic constants of the indenter. Since these values were unavailable or inconsistent across the collected publications, applying a common retrospective conversion would introduce additional assumptions. When the original authors had already converted indentation results to specimen Young's modulus, the reported value remained eligible for modelling because the conversion was defined in the source. Modulus values obtained from compression of short specimens were also retained in the complete database but excluded from the Young's modulus target. These criteria refer to the reported physical quantity rather than the quality of the experimental technique. Tensile, dynamic, ultrasonic, and indentation methods were therefore not ranked. In the controlled nanoindentation experiment described in Section 3.6.5, the same set of elastic constants was used for all specimens, allowing Er to be converted consistently within that experimental series.

The composition-based model was restricted to conventional, predominantly dense alloy products. Records produced by powder metallurgy, sintering, metal injection moulding, additive manufacturing, and powder-fed laser cladding were excluded from the main modelling domain. The elastic response of materials produced by these routes can be strongly influenced by porosity, incomplete consolidation, build direction, and route-specific microstructure. Since these factors were not reported consistently enough to be included in the model, such records were kept in the complete database but assigned outside the modelling scope. A record was retained for modelling when it contained a numerical Young's modulus, an identifiable publication, and sufficient compositional information to calculate the titanium balance and the required descriptors. Reported elemental contents were converted to a common weight-percent representation and normalized as described in Section 3.3. Yield strength and ultimate tensile strength were treated as separate targets. Their modelling sets were constructed using the same composition and scope criteria, with the additional requirement that the corresponding mechanical property was available.

Potential transcription errors and physically unusual values were examined using two model-independent checks. The first compared the measured modulus, E, with the composition-weighted theoretical modulus, EROM. A ratio E/EROM below 0.35 was used as a warning for primary-source inspection. This threshold was not used for automatic exclusion because low ratios can occur in compliant metastable alloys. A robust standardized score, calculated from the median and median absolute deviation of E/EROM, was used as an additional indication of unusually low or high values.

The second check compared each record with chemically similar records reported in other publications. Similarity was evaluated using e/a, Bo, Md, $[Mo]_{eq,B}$, Δr, ΔL_1, density, and shear modulus. Each descriptor was scaled to the interval from zero to one. Missing numerical values were replaced by the median only for this diagnostic calculation. For each record, the five nearest records from other publications were identified. The difference between its measured modulus and the median modulus of these neighbours was then divided by their robust spread, calculated from the median absolute deviation. A minimum spread of 3 GPa was imposed to avoid unstable standardized values when the neighbouring records had very similar modulus. Absolute standardized differences greater than three were flagged for inspection.

Neither of these checks was used to identify a record as erroneous or to remove it automatically. Their purpose was to identify records that required verification against the primary source. A value was corrected only when the original publication supported a different composition, unit, measurand, or processing description. Duplicate database entries referring to the same reported physical measurement were consolidated. Separate processing states and independent measurements were retained when the distinction was supported by the source.

Reproducibility for nominally repeated compositions was evaluated separately from the model residuals. Composition groups were formed using deterministic complete-linkage clustering. Two groups could be merged only if every pair of records in the resulting group differed by no more than 0.6 wt.% for each elemental content. The closest eligible groups were merged first, while stable database identifiers were used to resolve ties. This procedure makes the grouping independent of row order, prevents a record from belonging to more than one group, and ensures that the composition tolerance is satisfied for every pair of records within a group. Only groups containing records from at least two different publications were considered.

For each composition group, the modulus range was calculated as the difference between the highest and lowest reported values. A processing signature based on product form, mechanical treatment, heat treatment, and reported deformation was then used to identify records representing the same processing state. The largest modulus range among records with an identical processing signature was recorded separately. The complete group range therefore represents the literature variation at approximately the same composition, while the same-state range provides a stricter estimate of variation between publications and measurements under comparable processing conditions. The resulting distributions are presented in Section 4.3.

Importantly, no record was removed on the basis of its model residual. The modelling domain was defined before model fitting using only the criteria described above. This avoids improving the apparent model performance by excluding difficult observations after their prediction errors are known. The records affected by these criteria and the results of their primary-source verification are reported in Section 4.3.

3.3 Feature construction

Elemental contents provide the most direct description of alloy chemistry, but phase stability and elastic response also depend on electronic structure, atomic size, and bonding. The compositions were therefore transformed into a set of physically motivated numerical descriptors and two composition-based classes. All descriptors were calculated before model fitting using the same equations and elemental constants for every record.

The input compositions were expressed in weight percent and normalised to 100 wt.%, with titanium treated as the balance when it was not reported explicitly. The elemental input set contained 12 components: Ti, Fe, Mn, Mo, Nb, O, N, C, Si, Sn, Ta, and Zr. Weight percentage, w_i, was converted to atomic percentage, x_i, according to:

$$x_i = 100 * \frac{w_i/M_i}{\sum(w_i/M_i)}, \tag{6}$$

where M_i is the atomic mass of element *i*.

Elemental contents not reported in the source were entered as zero. For substitutional solutes, an unlisted intentional addition was treated as absent. For O, N, and C, however, zero represents an unreported interstitial content and does not imply physical absence. This convention may therefore underestimate the contribution of interstitial elements to the calculated descriptors. Sixteen continuous descriptors were calculated from the resulting compositions. The electron-to-atom ratio, e/a, represents the average number of valence electrons per atom. The bond order, Bo, represents the average bond-strength parameter assigned to the constituent elements within the d-electron approach,

while the d-orbital energy level, Md, combines electronic and atomic-size contributions and is commonly used as an indicator of β-phase stability. These descriptors were calculated as atomic-fraction-weighted averages of their elemental values,

$$D_{alloy} = \sum_i \frac{x_i}{100} D_i, \quad (7)$$

The same atomic-fraction weighting was used for specific heat, bulk modulus, shear modulus, theoretical Young's modulus, ΔL1, and Δr. The four property-based descriptors provide composition-weighted estimates of thermal response, volumetric stiffness, shear stiffness, and elastic stiffness based on elemental constants. They describe the nominal alloy composition rather than its experimentally measured properties. In particular, the theoretical Young's modulus, EROM, was kept separate from the measured Young's modulus used as the prediction target.

The two size-related descriptors describe different forms of mismatch. For each element i, the atomic-size difference relative to titanium was defined as:

$$\Delta r_i = r_i - r_{Ti}, \quad (8)$$

where *r* is the metallic radius in picometres. The alloy value, *Δr*, was calculated as the atomic-fraction-weighted average of the signed elemental differences. A negative value therefore indicates that the solute atoms are, on average, smaller than titanium.

The crystallographic mismatch was described using the ΔL_1 parameter, calculated as a composition-weighted descriptor following the approach used in the previous database and modelling workflow (Marković et al., 2023):

$$\Delta L_1 = \sum_i \frac{x_i}{100} \frac{100(L_{1,i} - L_{1,Ti})}{L_{1,Ti}}, \quad (9)$$

where $L_{1,i}$,i is the first tabulated lattice parameter of pure element *i*. Positive and negative values indicate the weighted direction of the difference relative to titanium. Since these elemental parameters correspond to the stable crystal structures of the pure elements, ΔL_1 should be interpreted as a heuristic composition descriptor rather than as the elastic lattice strain of the experimental multiphase alloy.

Weighted molar mass and density were used to describe the mass and packing contributions of the constituent elements. Both were calculated as linear weight-fraction descriptors:

$$P_{alloy} = \sum_i \frac{w_i}{100} P_{i,} \quad (10)$$

Five empirical molybdenum-equivalent formulations were also calculated in weight percent:

$$[Mo]_{eq,B} = Mo + 0.28Nb + 0.22Ta + 2.9Fe + 1.54Mn, \quad (11)$$

$$[Mo]_{eq,Z} = Mo + 0.39Nb + 0.28Ta + 2.20Fe + 1.69Mn, \quad (12)$$

$$[Mo]_{eq,W1} = Mo + 0.28Nb + 0.22Ta + 1.93Fe + 2.26Mn + 0.3Sn + 0.47Zr + 3.01Si, \quad (13)$$

$$[Mo]_{eq,W1} = Mo + 0.30Nb + 0.30Ta + 1.23Fe + 1.42Mn + 0.38Sn + 0.34Zr + 0.99Si, \quad (14)$$

$$[Mo]_{eq,Chen} = Mo + \frac{Nb}{3.6} + \frac{Ta}{4.5} + \frac{Fe}{0.35} + \frac{Mn}{0.65}, \quad (15)$$

where all elemental symbols represent concentrations in wt.%. The five formulations were initially retained separately because they represent different published calibrations of β-phase stabilisation.

Two categorical features were generated from pairs of continuous descriptors. For the Bo–Md classification, the calculated coordinates were compared with the digitised Ms, Mf1, Mf2, and α boundaries reported by Abdel-Hady et al. (2006). Linear interpolation along these boundaries was used to assign each composition to one of five regions: β slip, β + ω/twinning, α′ + α″, α + β, or α. The second classification was based on e/a and Δr and the polygonal twinning boundary reported by Rabadia et al. (2021). A point-in-polygon test assigned compositions located within this boundary to the twinning region, while the remaining compositions were assigned to the slip region. Both classifications were based only on composition-derived descriptors. Experimentally reported phases and deformation mechanisms were not used to assign the labels.

The initial candidate set contained 30 features: 12 elemental contents, 16 continuous descriptors, and two categorical features. Experimental Young's modulus was not used in any feature or classification calculation. The legacy variable Yls was also excluded because its elemental coefficients had been fitted to measured modulus and would therefore introduce information derived from the prediction target.

A sensitivity representation was additionally considered for the interstitial and molybdenum-equivalent variables. The three interstitial contents were combined into an oxygen-equivalent content:

$$O_{eq} = O + 2N + \frac{2}{3}C, \quad (16)$$

expressed in weight percent. A binary reporting indicator was set to one when at least one positive O, N, or C content was reported in the source and to zero otherwise. Together, these two variables allow the model to distinguish a reported interstitial contribution from the zero convention used for missing interstitial information. In the same representation, the five correlated molybdenum-equivalent expressions were replaced by a single variable, $[Mo]_{eq,W1}$.

The original 16-descriptor representation was retained unless the alternative representation reduced the pooled MAE by at least 0.25 GPa and also produced a lower MAE in at least four of the five publication grouped outer folds. This decision rule was defined before the alternative representation was evaluated, so the choice of representation could not be adjusted after the results were known.

3.4 Machine learning methodology

Machine learning was used to estimate Young's modulus, yield strength, and ultimate tensile strength from the available alloy information. The prediction of these three properties in biocompatible titanium alloys was addressed in the author's earlier study (Marković et al., 2024), and the methodology described here extends that work through publication grouped validation and the revised database described in Section 3.1. Young's modulus was the primary target, since it had the broadest literature coverage and was used in the subsequent composition screening. The same validation principle was applied to every property: a reported performance value had to describe predictions for publications that were absent during model fitting. The overall workflow, from the assembled database through to the screening of new compositions, is summarized in Figure 3.1.

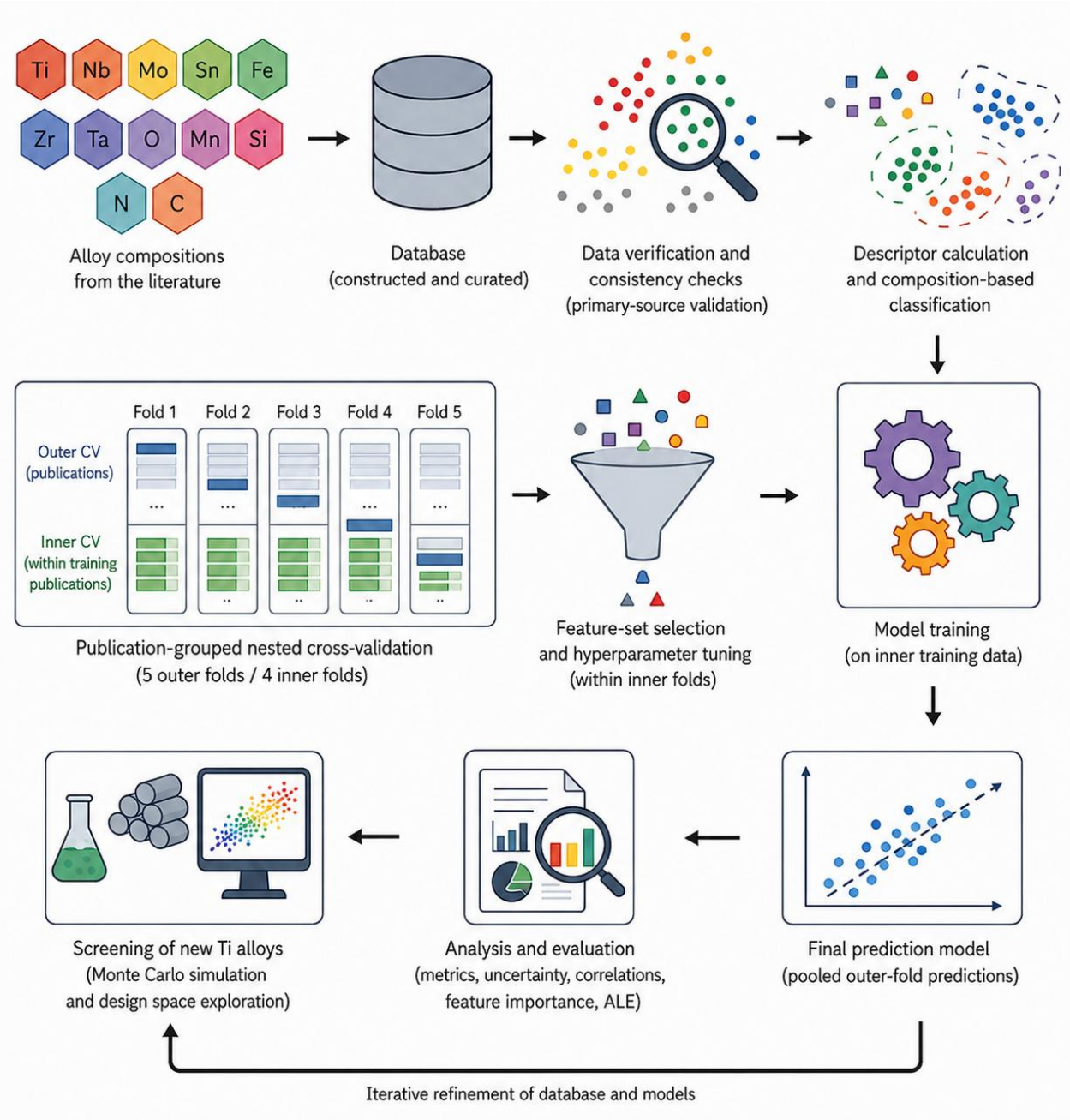

Figure 3.1. Workflow used for machine-learning prediction of mechanical properties in biocompatible titanium alloys, from database construction to the screening of new alloy compositions.

Records from a single publication often share alloy preparation, equipment, calibration, and reporting practice, and treating them as independent during data splitting can place closely related measurements in both the training and the test set. The primary validation therefore grouped records by publication. Five outer folds were used to generate predictions for the excluded publications, and within every outer training set four additional publication grouped folds selected the feature set and the model hyperparameters by the lowest mean absolute error. Preprocessing, feature-set selection, and hyperparameter selection were repeated inside each outer fold, and the outer test publications were used only once, after these decisions had been made.

A shuffled five-fold split of individual records was carried out as a secondary comparison with the conventional validation used in earlier modelling studies. Because that split allows records from the same publication to fall on both sides of a fold, it tests an easier prediction task, so the

publication grouped result was kept as the main estimate of generalisation to an unseen literature source.

Four composition-based feature sets were compared: the 12 elemental contents; the 16 derived descriptors; the combination of the 12 contents and 16 descriptors; and the full set with the two composition-based class labels. A separate process-aware set added treatment temperatures and times, deformation information, production-route indicators, heat-treatment indicators, and flags showing whether the selected process values were reported. The process-aware analysis measured the information carried by the available processing metadata, but the composition-based model remained the primary design model, because process conditions are unavailable when a new chemical composition is first screened.

Six regression algorithms were evaluated, and their hyperparameters were searched within the inner folds using the grids summarised in Table 3.1. The grids were kept deliberately compact to limit selection variance in a small literature dataset.

Table 3.1. Hyperparameter grids searched within the inner publication grouped folds for the six regression algorithms.

Algorithm	Fixed settings	Parameters searched
Ridge regression	standardized inputs	regularization α = 1, 10, or 100
Support vector regression	radial-basis kernel; standardized inputs	C = 10 or 100; ε = 5 or 10
Random Forest	300 trees	fraction of features per split = 0.6 or 1.0; minimum leaf size = 1 or 3
Extra Trees	300 trees	fraction of features per split = 0.6 or 1.0; minimum leaf size = 1 or 3
Gradient Boosting	Huber loss; 300 trees; learning rate = 0.03	maximum depth = 1 or 2; minimum leaf size = 2 or 5
XGBoost	squared-error objective; 300 trees; learning rate = 0.03; row and feature subsampling = 0.8; L2 regularization = 10	maximum depth = 2 or 3; minimum child weight = 1 or 4

Missing numerical inputs were replaced by the median calculated from the corresponding training data. Ridge regression and support vector regression additionally used a standardisation fitted on the training data, while the tree-based models used the imputed values directly, and a fixed random seed ensured reproducibility. Once the Young's modulus comparison had selected an algorithm, the same algorithmic framework was applied to yield strength and ultimate tensile strength, so that differences among the properties reflect the available data and the behaviour of the target rather than a change of method.

A predictor equal to the mean target value of the training fold provided the reference error for Young's modulus, while Ridge regression provided a second, linear reference. Performance was evaluated from the pooled outer-fold predictions using the coefficient of determination, R^2, mean absolute error (MAE), root mean square error (RMSE), and median absolute error. MAE gives the average absolute prediction error in the units of the property, while RMSE gives greater weight to

larger errors. R^2 describes how much of the observed variation is reproduced by the model and becomes negative when the model performs worse than the training-mean reference. For Young's modulus, the proportions of predictions within ±10 and ±20 GPa were also calculated.

Uncertainty in the performance estimates was obtained by resampling complete publications with replacement. For each of 2,000 bootstrap samples, all records belonging to a selected publication were included together and the metric was recalculated from the pooled out-of-fold predictions, with the 2.5th and 97.5th percentiles forming the reported 95% interval. This procedure preserves the dependence among records that originate from the same source.

Associations between categorical groups and continuous properties were quantified using η^2, which represents the fraction of the total variation associated with differences between group means. The bias-corrected ω^2 was reported alongside η^2 because η^2 can overestimate the effect when some groups contain few records. Statistical significance was assessed using 10,000 random permutations of the group labels. Correlations were evaluated using Pearson's r together with a permutation test and a 2,000-sample publication-level bootstrap interval. Their sensitivity to individual sources was additionally examined by recalculating each correlation after removing one publication at a time. These analyses describe associations within the collected literature and were not interpreted as evidence of an independent causal effect of an element, descriptor, or measurement category.

Feature importance was evaluated using a fixed 30-feature Random Forest, ensuring that the same features and feature groups were available in every outer fold. Within each fold, each feature was randomly permuted 100 times among the excluded records, and the resulting increase in MAE was used as its importance measure. Physically related features were also permuted as groups. This grouped analysis was included because several descriptors contain similar information, and the importance of an individual feature may appear small when another related descriptor remains available to the model.

Accumulated local effects (ALE) curves were used to examine the learned response for selected descriptors. The observed range of each descriptor was divided into eight quantile intervals. Within each interval, predictions at the lower and upper boundaries were compared only for records located in that part of the data space. The resulting local differences were then accumulated and centred. This approach keeps the interpretation within the combinations represented in the database. A two-dimensional second-order ALE calculation was also used to examine the joint Mo–Sn contribution. A map cell was interpreted only when it contained at least three records from at least two publications.

Feature interpretation followed the same five outer and four inner publication grouped folds used for performance estimation. The hyperparameters of the interpretation model were selected using only the training publications within each outer fold. The predefined rule for accepting an alternative descriptor representation is given in Section 3.3.

3.5 Computational design

Computational screening was used to examine the Ti–Mo–Sn composition space at a resolution that would be impractical to cover experimentally. Mo and Sn were varied independently from 0 to 16 wt.% in steps of 0.2 wt.%, with Ti as the balance and all other elemental contents set to zero. This regular grid provides uniform and reproducible coverage of the ternary section and includes the Ti–6.2Mo base composition used for experimental validation. V, Al, Ni, Co, Cu, and Cr were excluded in line with the cytotoxicity-based element-selection criteria established in Chapter 2.

The search was restricted to Ti–Mo–Sn because this system was selected for experimental validation and could be enumerated completely at the chosen resolution. A broad stochastic search would distribute candidates across many multicomponent systems without providing additional literature support for the Ti–Mo–Sn predictions. The regular grid also allows composition, prediction, and applicability-domain support to be represented on the same plane.

The composition-derived descriptors were calculated for every candidate using the equations and elemental constants defined in Section 3.3. A Random Forest was then fitted to the complete Young's modulus modelling domain. Its maximum-feature fraction and minimum leaf size were selected by publication grouped validation. The resulting final model was used to rank the generated candidates, while its expected generalisation performance was estimated using the nested publication grouped procedure described in Section 3.4.

The screening model contains no processing variables, so its predictions represent the composition–modulus relationship across the processing and phase states represented in the literature. No heat-treatment or deformation state was assigned to the generated compositions. The predicted modulus should therefore be interpreted as a screening estimate for composition selection rather than as a prediction for a specific thermomechanical condition.

Prediction uncertainty was described using two complementary measures. First, absolute residuals from the publication grouped out-of-fold predictions were used to determine error limits containing 80, 90, and 95% of the database observations. These limits describe the prediction errors observed when complete publications were excluded from model training. Second, the five models fitted to the outer training folds were applied to every candidate, and the standard deviation of their predictions was calculated. This value reflects the sensitivity of a candidate prediction to the publications available for model fitting and was therefore interpreted as a measure of model stability rather than as a calibrated prediction error.

The applicability domain was defined using a reduced descriptor space containing e/a, Bo, Md, $[Mo]_{eq,W1}$, weighted molar mass, ΔL_1, Δr, and theoretical Young's modulus. These eight descriptors represent electronic structure, β-phase stability, mass, atomic-size effects, and rule-of-mixtures stiffness, while avoiding the inclusion of multiple strongly correlated descriptors. Missing values were replaced with the training medians, and each descriptor was centred by its median and scaled by its interquartile range.

For each database record, the mean distance to its five nearest remaining database records was calculated. The 95th percentile of these leave-one-out distances was used as the applicability-domain threshold. The mean distance from each candidate to its five nearest database records was then calculated in the same scaled descriptor space, and candidates with distances at or below this threshold were classified as being inside the applicability domain.

Dependence on a single literature source was examined by removing the complete Ti–8Mo–xSn series reported by Li et al. (2023). Model selection was repeated using the remaining publications, and the excluded series was then predicted. This source was selected in advance because it provides direct experimental evidence for the Sn-dependent trend within the screened system. The test therefore examines whether the Mo–Sn prediction trend can be recovered from the remaining literature rather than being determined by this single experimental series.

Selection bias at the lower end of the predicted modulus range was estimated using the five outer validation folds. Within each excluded fold, the record with the lowest predicted modulus was treated as a pseudo-screening winner, and its predicted value was compared with the measured value. Repeating this procedure across genuinely excluded data provides an estimate of the optimism introduced when many candidates are screened and only the lowest predicted value is selected. The resulting bias was used to interpret the ranking of the best computational candidates within a more realistic error range.

3.6 Experimental procedure

3.6.1 Alloy manufacturing

The Ti–6.2Mo and Ti–6.2Mo–xSn (x = 5, 10, 15 wt.%) compositions were selected on the basis of the machine-learning screening of the Ti–Mo–Sn system described in Section 3.5, which

identified a promising low modulus region; the selected series traverses the predicted modulus gradient at a fixed Mo content while remaining within the applicability domain of the model. The predictions and the selection procedure are presented in Section 4.6

The selected alloys were synthesized using an arc melting system (AM, Edmund Bühler GmbH, Germany) on a water-cooled copper hearth under a purified argon atmosphere. Commercially pure raw elements were used as starting materials: Ti (99.9%), Mo (99.95%), and Sn (99.99%, ONYXMET). Prior to melting, the chamber was evacuated and purged three times with high-purity argon (6N) in order to minimize oxygen contamination. A titanium getter was additionally melted before alloy preparation to further purify the atmosphere. Each ingot was remelted at least six times to improve chemical homogeneity. The overall processing route adopted in this study is schematically presented in Figure 3.2.

The alloy ingots were subsequently heat treated at 1000 °C for 2 h for homogenization in evacuated quartz tubes, followed by water quenching achieved by breaking the quartz tubes directly into water. After heat treatment, the alloys were cold rolled to a thickness reduction of approximately 20%.

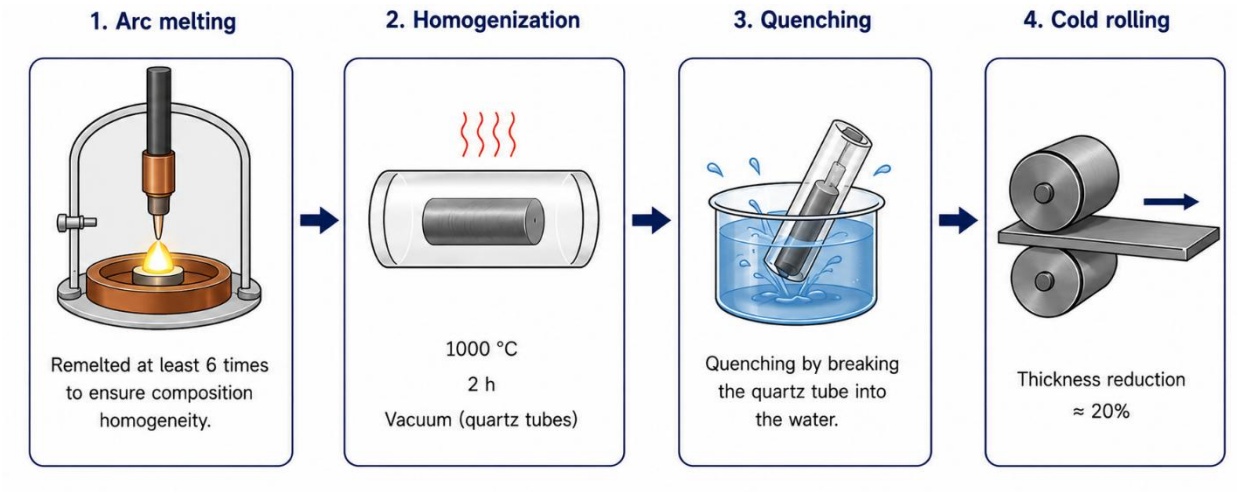

Figure 3.2. Schematic representation of the alloy manufacturing process.

3.6.2 Density measurements

The density of the synthesized alloys was determined at room temperature using the Archimedes method in distilled water. The measurements were performed using an analytical balance, and the quantities G, M, G_1, and G_2 were recorded for each sample, where G represents the dry sample mass, M the mass of the suspension mesh immersed in water, G_2 the combined mass of the immersed mesh and sample, and G_1 the mass of the saturated sample.

The density was calculated according to Equation (17):

$$\rho = \frac{G*\rho_w}{G_1+M-G_2}, \tag{17}$$

where ρ_w is the density of distilled water at the measurement temperature.

The theoretical density was calculated using the rule of mixtures based on the nominal alloy compositions. In addition, the open porosity of the alloys was evaluated using the Archimedes method. The open porosity was calculated according to Equation (18):

$$P_{open}(\%) = \frac{G_1-G}{G_1+M-G_2} * 100. \tag{18}$$

The measured values used for density and porosity calculations are summarized in Table 3.2.

Table 3.2. Measured masses used for density and open porosity calculations according to the Archimedes method.

Alloy	G (g)	M (g)	G_2 (g)	G_1 (g)
Ti–6.2Mo	5.5187	10.9165	15.2580	5.5192
Ti–6.2Mo–5Sn	4.8189	10.9723	14.7816	4.8195
Ti–6.2Mo–10Sn	4.2658	10.9755	14.3592	4.2669
Ti–6.2Mo–15Sn	4.7615	10.9255	14.7319	4.7620

3.6.3 Phase and microstructural characterization (XRD, SEM, EDS)

The phase composition and structural parameters of the synthesized alloys were determined by the X-ray diffraction (XRD). The analysis was performed on a Rigaku Ultima IV diffractometer with Ni-filtered Cu Kα radiation (λ = 0.1540 nm). The generator voltage and current were 40 kV and 40 mA, respectively. Continuous scanning was performed over the 30–90° 2θ range, using a step size of 0.02° and a scanning speed of 10°/min. PDXL2 software (version 2.0.3.0) with reference to the International Centre for Diffraction Data (ICDD) database was used for phase identification and determination of structural parameters.

Microstructural observations and compositional analysis were performed using a FEI Nova Nano 450 scanning electron microscope (SEM) equipped with an EDAX Octane Elect energy-dispersive spectroscopy (EDS) microanalyzer. SEM-EDS analysis was carried out using a beam voltage of 20 kV and a spot size of 5.

The alloy compositions determined by EDS analysis were further used to calculate the theoretical density and, subsequently, the relative density of the synthesized alloys.

3.6.4 EBSD analysis and crystallographic orientation mapping

Prior to EBSD analysis, the samples were mechanically ground using SiC papers from 320 to 4000 grit, followed by polishing with a diamond suspension and final chemo-mechanical polishing using an OPS colloidal silica suspension. The samples were subsequently cleaned in an ultrasonic cleaner.

Crystallographic orientation analysis was performed using a Helios 5 UX scanning electron microscope (Thermo Fisher Scientific) equipped with an EBSD detector (EDAX Velocity Pro). EBSD data were acquired in the form of inverse pole figure (IPF) orientation maps and phase maps using an accelerating voltage of 20 kV and a step size of 0.4 μm.

Post-processing was carried out using OIM Analysis 8 software. As a clean-up procedure, grain confidence index (CI) standardization was applied, followed by removal of points with CI values below 0.1.

3.6.5 Nanoindentation measurements

Nanoindentation measurements were performed using a Hysitron TI 950 TriboIndenter equipped with a Berkovich diamond indenter. Nanohardness and reduced elastic modulus were determined from the load–displacement curves using the Oliver–Pharr method (Oliver and Pharr, 1992; Oliver and Pharr, 2004). A maximum load of 5 mN was applied, with a holding time of 10 s at maximum load and loading and unloading rates of 250 μN/s. A total of 24 indentations were performed on each alloy.

For comparison with the machine-learning predictions, the reduced elastic modulus obtained by nanoindentation was converted to the specimen Young's modulus using the relationship:

$$\frac{1}{E_r} = \frac{1-\nu_s^2}{E_s} + \frac{1-\nu_i^2}{E_i} \tag{19}$$

where E_r is the reduced elastic modulus, E_s and ν_s are the Young's modulus and Poisson's ratio of the specimen, and E_i and ν_i are the corresponding elastic properties of the indenter. A Poisson's ratio of 0.34 was assumed for all investigated alloys, while the elastic constants of the diamond indenter were taken as E_i=1140 GPa and ν_i=0.07 (Fukuhara and Sanpei, 1993; Cheng and Cheng, 1998). The same values were used for all specimens, providing a consistent conversion of E_r to E_s within the experimental series.

3.6.6 Quantitative analysis of α-lamellar microstructure using MIPAR

Quantitative characterization of the α-lamellar microstructure was performed using MIPAR™ v4.50 software (Sosa et al., 2014), which is based on the MATLAB environment. The analysis procedure is illustrated in Figure 3.3. First, the original EBSD inverse pole figure (IPF) map was imported into the software (Figure 3.3(a)). Based on the color information associated with crystallographic orientation in the IPF map, α lamellae were identified and segmented from the surrounding microstructure using color-based selection criteria (Figure 3.3(b)). Small discontinuities within the segmented lamellae were removed through morphological dilation and erosion operations to obtain continuous regions for subsequent quantitative analysis.

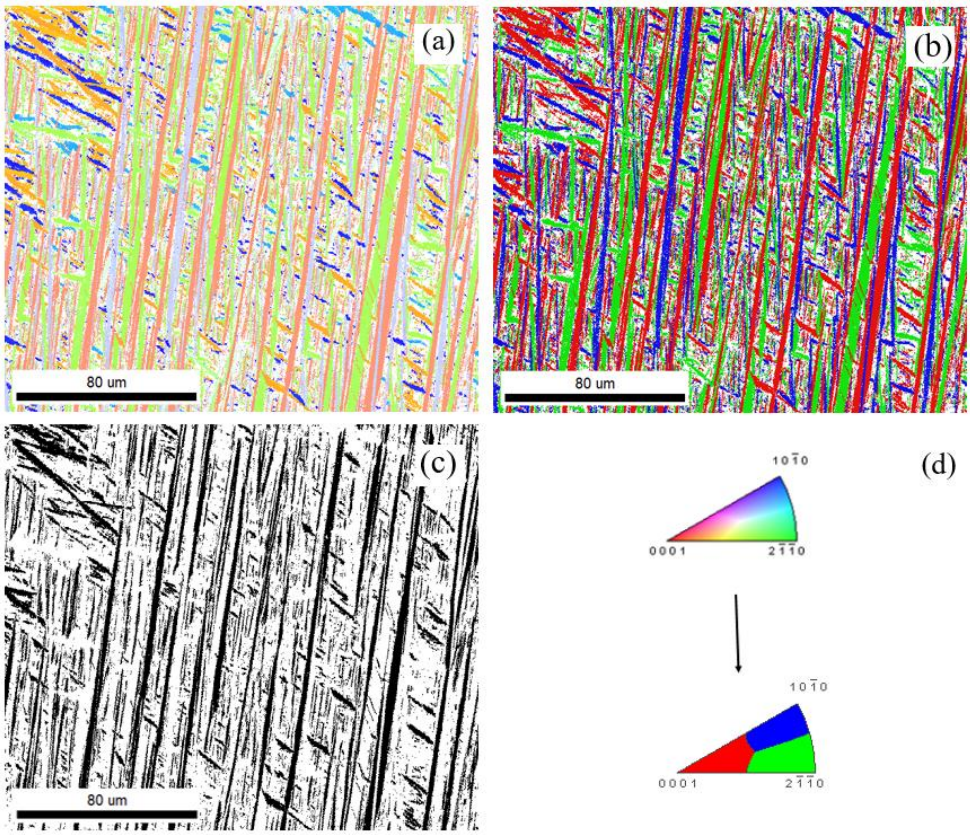

Figure 3.3. MIPAR-based workflow used for quantitative characterization of the α-lamellar microstructure in the Ti–6.2Mo alloy. (a) Original EBSD inverse pole figure (IPF) map used as input for the analysis. (b) Segmentation of α lamellae from the IPF map. (c) Example of orientation-specific segmentation corresponding to the [0001] orientation group used for thickness measurements. (d) Schematic illustration of the classification of lamellae into three dominant orientation groups ([0001], [10$\bar{1}$0], and [2$\bar{1}\bar{1}$0]) for orientation-resolved quantitative analysis.

The segmented lamellae were subsequently classified according to their crystallographic orientation into three groups centred around [0001], $[10\bar{1}0]$, and $[2\bar{1}\bar{1}0]$, based on the colour ranges defined from the IPF map. An example of the segmentation corresponding to the [0001] orientation group is shown in Figure 3.3(c), while the classification into all three orientation groups is illustrated in Figure 3.3(d). The colour-selection criteria used for the orientation classification are summarized in Table 3.3. Saturation and Value ranges were kept between 0 and 255 for all orientation groups to cover the full colour intensity range of the IPF maps.

Table 3.3. Color-selection criteria used for segmentation of the dominant α-lamella orientation groups in MIPAR.

Orientation group	Hue range
$[10\bar{1}0]$	188–281
$[2\bar{1}\bar{1}0]$	72–188
[0001]	0–72 ∪ 281–360

The area fraction of each orientation group was determined using the Measure Image function, while lamellar thickness was evaluated using the Local Measurements module and the Advanced Measure Thickness procedure. This classification enabled independent determination of lamellar thickness and area fraction for each orientation group.

3.7 Thermodynamic calculations

Equilibrium phase diagrams of the Ti–Mo and Ti–Sn binary systems, together with isothermal sections of the ternary Ti–Mo–Sn system at 1000 °C and 100 °C, were calculated using the PanPhaseDiagram module of the PANDAT software (Cao et al., 2009) with the PanHEA thermodynamic database. The calculations were used to identify the equilibrium phase fields relevant to the homogenisation temperature and to assess how Sn additions modify phase stability in the Ti-rich region of the system. The calculated diagrams are presented and discussed in Section 4.8.

3.8 Atomistic simulations of nanoindentation

Molecular dynamics simulations of nanoindentation in single-crystal α-Ti were performed using the LAMMPS code (Thompson et al., 2022) with an embedded-atom method interatomic potential developed for titanium (Mendelev et al., 2016); the full simulation protocol is described in Markovic and Dominguez-Gutierrez (2026). Simulation cells containing 4.25×10^6 to 7.3×10^6 atoms were constructed for the [0001], $[10\bar{1}0]$, and $[2\bar{1}10]$ orientations. After energy minimisation with the FIRE 2.0 algorithm, the samples were thermalised at 10, 300, and 600 K using a Nose–Hoover NPT thermostat, with a timestep of 1 fs. Indentation was performed with a rigid spherical indenter of radius 12 nm at a constant velocity of 20 m s^{-1}, with periodic boundary conditions applied along the x and y directions and a maximum indentation depth of 4 nm. Load–displacement curves were obtained from the indenter force, and the contact pressure was evaluated using the Pathak formulation (Pathak and Kalidindi, 2015). Local atomic structures were identified by the polyhedral template matching method and dislocation structures were extracted with the dislocation extraction algorithm, both implemented in OVITO (Stukowski, 2010), while Schmid factor mapping was used to connect slip-system activation with the resolved shear stress beneath the indenter. Since the indentation velocity accessible to molecular dynamics is several orders of magnitude higher than in experimental nanoindentation, the simulations at 300 K are used for a qualitative, mechanism-level interpretation of the orientation-dependent response discussed in Section 4.9.

4. Results and discussion

4.1 Dataset statistics

The first step of the analysis was to examine the statistical characteristics of the constructed database. The complete database contains 280 experimental records. Of these, 240 records from 77 primary publications form the modelling domain used for Young's modulus in this section. The remaining 40 records were retained in the database for traceability but excluded from the modelling domain because their measured quantity or processing route falls outside its predefined scope. These exclusions are examined in detail in Section 4.3. The 240 modelling records represent 201 alloy designations and 181 distinct composition vectors. Repeated compositions correspond to different processing states, measurement conditions, or independent publications.

The measured Young's modulus ranged from 29.0 to 133.2 GPa, with a mean of 67.8 GPa and a median of 64.8 GPa. The relatively small difference between the mean and median is consistent with the mild positive skewness of the distribution (0.69). The standard deviation is 19.9 GPa, and 166 records (69.2%) fall within one standard deviation of the mean, between 47.9 and 87.7 GPa. The coefficient of variation is 29.4%, while the central half of the observations lies between 52.4 and 80.7 GPa. As shown in Figure 4.1, the distribution is unimodal, with a modest tail toward higher modulus values.

The reference ranges included in Figure 4.1 place these values in a biomedical context. Ti-6Al-4V has a Young's modulus of approximately 110 GPa (Niinomi and Nakai, 2011), and 233 records (97.1%) in the modelling domain are below this value. Cortical bone has an approximate Young's modulus range of 10–30 GPa (Beisekenov et al., 2025), and only two records fall within this range. The database contains 100 records below 60 GPa, 46 below 50 GPa, and only 8 below 40 GPa, showing that experimental data become increasingly sparse toward the lowest-modulus region. The extent to which compositions predicted in this region remain within the descriptor space represented by the experimental data is examined through the applicability-domain analysis in Section 4.6.

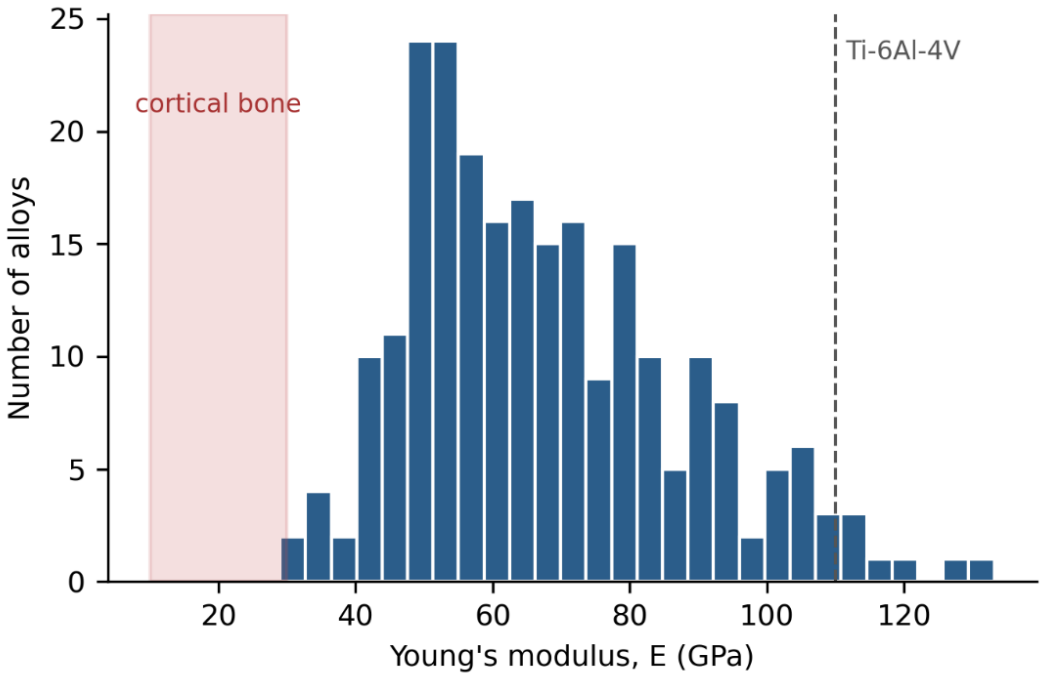

Figure 4.1. Distribution of measured Young's modulus in the modelling domain. The shaded region marks the approximate cortical-bone range, and the dashed line marks the reference value for Ti-6Al-4V.

To organise the data by composition, alloy systems were defined from the two most abundant alloying additions present at concentrations of at least 2 wt.%, with element symbols written in a fixed canonical order so that every ternary composition is assigned to a single system. This procedure yields the 17 systems summarised in Table 4.1.

Table 4.1. Young's modulus by alloy system, ordered by the number of records.

Alloy system	Records	Mean E (GPa)	Median E (GPa)	SD (GPa)	Range (GPa)
Ti-Nb-Zr	84	60.4	56.0	17.1	29.0–109.0
Ti-Nb-Sn	33	55.0	55.0	10.1	33.0–80.6
Ti-Nb	21	69.9	65.0	16.5	39.0–109.0
Ti-Nb-Ta	17	58.8	55.0	13.7	43.0–87.1
Ti-Mo-Zr	15	76.8	78.0	12.7	52.0–108.0
Ti-Nb-Mo	13	66.9	69.0	17.8	35.4–98.0
Ti-Nb-Fe	13	90.2	90.0	11.2	64.0–112.0
Ti-Mo	10	89.2	83.4	23.8	58.6–133.2
Ti-Zr-Sn	8	68.6	69.0	9.8	52.6–79.8
Ti-Mo-Sn	7	63.2	66.9	11.7	46.8–76.8
Ti-Ta-Fe	6	104.9	104.5	9.5	92.0–119.0
Ti-Mo-Mn	4	92.8	91.0	4.9	89.0–100.0
Ti-Mn	4	107.0	102.5	15.3	94.0–129.0
Ti-Mo-Ta	2	74.0	74.0	0.0	74.0
Ti-Ta	1	67.0	67.0	-	67.0
Ti-Ta-Zr	1	69.9	69.9	-	69.9
Ti-Fe	1	118.0	118.0	-	118.0

The literature coverage is strongly concentrated in niobium-containing systems: the five Nb-based systems together account for 168 of the 240 records, whereas six systems are represented by four records or fewer. Ti-Mo-Sn, the system selected later for experimental investigation, is represented by only seven records, with a mean modulus of 63.2 GPa; its small sample size provides a limited empirical basis for composition selection within this ternary system.

The individual system distributions differ in both position and width (Figure 4.2). Ti-Nb-Sn, Ti-Nb-Ta, and Ti-Nb-Zr occupy the lower part of the distribution, with mean values of 55.0, 58.8, and 60.4 GPa, whereas Ti-Nb-Fe, Ti-Ta-Fe, Ti-Mo-Mn, and Ti-Mn show substantially higher means. These differences reflect the sampled alloy and processing states; phase constitution,

thermomechanical history, interstitial content, and measurement conditions all remain potential sources of variation within each compositional system.

The dispersion within individual systems is also substantial. The standard deviation reaches 17.1 GPa for Ti-Nb-Zr and 23.8 GPa for Ti-Mo, compared with a span of about 50 GPa between the mean values of the systems represented by more than five records. Alloy-system identity therefore reduces compositional ambiguity, but still leaves a broad range of possible modulus values.

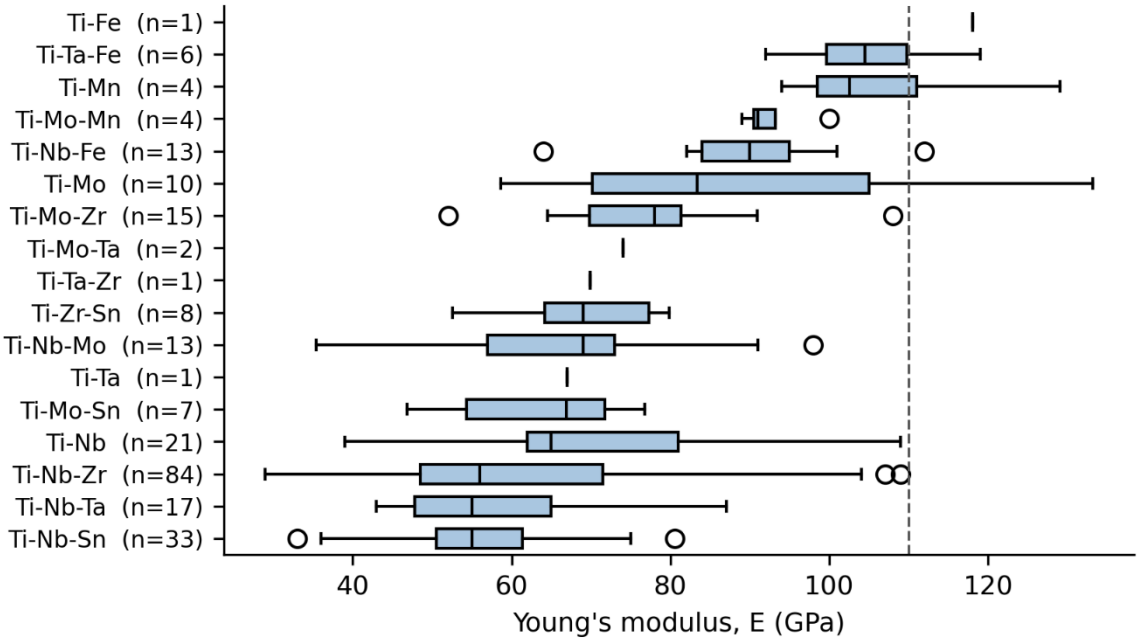

Figure 4.2. Distribution of Young's modulus across the 17 canonical alloy systems. Systems are ordered by median modulus; sample size is shown beside each system, and the dashed line marks the reference value for Ti-6Al-4V.

The records were then grouped by alloy system to examine how much of the variation in Young's modulus is associated with differences between systems such as Ti-Nb-Zr, Ti-Mo-Sn, and others. This contribution was quantified using η^2. The obtained value of $\eta^2 = 0.457$ indicates that differences between the mean modulus of the 17 systems account for 45.7% of the variation across the 240 records. The remaining 54.3% occurs within individual alloy systems and reflects differences in composition, processing state, phase constitution, and other unrecorded or incompletely recorded factors.

Since η^2 can overestimate the effect of grouping when groups differ in size or contain only a small number of records, the corrected coefficient ω^2 was also calculated. The obtained value of $\omega^2 = 0.417$ is close to η^2 and indicates that approximately 40% of the observed variation in Young's modulus is associated with alloy-system identity.

The statistical significance of this association was evaluated using a permutation test, in which the alloy-system labels of the 240 records were randomly reassigned 10,000 times. Fewer than 0.1% of the random permutations produced a separation at least as large as the observed one ($p < 0.001$), indicating that the observed differences between alloy systems are unlikely to result from random grouping.

Several records originate from the same publication and may share material preparation, equipment, and reporting practices, and therefore cannot be considered fully independent. The bootstrap analysis consequently resampled complete publications, keeping records from the same publication together. This resulted in a 95% interval of $\eta^2 = 0.29–0.68$. The association between alloy system and Young's modulus therefore remains substantial across different resamples of the available literature, although its estimated magnitude depends on the publications represented in the database.

The combinations of alloying elements represented in the database are shown in Figure 4.3. Niobium occurs in 200 records, with a mean concentration of 23.4 wt.% when present, followed by zirconium in 140 records, tin in 80, molybdenum in 79, tantalum in 66, and iron in 56. The Nb-Zr and Nb-Sn pairs dominate the co-occurrence matrix, whereas manganese and silicon occur in only eight and six records, respectively, limiting element-specific analysis for these additions. Oxygen is reported in 91 records and reaches 0.70 wt.%, while nitrogen and carbon are reported in 32 and 26 records at considerably lower concentrations. The database is therefore concentrated around a relatively small number of Nb-rich compositional regions, while several other combinations of biocompatible elements remain sparsely represented.

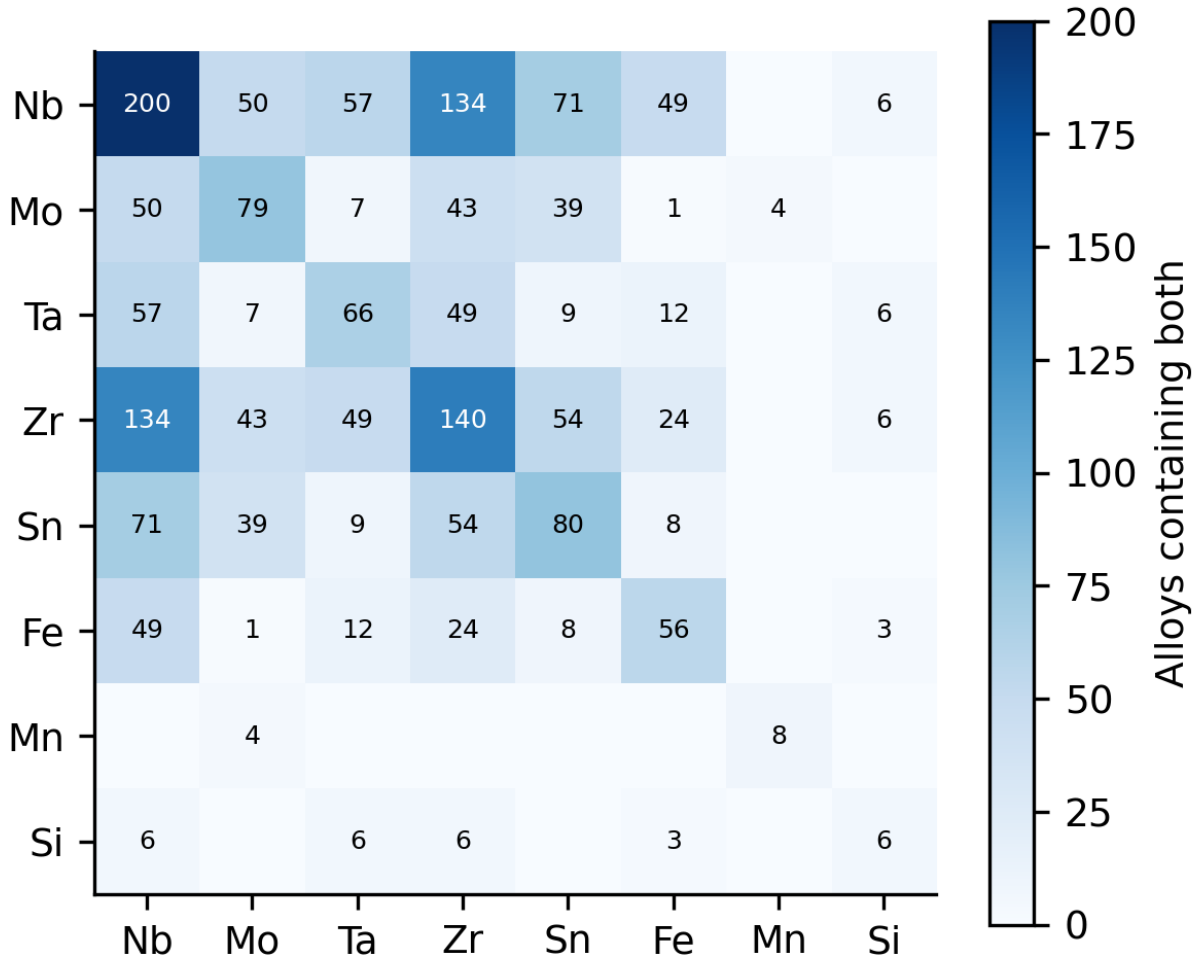

Figure 4.3. Element co-occurrence in the Young's modulus modelling domain. Each diagonal cell gives the number of alloy records containing the corresponding element. Each off-diagonal cell gives the number of alloy records containing the corresponding pair of elements.

The accompanying processing and mechanical-property metadata are less complete than the target modulus (Table 4.2). A production route is available for 176 records (73.3%) and a heat-treatment temperature for 125 (52.1%), while ultimate tensile strength, elongation, and yield strength are reported for approximately half of the modelling domain. The degree of deformation is available for only 67 records (27.9%). These coverage levels result in smaller analysis populations for strength modelling and limit the direct representation of the thermomechanical state.

Table 4.2. Availability of properties and processing metadata in the 240-record modelling domain.

Reported quantity	Records	Share of modelling domain (%)
Young's modulus	240	100.0
Production route	176	73.3
Heat-treatment temperature	125	52.1
Ultimate tensile strength	121	50.4
Elongation	114	47.5
Yield strength	113	47.1
Oxygen content	91	37.9
Mechanical treatment	91	37.9
Degree of deformation	67	27.9
Hardness	51	21.2

The possible influence of the measurement method was evaluated by grouping records according to the reported method and comparing the mean Young's modulus between groups. Measurement method accounts for only 1.4% of the total variation in Young's modulus ($\eta^2 = 0.014$), indicating that differences between the method-group means are small compared with the overall range of 29.0–133.2 GPa. The permutation test gave $p = 0.339$, with an equal or larger separation between group means obtained in 33.9% of the random permutations. The observed differences therefore provide no evidence of a systematic association between measurement method and Young's modulus in this dataset. On this basis, the methods were not ranked and records were not excluded according to measurement method alone.

As described in Section 3.2, twelve records were excluded according to the measured quantity: eight reporting reduced indentation modulus, Er, and four reporting a compression-derived modulus. These quantities were treated separately from Young's modulus, and only records explicitly reporting Young's modulus were included in the present modelling domain. This scope decision concerns the reported measurand and does not assess the validity of the measurement techniques themselves.

Finally, the direct linear associations between the principal alloying contents and Young's modulus are reported in Table 4.3. Pearson's coefficient r describes the direction and strength of each linear association, while r^2 gives the corresponding fraction of variance associated with that element alone. Confidence intervals were obtained by resampling complete publications, and leave-one-publication-out ranges were used to assess the sensitivity of each coefficient to individual sources.

Table 4.3. Association between alloying content and Young's modulus. Intervals are 95% publication-level bootstrap confidence intervals.

Element	r	Variance explained (%)	95% interval (by source)	Range under leave-one-source-out
Fe	+0.445	19.8	+0.22 to +0.59	+0.35 to +0.48
Nb	−0.423	17.9	−0.61 to −0.20	−0.51 to −0.38
Mn	+0.271	7.4	+0.15 to +0.44	+0.17 to +0.29
Zr	−0.246	6.0	−0.42 to −0.07	−0.29 to −0.21
Sn	−0.231	5.3	−0.37 to −0.09	−0.26 to −0.21
Mo	+0.171	2.9	−0.01 to +0.37	+0.14 to +0.21

Higher Nb, Zr, and Sn contents are associated with lower measured modulus in this literature sample, whereas Fe and Mn show positive associations. Iron provides the largest positive coefficient (r = 0.445; 19.8% of the variance) and niobium the largest negative one (r = −0.423; 17.9% of the variance), while molybdenum shows a smaller positive coefficient (r = 0.171; 2.9% of the variance) whose publication-level interval includes zero. Every listed association retains its sign when each publication is removed in turn, so the estimates are robust to the removal of an individual source, even though their magnitudes remain modest.

It should be emphasized that these correlations describe a compositionally selected literature sample, in which elements, processing routes, and phase states vary together. Controlled experiments, or models that contain the relevant structural variables, would be required for any causal interpretation. The physically motivated descriptors calculated from composition are introduced in Section 4.2.

4.2 Physical interpretation of derived features

The derived descriptors were examined before they were used for modelling, so that the part of the feature space actually supported by the collected alloys could be identified. The 240-record modelling domain is described here through the numerical ranges of these descriptors, the population of the composition-based classes, and the degree of overlap among the candidate inputs. All quantities and classifications used in this section are derived from composition alone, and their association with the measured Young's modulus is evaluated separately in Section 4.5.

All 16 continuous descriptors are complete for all 240 records, and the range that each of them occupies in the literature sample is summarized in Table 4.4. Together they provide complementary electronic, β-stability, atomic-size, and rule-of-mixtures descriptions of the alloys, and their numerical ranges define the region of feature space that the collected compositions actually support.

The distribution of ΔL_1 is strongly right-skewed, with a median of 3.05 and a maximum of 31.75. This asymmetry follows directly from the elemental coefficients described in Section 3.3, where the coefficients for manganese and tin are approximately one order of magnitude larger than those for the refractory solutes. As a consequence, the upper tail of ΔL1 can dominate a distance calculation unless the candidate inputs are scaled before distance-based algorithms are applied.

Table 4.4. Composition-derived descriptors in the modelling domain. Values are calculated for 240 records; the ranges describe the literature sample and do not represent universal limits for titanium alloys.

Descriptor family	Descriptor	Unit	Minimum	Median	Maximum
Electronic and phase stability	e/a	–	4.044	4.207	4.475
Electronic and phase stability	Bo	–	2.767	2.823	2.942
Electronic and phase stability	Md	eV	2.245	2.434	2.565
β-stability equivalent	[Mo]eq,B	wt.%	2.50	10.88	31.20
β-stability equivalent	[Mo]eq,Z	wt.%	3.35	13.30	29.83
β-stability equivalent	[Mo]eq,W1	wt.%	3.64	13.00	39.89
β-stability equivalent	[Mo]eq,W2	wt.%	2.99	11.38	25.06
β-stability equivalent	[Mo]eq,Chen	wt.%	2.50	10.81	30.79
Composition average	Weighted molar mass	g mol^{-1}	48.24	64.59	141.02
Composition average	Density	g cm^{-3}	4.655	5.779	13.010
Crystallographic mismatch	ΔL1	%	−0.162	3.051	31.745
Atomic-size description	Δr	pm	−3.143	−0.127	3.046
Rule-of-mixtures property	Specific heat	J kg^{-1} K^{-1}	374.97	466.67	516.68
Rule-of-mixtures property	Bulk modulus	GPa	110.21	121.24	147.74
Rule-of-mixtures property	Shear modulus	GPa	39.72	42.24	52.78
Rule-of-mixtures property	Theoretical Young's modulus, Yth	GPa	100.84	114.23	142.72

The five molybdenum-equivalent variables span different numerical intervals because their empirical coefficients assign different strengths to the individual solutes, although all describe β-phase stabilisation relative to molybdenum. The rule-of-mixtures quantities, in turn, compress the full composition vector into physically interpretable averages of mass, packing, thermal response, and elastic stiffness.

The Bo–Md map shows how the literature sample occupies the electronic regions defined by the published boundaries (Figure 4.4). The largest class is the β + ω/twinning region, with 104 records, followed by the martensitic α′ + α″ region with 59 records, the β-slip region with 55 records, and the α + β region with 22 records. No composition falls in the α-only region.

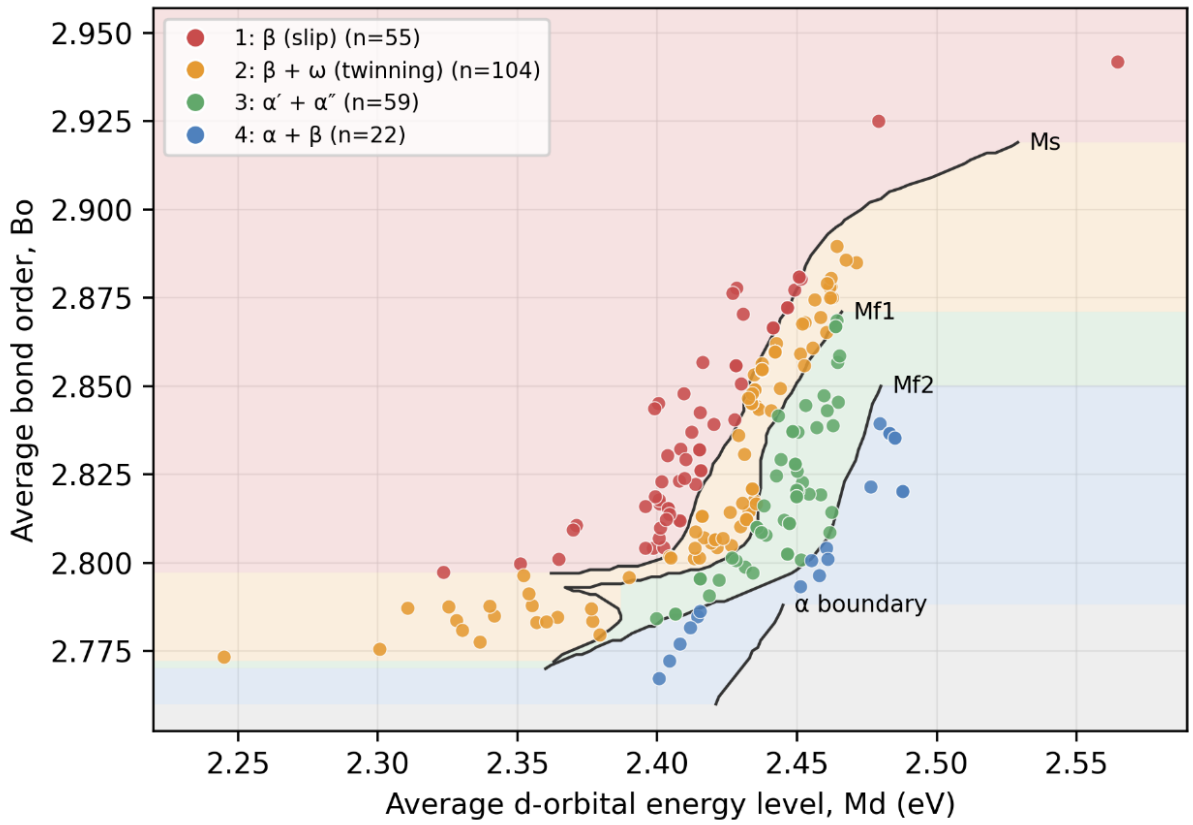

Figure 4.4. Distribution of the 240 modelling records in the Bo–Md diagram. Colours indicate the composition-based regions defined by the published Ms, Mf1, Mf2, and α boundaries; the measured Young's modulus is not used in the classification or the visual encoding.

The phase constitution realised in a given specimen also depends on cooling rate, heat treatment, deformation history, and interstitial content. A point in the β + ω/twinning region therefore only records its position in the electronic map and does not establish that ω precipitates or twins were actually observed in that specimen**.** This distinction matters because many of the source papers report composition and modulus without a complete and consistently coded microstructural characterisation. The e/a–Δr map places 199 records in the twinning region and 41 in the slip region (Figure 4.5). This imbalance shows that the collected literature is concentrated in the composition space associated with twinning. Because alloys with similar e/a can still occupy different regions when their solute-size contributions differ, the joint map retains information that neither coordinate provides on its own. The populations of all composition-based classes considered as candidate categorical features are summarized in Table 4.5.

Table 4.5. Population of the composition-based classes used as candidate categorical features.

Map	Class	Records	Share in modelling domain (%)
Bo–Md	β slip	55	22.9
Bo–Md	β + ω / twinning	104	43.3
Bo–Md	α′ + α″	59	24.6
Bo–Md	α + β	22	9.2
Bo–Md	α	0	0.0
e/a–Δr	Twinning region	199	82.9
e/a–Δr	Slip region	41	17.4

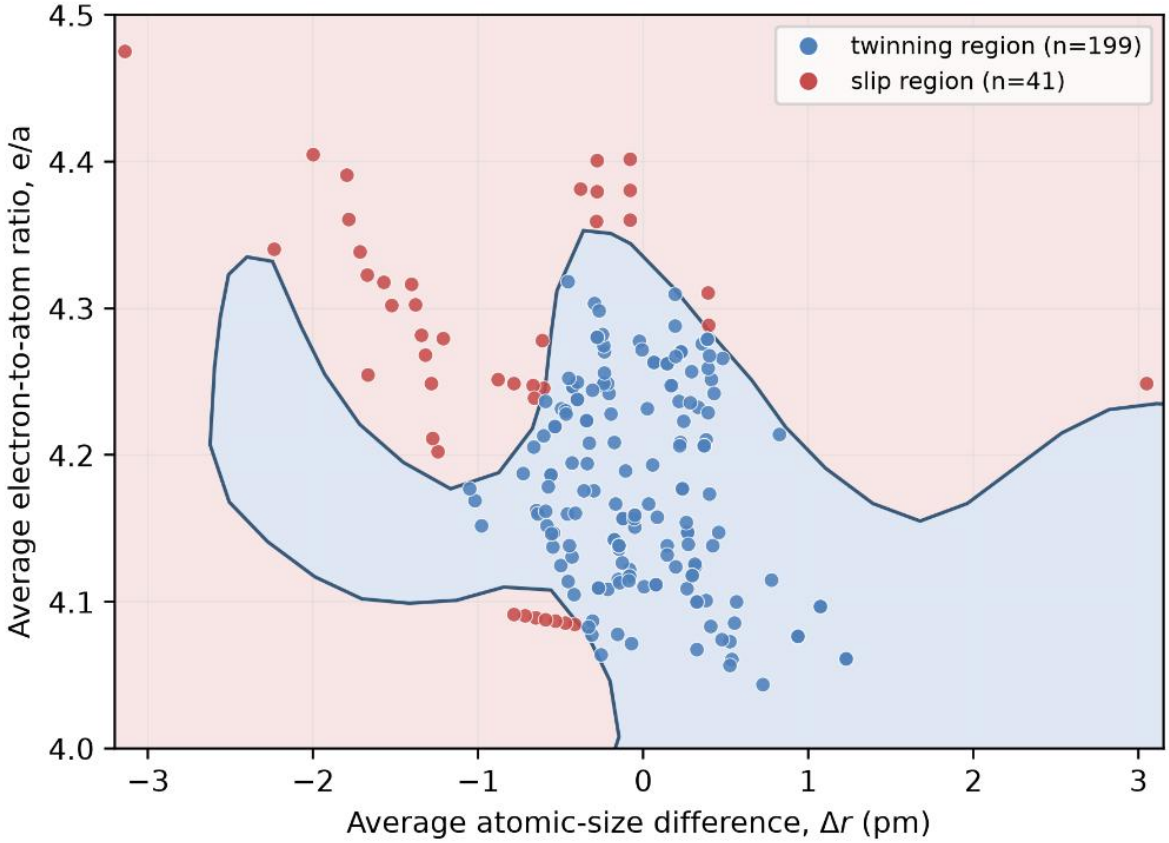

Figure 4.5. Classification of the modelling records in the e/a–Δr diagram. The blue polygon is the composition-based twinning region and the surrounding field is the slip region; the measured deformation mechanisms are not used to assign the labels.

Several descriptors originate from the same elemental composition and are consequently related to one another. Figure 4.6 quantifies this internal structure without reference to Young's modulus. Weighted molar mass and density have a Pearson correlation of 0.97 in this dataset. Md and Δr have a correlation of 0.91. Bo and the rule-of-mixtures bulk modulus have a correlation of 0.90. The five molybdenum-equivalent expressions also contain substantial shared information; the $[Mo]_{eq,B}$ and $[Mo]_{eq,Chen}$ values are almost identical over the sampled compositions (r = 1.00 to the displayed precision); for practical modelling purposes, they encode the same axis of compositional variation. Their shared information must be considered when selecting features and interpreting their individual importance. Specific heat varies inversely with bulk modulus (r = −0.89) and weighted molar mass (r = −0.86).

These correlations have a direct engineering interpretation. Solutes with a high molar mass usually increase the calculated density and reduce the composition-weighted specific heat, while the electronic and atomic-size descriptors respond together to the restricted combinations of elements represented in the literature. A strong correlation means only that two variables carry overlapping information in this particular dataset; it does not make their physical definitions interchangeable. The candidate feature space therefore records the separately defined descriptors together with their mutual dependence, and it is precisely this separation of physical meaning from duplicated numerical information that allows the feature evaluation in Section 4.5 to be interpreted correctly.

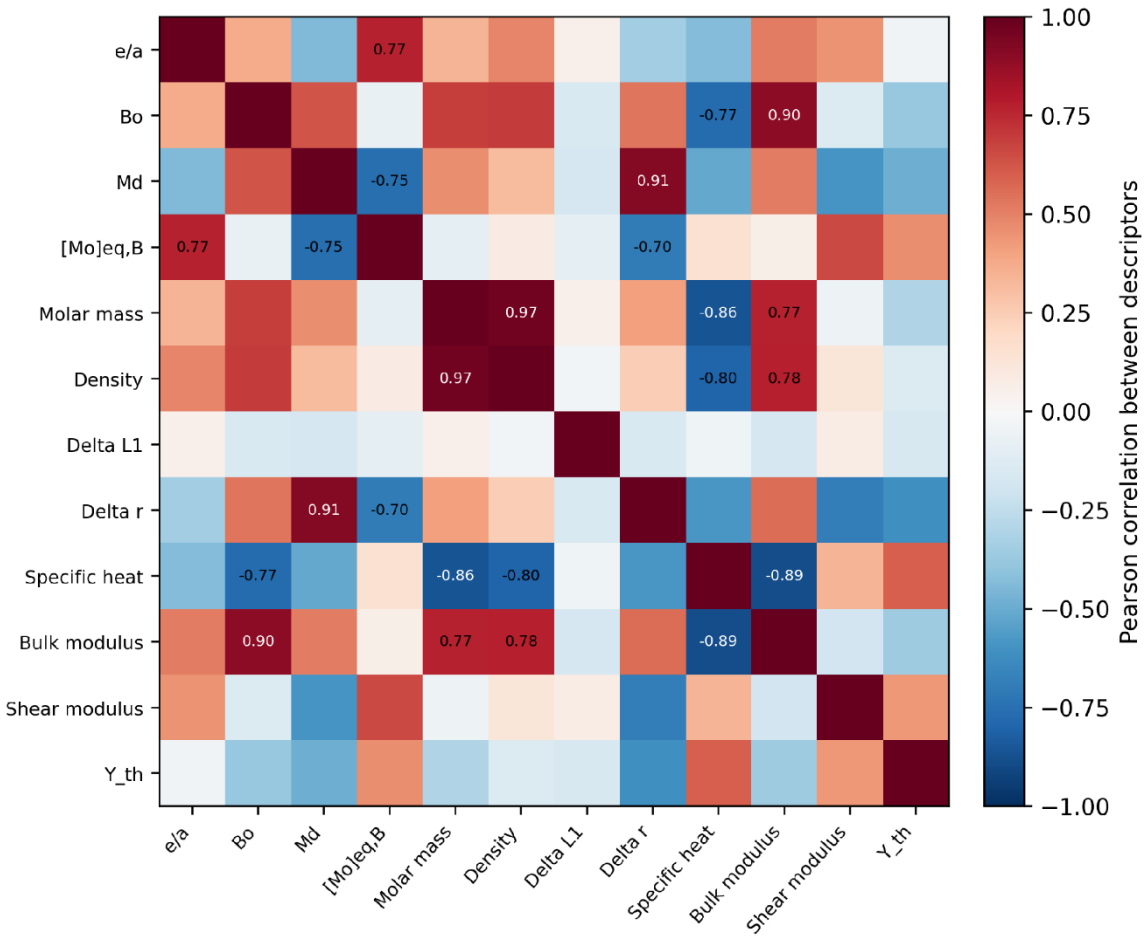

Figure 4.6. Pearson correlations among representative composition-derived descriptors. Numerical labels are shown for absolute correlations of at least 0.70. The matrix describes relationships between the candidate inputs and contains no experimental Young's modulus values.

4.3 Dataset selection and verification

The database was assembled to answer one specific question: how Young's modulus changes with alloy composition in conventionally produced, dense titanium alloys. The complete database contains 280 experimental records, of which 40 describe either a different measured quantity or a production route that falls outside this prediction task. These 40 records remain in the master database, with their original identifiers and references, while the remaining 240 records form the modelling domain.

Twelve of the forty records do not report the same elastic property as the model target. Eight of them report the indentation reduced modulus, Er, and four report a modulus obtained from compression tests on short specimens. Reduced modulus and Young's modulus are different quantities, and a compression-derived stiffness can additionally depend on specimen geometry and machine compliance. Combining such values with Young's modulus would give a single target column more than one physical meaning.

The other 28 records were produced by powder metallurgy, sintering, metal injection moulding, additive manufacturing, or laser cladding. These routes can introduce porosity, incomplete densification, build-direction effects, and route-specific defects, and the database does not contain enough information about these factors to represent them consistently in a composition-based model. The resulting distribution of the forty records is given in Table 4.6.

Table 4.6. Records retained in the master database and placed outside the primary Young's modulus modelling domain. The criteria were applied before model fitting.

Exclusion category	Records	Mean reported modulus (GPa)	Range (GPa)
Reduced modulus Er or compression-derived modulus	12	52.7	23.1–80.0
Powder metallurgy or sintering	13	86.2	56.9–146.0
Metal injection moulding	6	95.3	87.0–103.0
Additive manufacturing, including selective laser melting	7	82.2	70.9–107.1
Laser cladding with powder feed	2	41.0	32.0–50.0
Total	40	—	23.1–146.0

The selection criteria describe the intended use of the model and make no assessment of the quality of the excluded experiments. The reported moduli of the excluded records span 23.1–146.0 GPa, and 37 of the 40 values fall within the 29.0–133.2 GPa range of the modelling data, which confirms that the exclusion does not act on the modulus itself and does not preferentially remove the lowest or highest values. Instead, the exclusions leave a dataset that is consistent in two respects: every record reports the same target property, Young's modulus, and every record comes from a conventional, dense production route that can be described from composition alone.

The 240 retained records were then screened for values that might reflect a transcription error or an unusual physical state. In the first check, each measured modulus was divided by the theoretical modulus estimated from its composition, so that a small ratio marks an alloy that is much softer than a simple rule-of-mixtures estimate would predict. Eight records had a ratio below 0.35, meaning a measured modulus lower than 35% of the composition-weighted expectation. Such a gap is a reason to inspect the source, but not, on its own, a reason to remove the record, because a metastable titanium alloy really can be this compliant. Ti–24Nb–4Zr–7.9Sn is a clear example: its reported modulus is only 33 GPa, yet as a metastable β-titanium alloy its stiffness is governed by phase constitution and processing state, so a low ratio here reflects genuine physics rather than a data error.

The second check compared each record with the five most similar compositions reported in other publications, and 42 records were found to differ from the median of these neighbours by more than three robust standard deviations. In practical terms, their modulus lies well outside the usual spread of nearby compositions: Ti–23Nb–2Fe–10Zr is reported at 104 GPa against a neighbouring median of 49.2 GPa, and Ti–26Nb–2Fe–4Sn at 58 GPa against a neighbouring median of 94 GPa. Differences of this size identify records that deserve source verification, although they can equally reflect phase constitution, deformation, ageing, texture, oxygen content, or measurement conditions that are absent from the composition descriptors.

The repeated compositions show the size of this additional variation directly. The deterministic grouping rule defined in Section 3.2 identifies 19 compositions that were reported in at least two independent publications, together covering 61 records. The median range of Young's modulus within these groups is 2.7 GPa, the upper-quartile range is 12.0 GPa, and five of the 19 groups exceed this value, with the largest range reaching 34.0 GPa. Ti–13Nb–13Zr spans 45–79 GPa across five records from three publications that describe different processing states, including cold-worked and quenched-and-aged material, while Ti–29Nb–13Ta–4.6Zr spans 17.2 GPa across two publications, neither of which reports a processing state at all. The reported state therefore explains only part of the scatter, and unreported processing, measurement conditions, and microstructure account for the remainder.

In total, 46 of the 240 records were flagged by at least one of the two checks and four by both, and each flagged record was examined against its primary publication. Four records were corrected: a composition reported in atomic percent had been entered as weight percent; two records described the same alloy under atomic- and weight-percent names and were merged; and one alloy reported in two processing conditions was restored as two separate records. The remaining flagged records were confirmed as reported and retained, so the modelling domain stands at 240 records.

4.4 Prediction of mechanical properties

Young's modulus varies with several alloying elements at once, and processing and phase state add further variation whose description is incomplete in the available literature. A multivariable model is therefore needed both to combine the composition information and to determine how accurately the property can be estimated for an alloy reported by an independent source.

Six regression algorithms were retained for direct comparison: Ridge regression, support vector regression, Random Forest, Extra Trees, Gradient Boosting, and XGBoost. Four composition-based feature sets were defined before any model was fitted, namely the 12 elemental contents, the 16 derived descriptors, their combination of 28 continuous features, and the full set of 30 features that also includes the two composition-based class labels. A fifth scenario added 21 available processing variables, including heat-treatment temperature and time, deformation, production route, and reported treatment steps. This 51-feature process-aware scenario was evaluated separately, because the process information is incomplete and is in any case unavailable when a new composition is screened before its processing has been chosen.

The main test was designed to represent prediction from a new publication. The 77 publications were divided into five groups, and each group was excluded from model fitting in turn, while a second four-fold validation within the remaining publications was used to select the feature set and the model settings. The excluded publications played no part in these selections. Repeating the procedure produced one out-of-fold prediction for each of the 240 records. A conventional random five-fold split, in which individual rows are assigned to folds regardless of their publication, was also calculated as a secondary result.

Model performance is described by three measures. R^2 is the fraction of the observed variation captured by the predictions, so that a value of zero corresponds to using the mean alone and a negative value is worse than that reference. The mean absolute error (MAE) is the average distance between measured and predicted values, and the root mean squared error (RMSE) gives greater weight to the largest errors. Of the three, MAE has the most direct engineering interpretation, because it is expressed in GPa for Young's modulus and in MPa for strength.

Table 4.7 compares the algorithms on the same 16 derived features, so that the differences arise only from the regression method and its internally selected settings. A prediction that assigns the training mean to every test alloy gives $R^2 = -0.037$ and MAE = 16.34 GPa. Ridge regression already reduces the MAE to 13.20 GPa and gives $R^2 = 0.298$, which shows that a linear combination of the features captures part of the variation, while the nonlinear models reach R^2 values between 0.350 and 0.432. Random Forest gives the best result, with MAE = 11.30 GPa and RMSE = 14.98 GPa, and the reduction in error from 16.34 to 11.30 GPa quantifies the benefit of learning nonlinear relationships between the derived features.

Table 4.7. Publication grouped comparison of models for Young's modulus using the same 16 derived features. Hyperparameters are selected within the training publications of each outer fold.

Model	R^2	MAE (GPa)	RMSE (GPa)
Random Forest	0.432	11.30	14.98
Extra Trees	0.388	11.51	15.55
XGBoost	0.360	12.50	15.91
Gradient Boosting	0.357	12.54	15.93
Support vector regression	0.350	12.63	16.03
Ridge regression	0.298	13.20	16.66

The comparison across fixed feature sets leads to the same practical choice. With Random Forest, the 12 elemental contents give $R^2 = 0.322$ and MAE = 12.25 GPa; the 16 derived descriptors raise R^2 to 0.432 and reduce MAE to 11.30 GPa; combining composition and descriptors gives $R^2 = 0.399$; and adding the two class labels gives $R^2 = 0.404$. The derived descriptors therefore form the strongest compact representation. The fully nested result of $R^2 = 0.417$ is retained as the primary performance estimate, because in that case the choice among the four feature sets was repeated inside each outer training fold.

Adding the process variables increased R^2 for Young's modulus from 0.417 to 0.477 and decreased MAE by 0.40 GPa, from 11.50 to 11.10 GPa. The process variables thus carry useful information, even though the change in the typical prediction error is small. This is consistent with the database statistics: processing affects modulus, but complete and uniformly defined processing data are available for only part of the modelling domain.

Figure 4.7 compares the out-of-fold predictions of the primary composition model with the measured Young's modulus. Of the 240 records, 136 (56.7%) are predicted within 10 GPa and 197 (82.1%) within 20 GPa of the measured value, and the median absolute error is 9.03 GPa. Predictions at the lower and upper ends of the range are drawn towards the centre, which is consistent with microstructural and processing contributions that cannot be reconstructed from composition for every record. Resampling complete publications gives a 95% interval of 0.185–0.576 for R^2 and 9.66–13.64 GPa for MAE, describing how much the estimated performance changes with the particular collection of publications represented in the database. The MAE of 11.50 GPa is close to the 12.0 GPa upper-quartile range found among the repeated-composition groups in Section 4.3, so the model error is on the same scale as the larger differences reported for an unchanged nominal composition across independent publications.

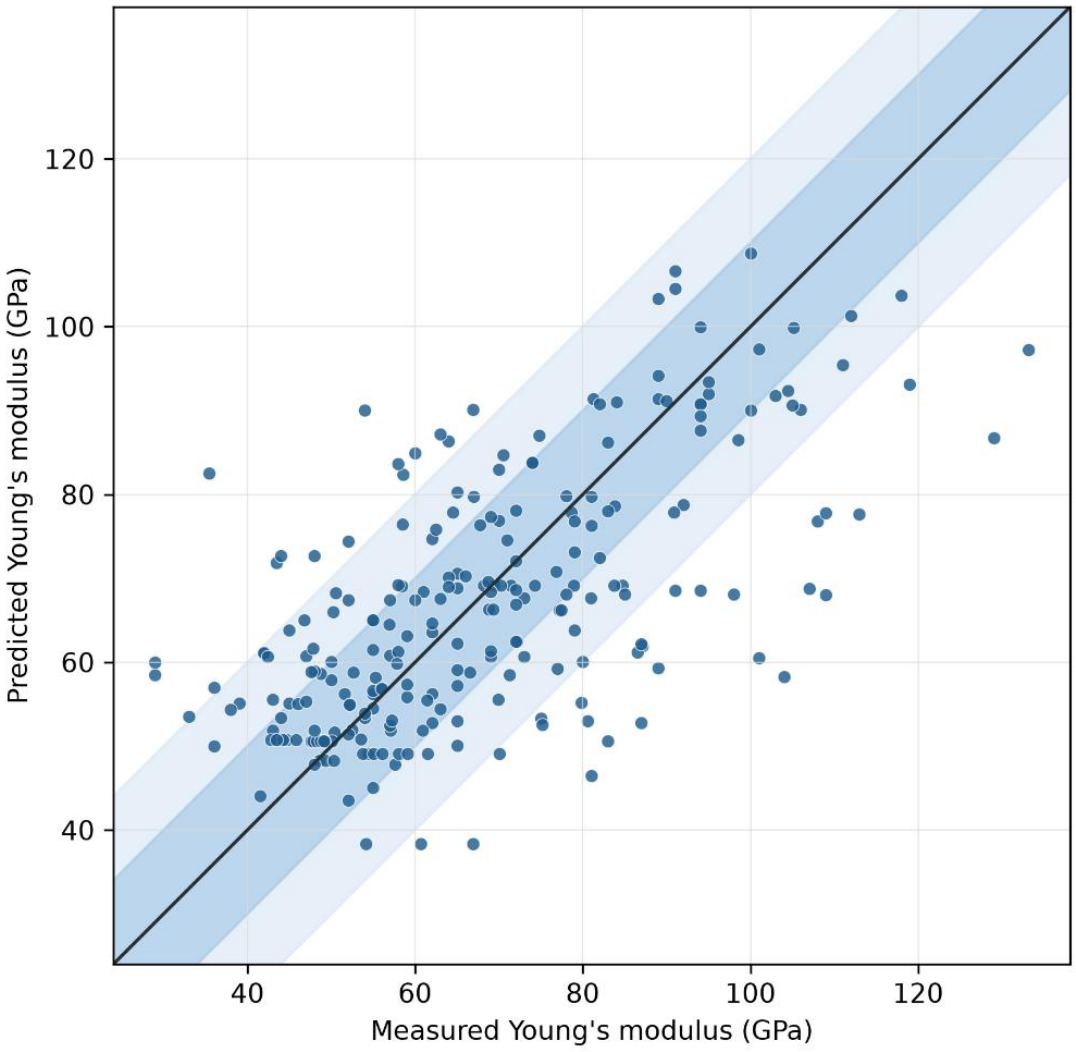

Figure 4.7. Publication grouped out-of-fold prediction of Young's modulus by the nested Random Forest composition model. The diagonal is exact agreement, and the dark and light bands mark deviations of ±10 and ±20 GPa, respectively.

Random row splitting gives higher performance for every property (Table 4.8). For Young's modulus, R^2 rises from 0.417 to 0.597 and MAE falls from 11.50 to 8.93 GPa. Records from the same publication commonly share alloy families, processing routes, measurement conditions, and reporting conventions, and when the rows are divided randomly part of this shared context can appear in both the training and the test data. The publication grouped result is consequently the more relevant measure for application to an independent source.

Yield strength was modelled using 113 records from 34 publications. The composition model gave $R^2 = 0.277$ and MAE = 181.36 MPa under publication grouped validation, with publication resampling giving intervals of 0.001–0.425 for R^2 and 156.57–209.43 MPa for MAE. The result retains a positive predictive signal, although with substantial uncertainty in its magnitude, and the process-aware variant was lower, at $R^2 = 0.205$ and MAE = 188.35 MPa.

Ultimate tensile strength was available for 121 records from 39 publications. Its grouped point estimate of R^2 increased from 0.149 to 0.268 when the process variables were added, and MAE decreased from 213.97 to 193.56 MPa. For the primary composition model, however, publication resampling gave intervals of −0.734–0.533 for R^2 and 159.69–275.45 MPa for MAE. Because the R^2 interval includes zero and extends well into negative values, the apparent improvement cannot establish a transferable process contribution from the available publications.

The publication grouped strength predictions are shown in Figure 4.8. For both properties the predictions occupy a narrower range than the measured values, and this compression is strongest at the upper and lower ends of the experimental range, consistent with the low grouped R^2 values. The model captures a broad strength level from composition but miss part of the variation associated with the thermomechanical and microstructural state.

Table 4.8. Nested model performance by property and evaluation scenario.

Property	Evaluation scenario	Records	Publications	R^2	MAE*	RMSE*
Young's modulus	Publication grouped, composition	240	77	0.417	11.50	15.18
Young's modulus	Publication grouped, process-aware	240	77	0.477	11.10	14.37
Young's modulus	Random rows, composition	240	77	0.597	8.93	12.62
Yield strength	Publication grouped, composition	113	34	0.277	181.36	225.37
Yield strength	Publication grouped, process-aware	113	34	0.205	188.35	236.43
Yield strength	Random rows, composition	113	34	0.525	141.70	182.72
Ultimate tensile strength	Publication grouped, composition	121	39	0.149	213.97	294.21
Ultimate tensile strength	Publication grouped, process-aware	121	39	0.268	193.56	272.76
Ultimate tensile strength	Random rows, composition	121	39	0.749	117.51	159.74

*Errors are in GPa for Young's modulus and in MPa for yield strength and ultimate tensile strength.

The primary model thus provides a useful composition-based estimate of Young's modulus for alloys from unseen publications. The process-aware point estimates change by small or inconsistent amounts across the three targets, and the publication-level intervals for strength remain wide, because the sparse categorical treatment labels cannot yet represent the phase constitution, microstructure, texture, and complete thermomechanical history that ultimately control the measured properties.

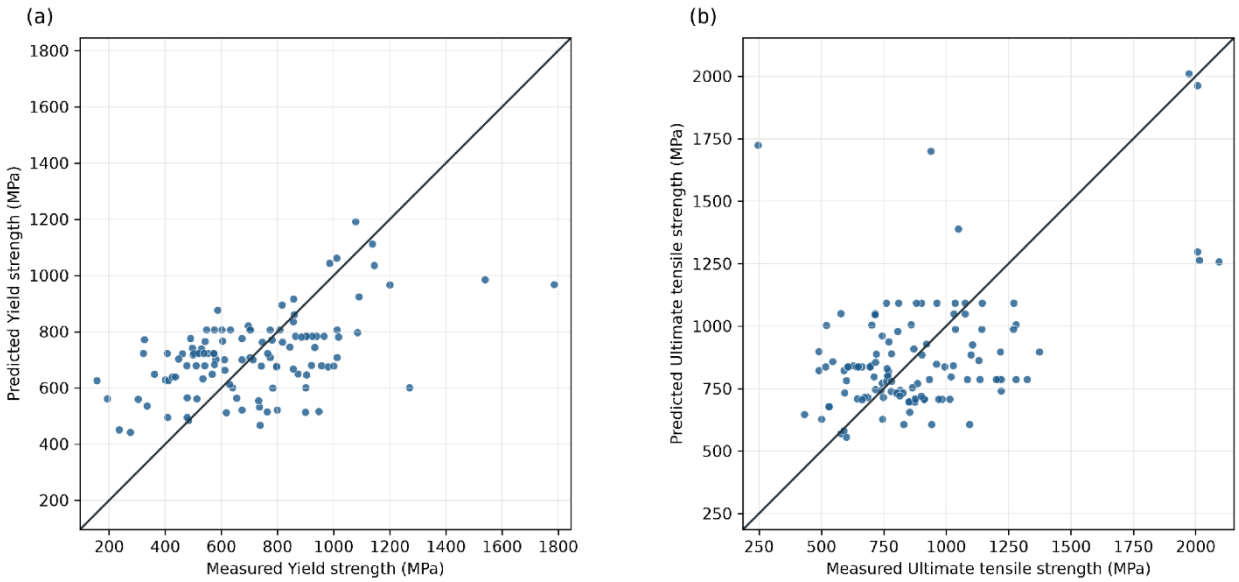

Figure 4.8. Publication grouped out-of-fold strength predictions from the primary composition model: (a) predicted versus measured yield strength; and (b) predicted versus measured ultimate tensile strength. The diagonals indicate exact agreement.

4.5 Feature analysis and model response

The prediction model combines several composition-derived descriptions of the same alloy, and because some of these descriptions carry similar information, the contribution of a descriptor cannot be judged from its correlation with Young's modulus alone. Feature importance was therefore evaluated with a fixed interpretation model that contains all 30 composition-based inputs. The Random Forest hyperparameters were selected within the training publications of each outer fold, and importance was measured only on the excluded publications. This interpretation model gave R^2 = 0.404 and MAE = 11.60 GPa, matching the corresponding 30-input scenario reported in Section 4.4. A fixed set was required because an input can be compared across folds only when it is present in every fold model, whereas the primary model in Section 4.4 selected different input sets within its outer folds.

Permutation importance measures how much the prediction error increases when the values of an input are randomly reassigned, so that a large increase in MAE means the trained model relied on that input when predicting the excluded publications. Each permutation was repeated 100 times within every outer fold. The values in Table 4.9 are the mean increases in MAE, and the ranges give the lowest and highest fold means; a negative lower limit indicates that the apparent contribution was not stable across the five sets of excluded publications.

The electronic descriptors produced the largest mean increase in error, followed by the five molybdenum-equivalent expressions (Figure 4.9). The positive range of 0.19–1.53 GPa for the β-stability group shows that it contributed in every outer fold, whereas the remaining group ranges include zero and are therefore more sensitive to the publications represented in a given test fold. The 12 elemental contents increased MAE by 0.33 GPa when permuted together, but much of their information is also encoded in the derived descriptors, so these grouped values quantify the model's reliance within a redundant representation rather than partitioning the prediction into independent physical causes. Permuting all 30 inputs together increased MAE by 7.87 GPa, from 11.60 to 19.47 GPa; this exceeds the mean-prediction baseline of 16.34 GPa because the permuted model still produces different predictions and assigns them to the wrong alloys. The more useful reference is the 4.74 GPa reduction from the mean baseline to the interpretation model, and the 1.18 GPa importance of the electronic group corresponds to about one quarter of that improvement.

Table 4.9. Grouped permutation importance for the 30-input Random Forest interpretation model. All descriptors in a group were permuted together using the same reassignment of the held-out records. Importance is expressed as the increase in MAE for publications excluded from model fitting.

Input group	Inputs	Mean increase in MAE (GPa)	Range across folds (GPa)
Electronic structure	3	1.18	−0.17 to 2.72
Beta stability	5	0.80	0.19 to 1.53
Elastic and thermal mixture rules	4	0.73	−0.12 to 1.85
Mass and density	2	0.72	−0.37 to 2.12
Elemental composition	12	0.33	−0.51 to 1.00
Atomic size	2	0.15	−0.43 to 1.00
Composition-based classes	2	0.02	−0.01 to 0.09

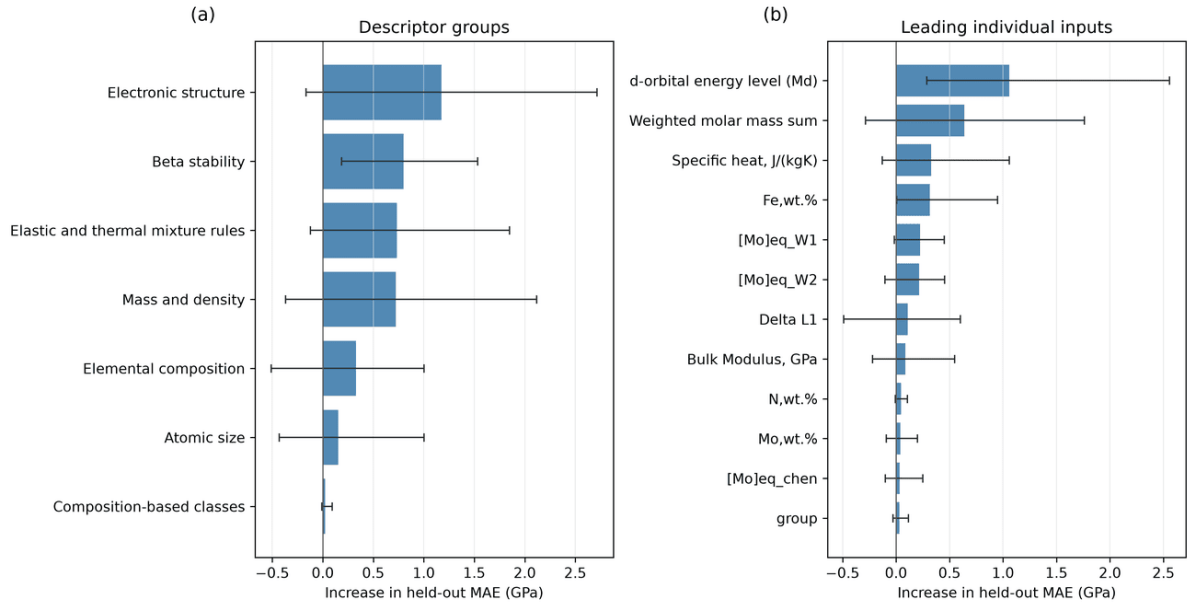

Figure 4.9. Permutation importance of the fixed 30-input Random Forest interpretation model: (a) groups of related inputs and (b) the twelve leading individual inputs. Bars show the mean increase in MAE across the five publication grouped outer folds, and the error bars show the range of the five fold means.

The difference between individual and grouped importance shows the effect of the correlated inputs. Md was the leading individual descriptor: permuting it increased MAE by 1.06 GPa on average, with a positive range of 0.29–2.56 GPa across all five folds. Weighted molar mass came second at 0.64 GPa, although its fold range extended from −0.29 to 1.76 GPa, and specific heat and Fe content increased MAE by 0.33 and 0.31 GPa, respectively. The five individual molybdenum-equivalent variables each increased MAE by no more than 0.23 GPa, whereas their joint permutation increased it by 0.80 GPa, because the model can substitute one highly correlated molybdenum-

equivalent expression for another when only one is disturbed, and permuting the complete group removes that alternative source of the same information.

The form of the model response was determined using accumulated local effects. The populated range of each descriptor was divided into eight intervals, the descriptor was changed only between the local boundaries within each interval, and the resulting prediction changes were accumulated over the range. An ALE value of +5 GPa means that the local model response lies 5 GPa above its average response. These curves describe associations learned by the model and do not establish that changing one descriptor alone would produce the same change in a physical alloy. In Figure 4.10 the shaded regions show the range across the five outer-fold models, and the marks above the horizontal axis show the density of the 240 records. Only the Md response is large relative to the 29.0–133.2 GPa modulus range and the model MAE of 11.60 GPa. Each of the other five ALE curves stays within approximately 1–2 GPa of its average response, so their detailed shapes do not support a comparable physical interpretation.

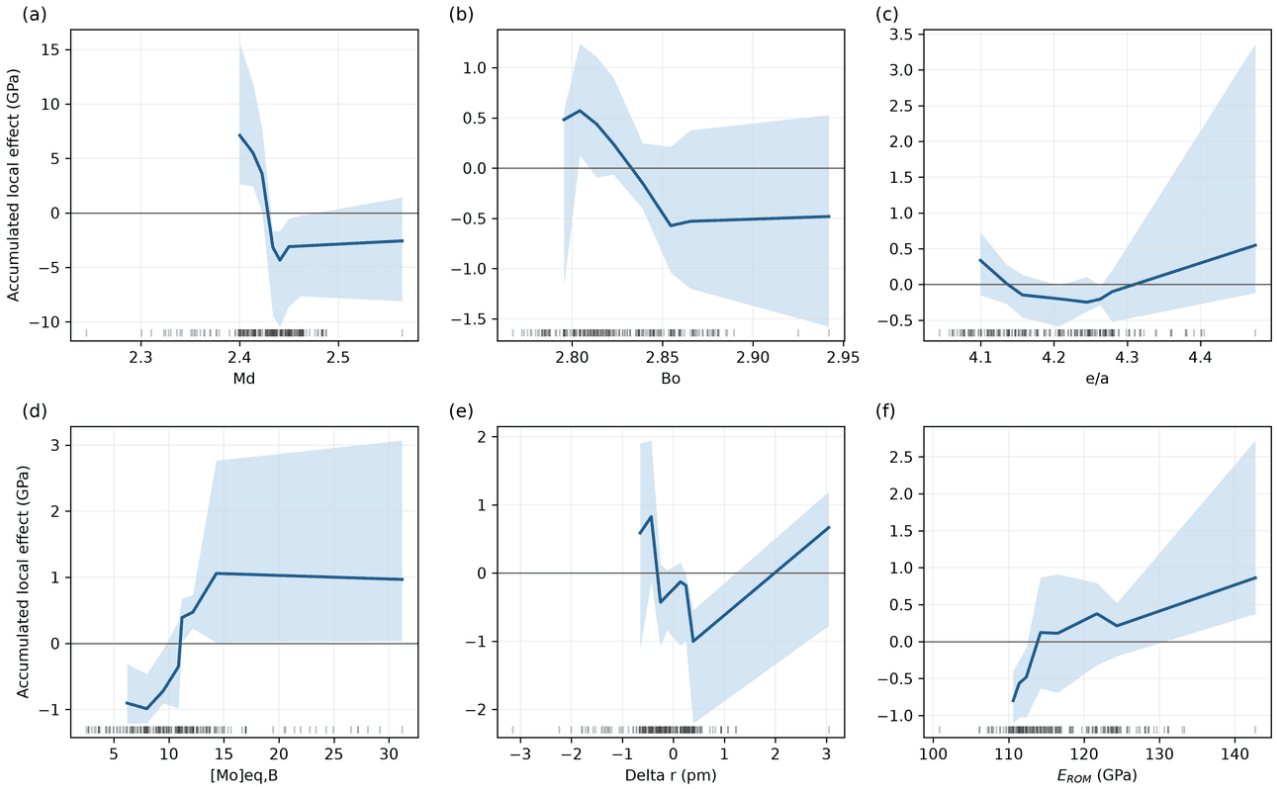

Figure 4.10. Accumulated local effects for six composition-derived descriptors in the fixed 30-input Random Forest interpretation model: (a) Md, (b) Bo, (c) e/a, (d) [Mo]eq,B, (e) Δr, and (f) the composition-weighted theoretical modulus, EROM. Lines show the pooled out-of-fold ALE, the shaded regions show the range across outer folds, and the rug marks show the observed descriptor density.

Md produced the strongest model response. The accumulated effect decreased from +7.11 GPa at Md = 2.400 to −4.35 GPa at Md = 2.441, and then remained almost constant over most of the higher-Md range. The transition interval contains 120 of the 240 records, so the change of 11.5 GPa is supported by half of the modelling domain and is not confined to a few isolated compositions. The individual permutation result confirms that Md remained useful in every outer fold, although the width of the ALE band shows that the magnitude of the response is uncertain. The learned decrease is consistent with the role of the d-electron energy in the electronic description of metastable β-titanium alloys developed in Chapter 2, but this agreement concerns only the direction learned from the collected compositions, since the literature data do not vary Md independently of alloy system, processing, and phase state.

The other five descriptors produced smaller accumulated effects. [Mo]eq,B increased by about 2 GPa between its lower and upper ranges, EROM by about 1.7 GPa across its observed range, and Bo by approximately 1 GPa, while the e/a and Δr curves were non-monotonic and stayed within about ±1 GPa of the average response. Because their fold ranges frequently crossed zero, the detailed turns in these curves are not stable enough to interpret physically.

The two classical composition-based classifications carried little direct predictive information for Young's modulus. The Bo–Md regions accounted for 3.9% of the observed modulus variation (η^2 = 0.0389; bias-corrected ω^2 = 0.0266), with a publication-resampled interval of 0.008–0.149 and a row-level permutation value of p = 0.0236, and the e/a–Δr classification accounted for 14.7% (η^2 = 0.1472; ω^2 = 0.1431), with an interval of 0.022–0.308 and p < 0.001. When both class labels were permuted in the prediction model, MAE increased by only 0.02 GPa. These diagrams encode phase stability and deformation mechanism, and their broad regions retain less information about stiffness than the continuous electronic and β-stability descriptors.

The second-order ALE analysis did not resolve a substantial Mo–Sn interaction. Across the supported cells, the interaction term ranged from −0.009 to +0.012 GPa, which is negligible relative to the 11.60 GPa model MAE. Both elements were present in 39 records from 12 publications, and six of the nine Mo–Sn cells contained at least three records from at least two publications, while the remaining three cells were left blank in Figure 4.11. The result shows that the model treats the resolved Mo and Sn contributions as effectively additive within the populated region; it does not establish that a physical Mo–Sn interaction is absent, because the joint composition space is sparse and the local perturbations do not enforce exact composition closure.

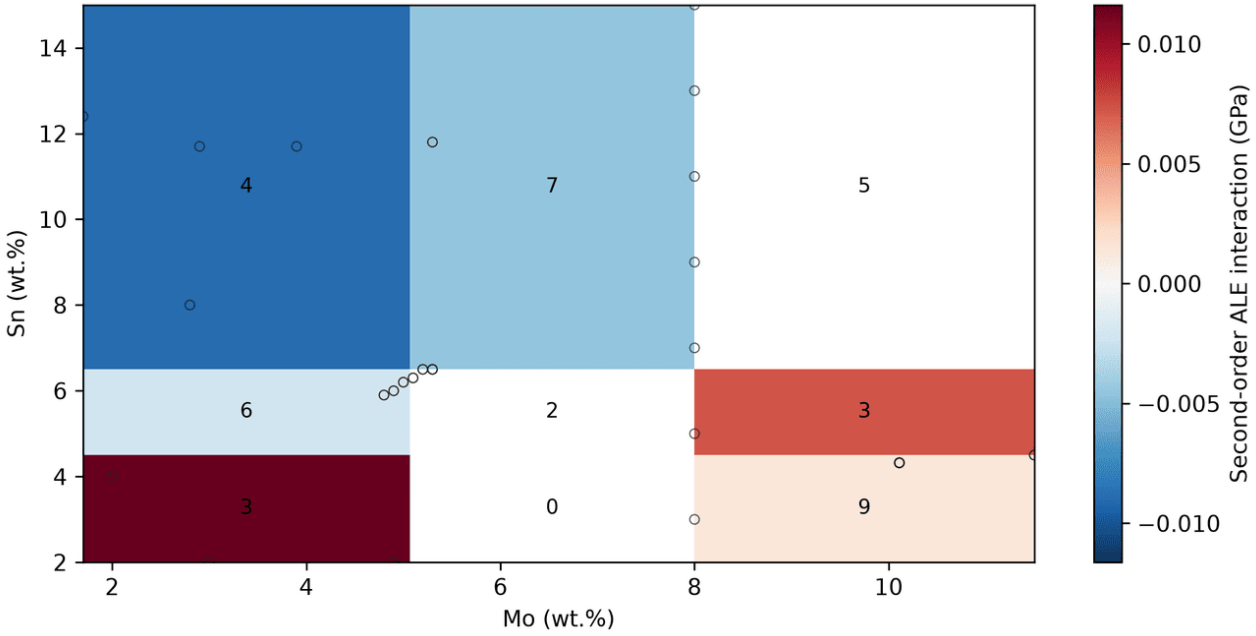

Figure 4.11. Second-order accumulated local interaction between Mo and Sn for the fixed 30-input Random Forest interpretation model. The numbers give the records in each cell, the circles show the 39 compositions containing both elements, and the blank cells fail the requirement of at least three records from at least two publications.

Two compact feature refinements were evaluated under the same publication grouped validation before the model was applied to new compositions, using the 16-derived-descriptor screening baseline (R^2 = 0.430, MAE = 11.40 GPa, RMSE = 15.011 GPa), which differs from the 30-input interpretation model with MAE = 11.60 GPa used for the permutation analysis. Before fitting, retention was defined by a pooled MAE reduction of at least 0.25 GPa together with a lower MAE in at least four of the five outer folds. Retaining a single molybdenum-equivalent expression reduced the input set from 16 to 12 descriptors and gave R^2 = 0.433, MAE = 11.44 GPa, and RMSE = 14.968

GPa; it improved R^2 by 0.003 and RMSE by 0.043 GPa, but its MAE was 0.042 GPa higher and lower in only one of the five folds, so the pre-specified rule rejected it. Adding Oeq and the interstitial-reporting indicator gave $R^2 = 0.426$, MAE = 11.53 GPa, and RMSE = 15.053 GPa, with an MAE that was 0.129 GPa higher and lower in two folds. Since neither representation met the predefined criterion, the screening model retained the 16 derived descriptors, and the tests provided no evidence that descriptor redundancy or the proposed interstitial encoding accounts for the remaining prediction error.

Overall, the model relies most consistently on Md and on the groups of correlated electronic and β-stability descriptors, yet their importance remains modest relative to the interpretation-model MAE of 11.60 GPa. Variations in processing, phase constitution, texture, measurement, and sparsely sampled alloy systems therefore remain part of the prediction error.

4.6 Prediction of new alloy compositions

The composition model was then used to identify Ti–Mo–Sn alloys with a low predicted Young's modulus and to determine how strongly the literature database supports each prediction. The systematic grid contained 6,561 compositions between 0 and 16 wt.% Mo and 0 and 16 wt.% Sn, of which 4,590 (70.0%) lie within the applicability domain defined by the distance to the measured alloys.

Candidate support was measured in a scaled space of eight non-redundant descriptors, by comparing the mean distance to the five nearest database records with the corresponding distances among the training records themselves. The applicability threshold was set at 1.407, equal to the 95th percentile of the training-record distribution, so that a candidate below 1.407 falls within the distance range occupied by 95% of the modelling records.

The predicted surface contains a low-modulus region centred at approximately 7–9 wt.% Mo and 13–16 wt.% Sn (Figure 4.12). The lowest well-supported grid prediction is 50.7 GPa for Ti–8Mo–14.8Sn, and the neighbouring candidates remain below 55 GPa once a minimum spacing of 1 wt.% is imposed between ranked compositions (Table 4.10). The white boundary in Figure 4.12 encloses the central region that satisfies the distance criterion, while grey hatching marks the candidates outside this domain. The compositions selected for synthesis are marked by red diamonds. The measured alloys that contain both Mo and Sn (white circles in Figure 4.12) are concentrated around Ti–8Mo–xSn and several multicomponent systems near 5 wt.% Mo and 6 wt.% Sn, so the apparent continuity of the predicted surface exceeds the density of the direct experimental coverage.

Table 4.10. Lowest predicted Ti–Mo–Sn candidates within the applicability domain.

Candidate	Predicted E (GPa)	Five-neighbour distance	SD across fold models (GPa)
Ti–8Mo–14.8Sn	50.7	0.87	6.30
Ti–7.2Mo–15.8Sn	52.1	1.01	5.77
Ti–8Mo–13.8Sn	52.3	0.74	6.20
Ti–7Mo–14.8Sn	52.8	0.86	5.74
Ti–8.2Mo–12.8Sn	53.8	0.66	5.45
Ti–7Mo–13.8Sn	54.2	0.75	5.22

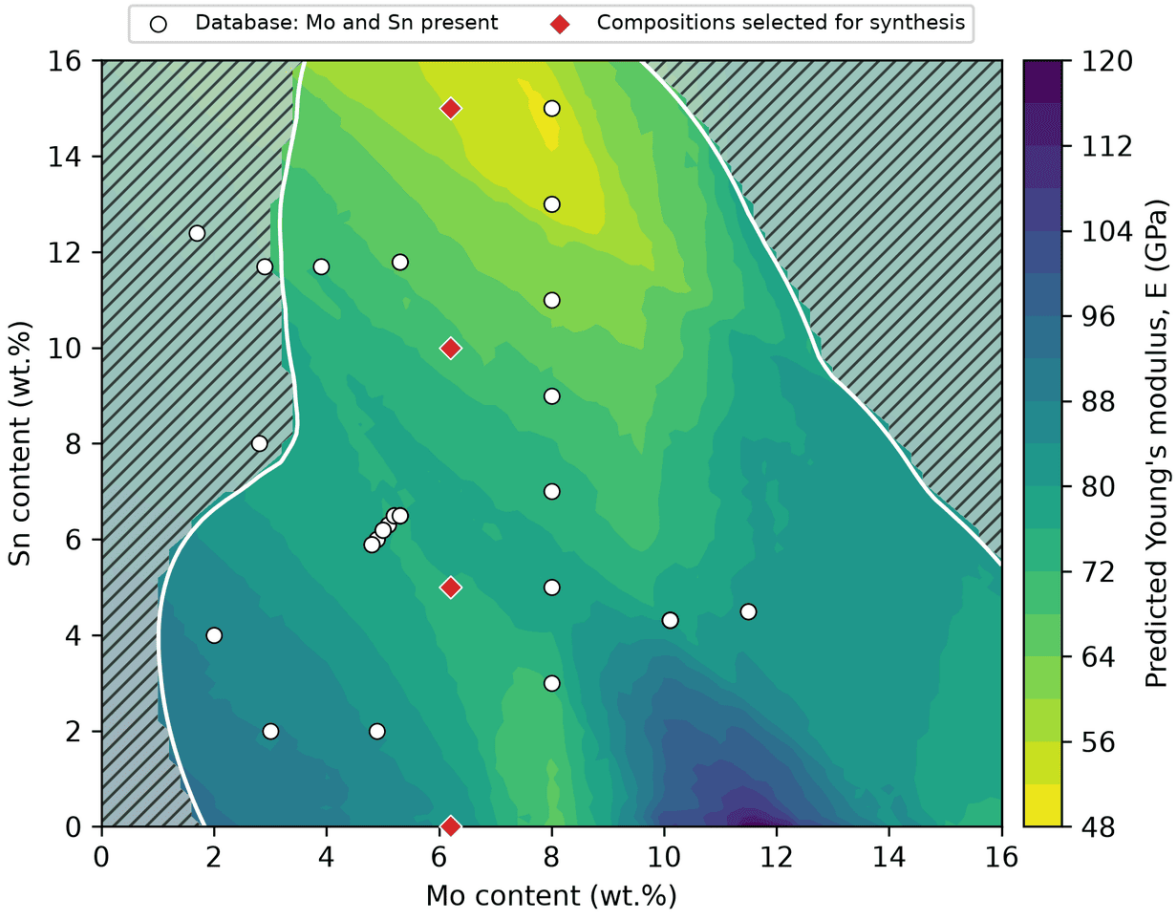

Figure 4.12. Predicted Young's modulus in the Ti–Mo–Sn composition space, with the applicability-domain boundary shown as a white line. Lighter colours correspond to a lower predicted modulus.

The prediction error remains large relative to the differences among the neighbouring candidates. In publication grouped validation, 80% of the absolute errors were below 18.49 GPa, 90% below 24.99 GPa, and 95% below 29.97 GPa; these limits describe the empirical coverage across the database and do not provide a composition-specific confidence interval. The standard deviation across the five fold models has a median of 4.35 GPa and a 95th percentile of 7.63 GPa over the complete grid, and this smaller model-to-model spread shows that agreement among the Random Forest fits captures only one part of the prediction uncertainty.

The distance plot separates candidate support from the predicted value (Figure 4.13). Low-modulus predictions occur both well within the domain and close to its boundary, so a low prediction is not automatically the product of extrapolation. Predictions beyond the distance threshold cluster over a narrower modulus range, because tree models tend towards the values represented in their training leaves as a candidate moves away from the populated regions. Ranking the minimum of a noisy prediction surface introduces an additional downward bias. In each of the five publication grouped folds, the record with the lowest predicted modulus was selected before its measurement was examined, and the measured value then exceeded the selected prediction by an average of 7.30 GPa and a median of 7.51 GPa, with the five differences ranging from −2.55 to 16.33 GPa. The numerical minimum of 50.7 GPa should therefore be read as a screening rank with an observed tendency towards underestimation, its precision limited both by this selection effect and by the publication grouped prediction error. Adding the mean selection bias to the minimum gives a simple bias-adjusted estimate of about 58.0 GPa, which describes the average behaviour of the five pseudo-screening tests and remains less specific than a new measurement of the candidate.

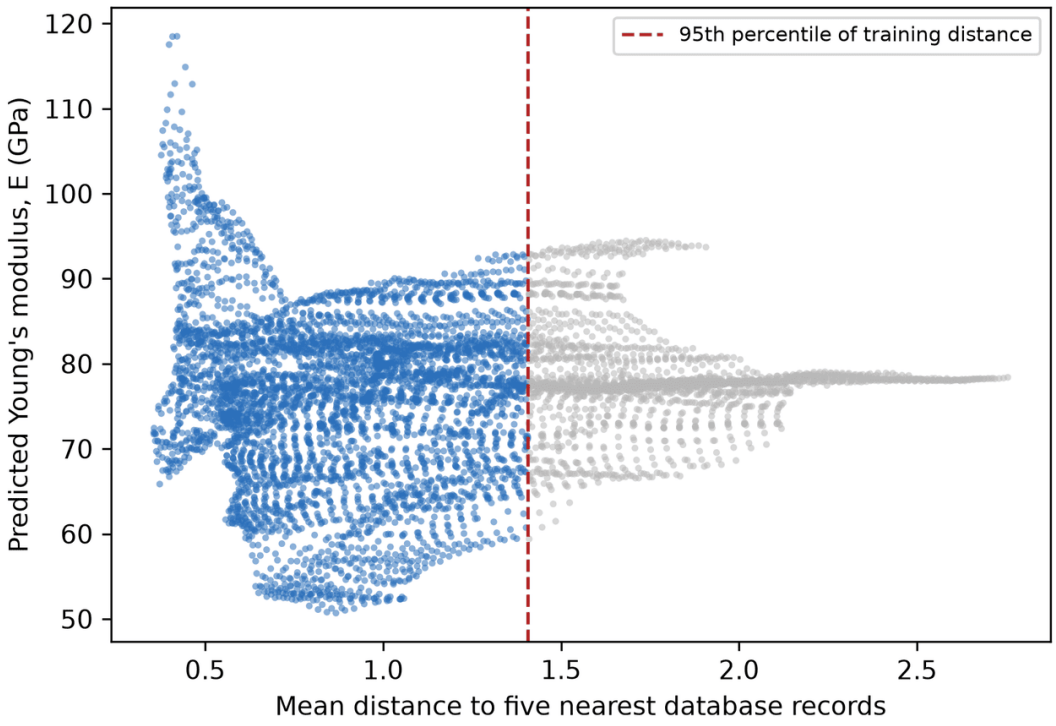

Figure 4.13. Predicted Young's modulus of the 6,561 Ti–Mo–Sn candidates as a function of the mean distance to their five nearest database records. Blue points satisfy the applicability criterion, grey points lie outside it, and the dashed line is the 95th percentile of the training-record distance.

The low-modulus region also depends strongly on the Ti–8Mo–xSn measurements of Li et al. (2023). The final model fitted to all publications follows the measured decrease above approximately 7 wt.% Sn because these eight records are part of its training data, and removing the complete publication raises the prediction error for the series to 16.77 GPa and gives $R^2 = -2.408$. At the measured compositions, the source-excluded model predicts 84.5–95.1 GPa at 0–5 wt.% Sn and 68.4–69.1 GPa at 13–15 wt.% Sn, missing both the low value of binary Ti–8Mo and the measured minimum at high Sn content (Figure 4.14). The surface is therefore a quantitative summary of the available Ti–Mo–Sn evidence, and its ability to reproduce the Sn trend does not transfer when the publication that defines that trend is withheld. For the best-ranked Ti–8Mo–14.8Sn candidate, excluding Li et al. (2023) raises the prediction from 50.7 to 68.6 GPa, a difference of 17.9 GPa, so the ranking of this candidate depends directly on the experimental series located in the same composition region.

The Ti–6.2Mo base alloy and the three Sn additions selected for synthesis all lie within the applicability domain (Table 4.11). The model predicts a decrease from 83.3 GPa for Ti–6.2Mo to 55.4 GPa for Ti–6.2Mo–15Sn. The fold-model standard deviation spans 1.33–5.03 GPa across the series, following the sequence 2.35, 5.03, 1.33, and 4.98 GPa as Sn increases; this non-monotonic variation reflects a sensitivity to which publications are used for fitting and does not represent the expected prediction error, which is given instead by the publication grouped residual quantiles.

The composition model averages over the processing states represented in the database. The experimental Ti–6.2Mo–xSn alloys were homogenised at 1000 °C for 2 h, water quenched, and cold rolled to a thickness reduction of approximately 20%, and the predictions in Table 4.11 are not conditioned on this specific thermomechanical state. The four compositions provide a controlled experimental sequence extending from the base alloy towards the predicted low-modulus region, allowing the predicted trend with increasing Sn content to be evaluated experimentally.

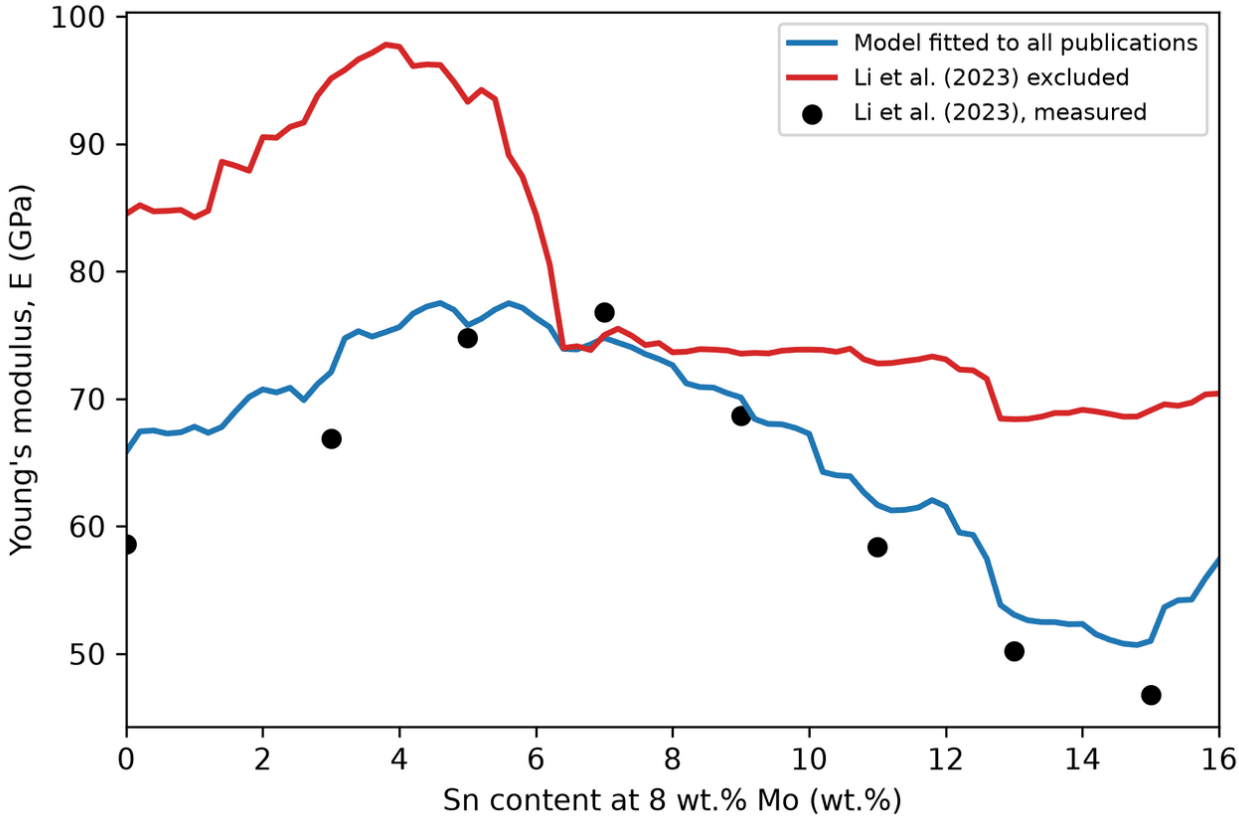

Figure 4.14. Young's modulus along the Ti–8Mo–xSn series. The blue curve is predicted by the final model fitted to all 77 publications, the black circles are the eight measurements reported by Li et al. (2023), and the red curve shows the predictions after that publication was removed before model fitting.

Table 4.11. Model predictions for the Ti–6.2Mo–xSn compositions selected for experimental validation. All four candidates satisfy the applicability-domain distance threshold of 1.407.

Candidate	Predicted E (GPa)	Five-neighbour distance	SD across fold models (GPa)
Ti–6.2Mo	83.3	0.50	2.35
Ti–6.2Mo–5Sn	75.4	0.75	5.03
Ti–6.2Mo–10Sn	69.5	0.80	1.33
Ti–6.2Mo–15Sn	55.4	0.94	4.98

4.7 Experimental validation of designed alloys

4.7.1 Chemical composition and density

Table 4.12 presents the experimentally and theoretically estimated values of the density, open porosity and relative density of the Ti–6.2Mo and Ti–6.2Mo–xSn alloys. The density of the Ti–6.2Mo alloy was 4.68 g/cm3, while the density of the Ti–6.2Mo–15Sn alloy was about 4.97 g/cm3. The increase in density with increasing Sn content is consistent with the higher density of Sn relative to Ti.

The experimental density values of all investigated alloys were close to the corresponding theoretical values, while the open porosity remained below 1%. Together with relative density values close to 100%, these results indicate a high degree of densification and low open porosity in the synthesized alloys.

Table 4.12. Density and porosity parameters of the synthesized Ti–6.2Mo and Ti–6.2Mo–xSn alloys determined by the Archimedes method.

Alloy	Experimental density (g/cm³)	Theoretical density (g/cm³)	Relative density (%)	Open porosity (%)
Ti–6.2Mo	4.677	4.668	100.18	0.04
Ti–6.2Mo–5Sn	4.761	4.762	99.97	0.06
Ti–6.2Mo–10Sn	4.820	4.860	99.18	0.12
Ti–6.2Mo–15Sn	4.973	4.962	100.22	0.05

For some alloys, small differences were observed between the theoretical and experimental density values, resulting in relative density values slightly above 100%. The theoretical densities were calculated using the experimentally determined alloy compositions obtained by EDS analysis, and the remaining small differences may reflect local compositional variations as well as experimental uncertainty associated with the Archimedes method. Considering the small absolute differences between the measured and calculated values, these deviations do not indicate substantial differences between the theoretical and experimental densities.

The results therefore show that increasing Sn content did not produce a measurable increase in open porosity, with all investigated alloys exhibiting open porosity below 1%.

The chemical composition of the synthesized Ti–6.2Mo and Ti–6.2Mo–xSn alloys was evaluated by EDS analysis to assess the actual elemental content after processing. The nominal and measured alloy compositions are summarized in Table 4.13. Generally, the EDS-estimated compositions were close to the nominal values, indicating that the targeted alloy compositions were approximately achieved. A gradual increase in Sn content was observed with increasing nominal Sn addition, while the Mo content remained close to the targeted value in all investigated alloys.

Table 4.13. Nominal and EDS-estimated chemical compositions of the synthesized Ti–6.2Mo and Ti–6.2Mo–xSn alloys.

Alloy	Nominal composition (wt.%)	Measured composition by EDS (wt.%)
Ti–6.2Mo	Ti–6.2Mo	94.3Ti–5.7Mo
Ti–6.2Mo–5Sn	Ti–6.2Mo–5Sn	88.4Ti–5.8Mo–5.9Sn
Ti–6.2Mo–10Sn	Ti–6.2Mo–10Sn	82.3Ti–6.4Mo–11.2Sn
Ti–6.2Mo–15Sn	Ti–6.2Mo–15Sn	77.7Ti–6.1Mo–16.3Sn

Several alloys exhibited small deviations between the nominal and measured compositions. Such differences may reflect elemental redistribution during melting and solidification, local

compositional variations within the analysed regions, and uncertainty associated with EDS quantification.

Figure 4.15 shows representative EDS elemental maps of the Ti–6.2Mo–15Sn alloy. Within the analysed region, Ti, Mo, and Sn show a relatively uniform spatial distribution, with no clearly visible elemental segregation.

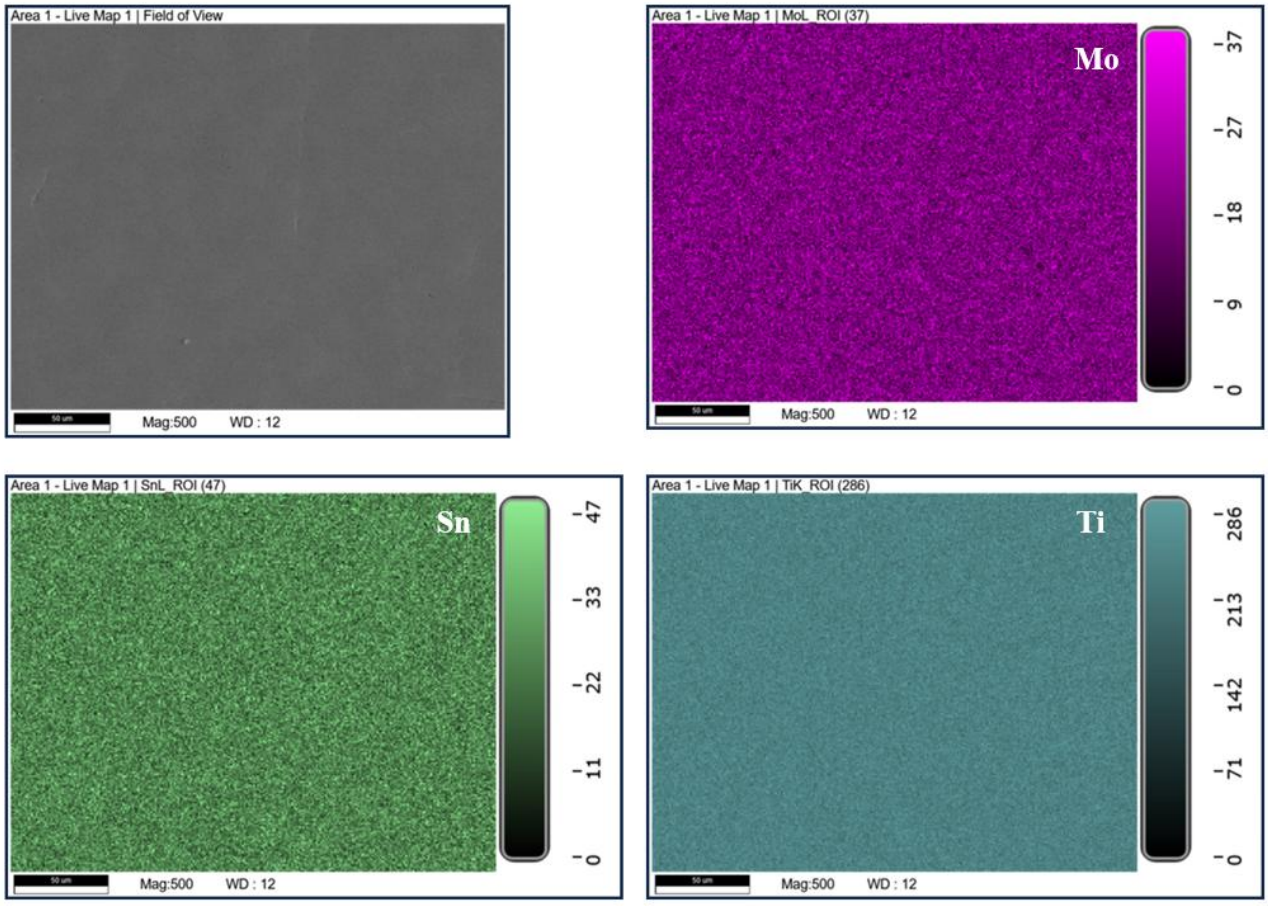

Figure 4.15. Representative SEM image and corresponding EDS elemental maps of the Ti–6.2Mo–15Sn alloy showing the distribution of Ti, Mo, and Sn within the analyzed region.

4.7.2 Phase analysis by XRD

X-ray diffraction (XRD) patterns of the initial Ti, Mo, and Sn powders are presented in Figures 4.16(a–c). The diffraction peaks of Ti powder were indexed to the α-Ti phase with a hexagonal close-packed (HCP) crystal structure ($P6_3/mmc$), while those of Mo powder were indexed to a body-centered cubic (bcc) structure (Im-3m). The Sn powder was identified as tetragonal β-Sn ($I4_1/amd$). The obtained lattice parameters are summarized in Table 4.14 and were used as reference values for the subsequent analysis of structural changes after alloy synthesis. No additional crystalline phases were detected within the detection limits of the XRD analysis.

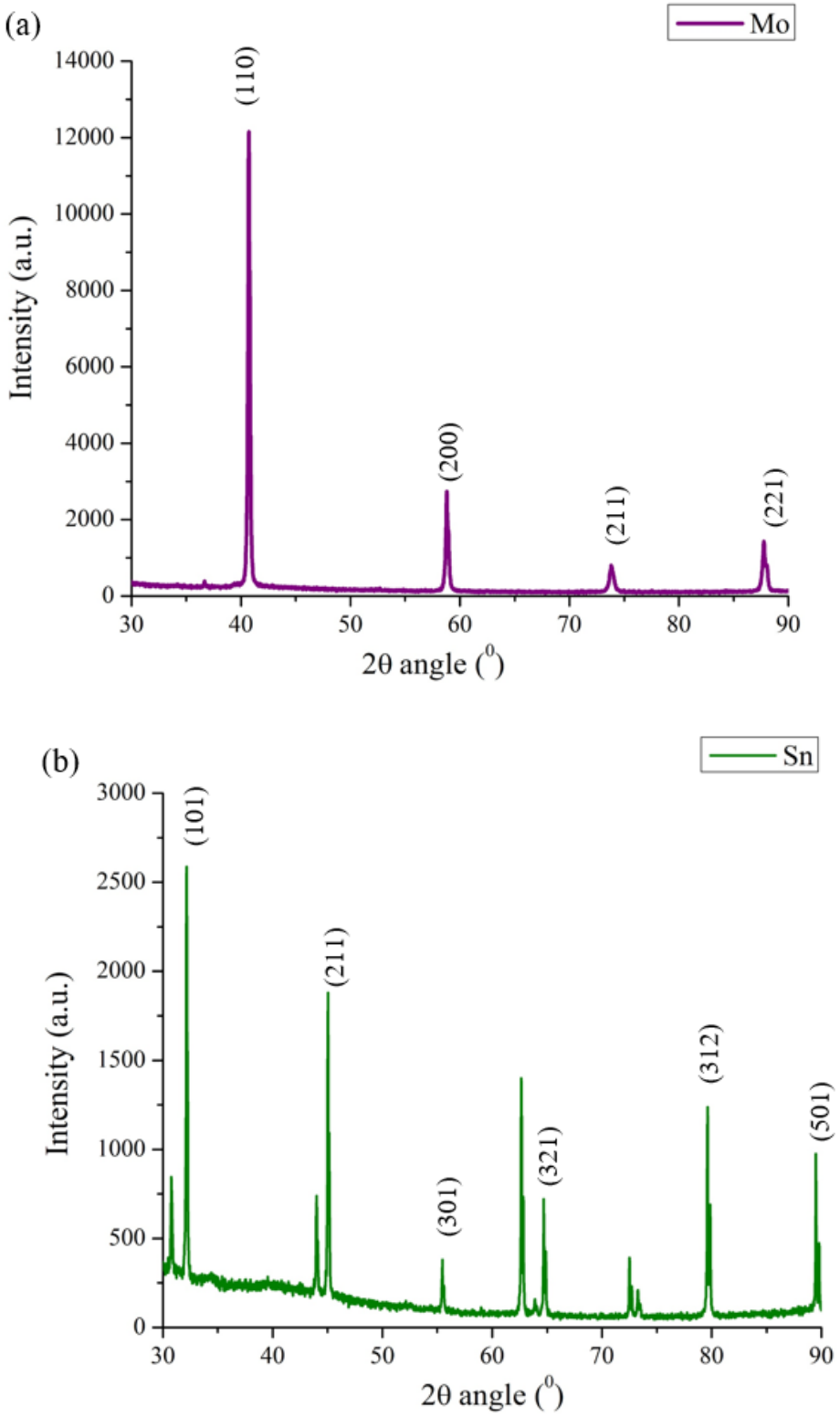
(a)
Mo
(110)
(200)
(211)
(221)
Intensity (a.u.)
2θ angle (0)
(b)
Sn
(101)
(211)
(301)
(321)
(312)
(501)
Intensity (a.u.)
2θ angle (0)

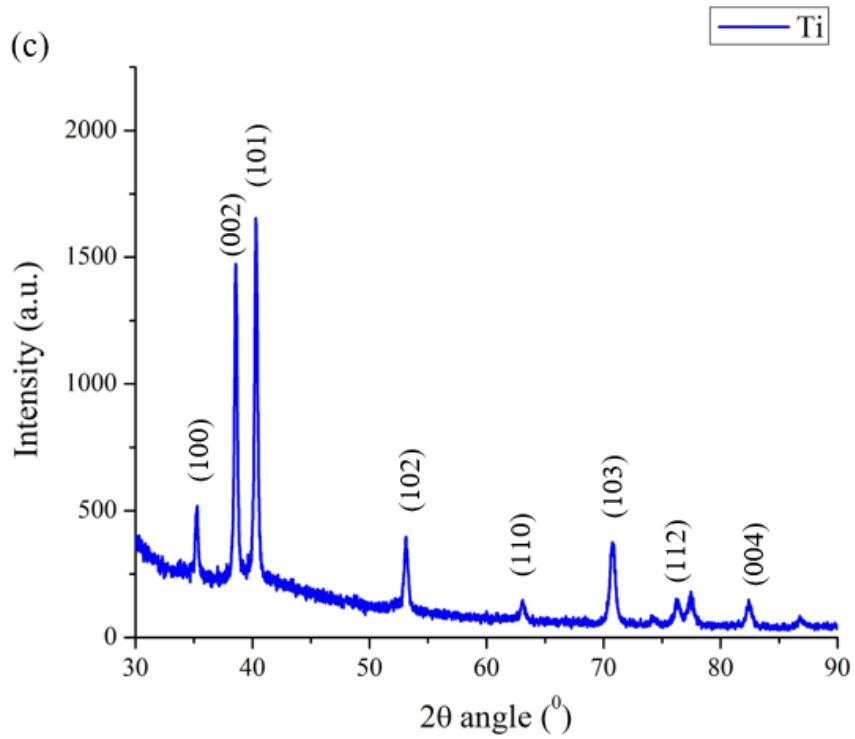

Figure 4.16. XRD patterns of the starting elemental powders: (a) β-Mo powder with a bcc crystal structure; (b) β-Sn powder with a tetragonal crystal structure; and (c) α-Ti powder with an HCP crystal structure.

Table 4.14. Crystal structure parameters of the initial elemental powders used for alloy synthesis.

Powder	Phase / Structure	Space group	Lattice parameters
Ti	α-Ti (HCP)	P63/mmc	a = 2.948 Å, c = 4.677 Å
Mo	β-Mo (bcc)	Im-3m	a = 3.140 Å
Sn	β-Sn (tetragonal)	I41/amd	a = 5.825 Å, c = 3.176 Å

The identified crystal structures and lattice parameters of the initial powders provide a reference for the subsequent analysis of phase evolution in the synthesized alloys.

The XRD patterns of the TiMo, TiMo5Sn, TiMo10Sn, and TiMo15Sn alloys are shown in Figures 4.17(a–d). The evolution of the lattice parameters and crystallite size with increasing Sn content is summarized in Figures 4.18 and 4.19, respectively. The diffraction analysis revealed that all investigated alloys were predominantly composed of α-Ti-based phase with a hexagonal close-packed (HCP) crystal structure. The identified reflections were indexed according to the $P6_3/mmc$ space group corresponding to α-Ti. No clearly distinguishable β-Ti reflections were detected in the investigated alloys, indicating that α-Ti was the predominant crystalline phase under the applied processing conditions.

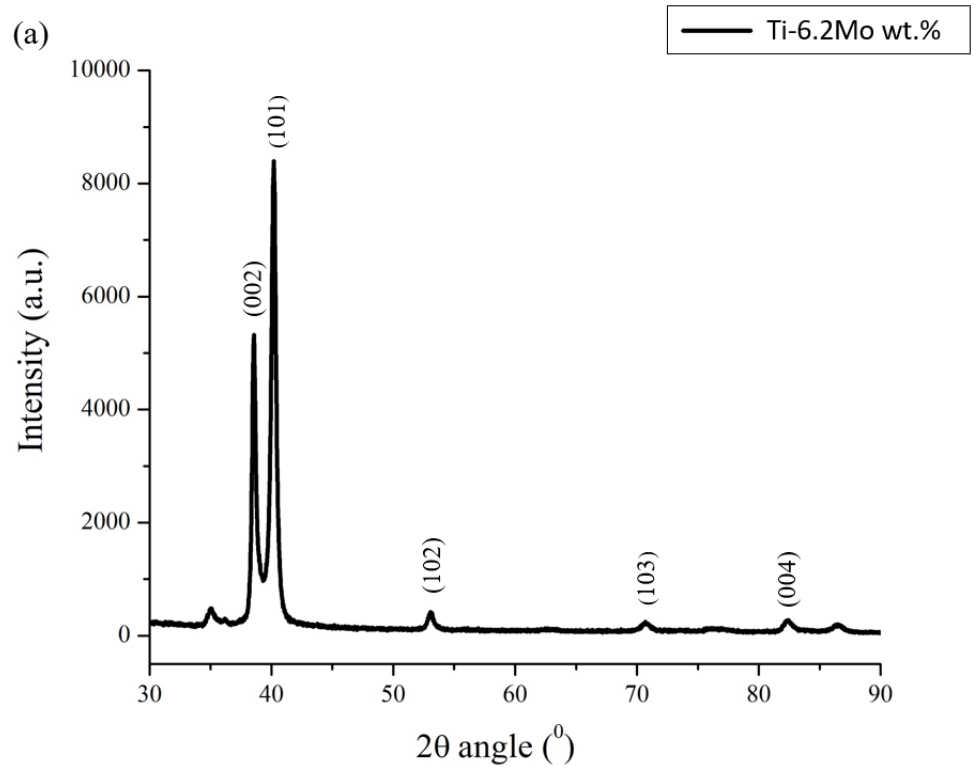
(a)
Ti-6.2Mo wt.%
Intensity (a.u.)
10000
8000
6000
4000
2000
0
(002)
(101)
(102)
(103)
(004)
30
40
50
60
70
80
90
2θ angle (0)

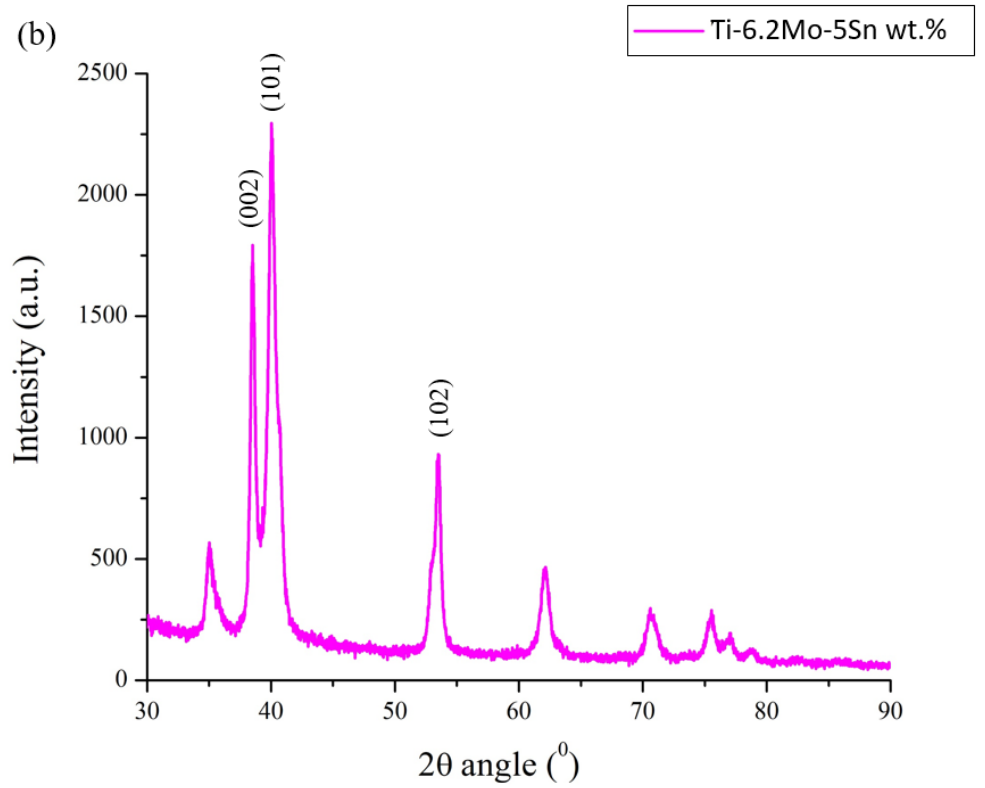
(b)
Ti-6.2Mo-5Sn wt.%
Intensity (a.u.)
2500
2000
1500
1000
500
0
(002)
(101)
(102)
30
40
50
60
70
80
90
2θ angle (0)

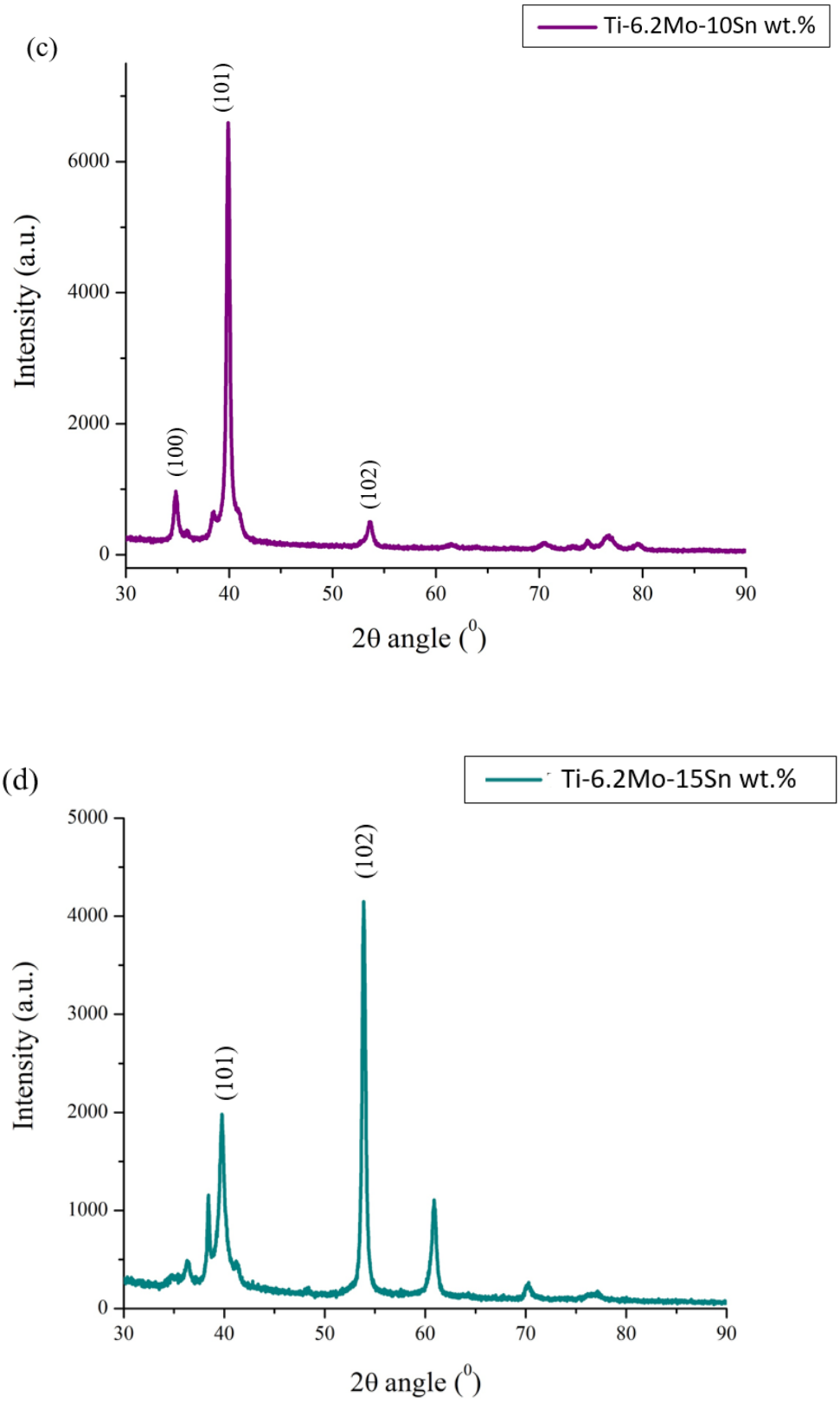

Figure 4.17. XRD patterns of the Ti–6.2Mo–xSn alloys: (a) Ti–6.2Mo, (b) Ti–6.2Mo–5Sn, (c) Ti–6.2Mo–10Sn, and (d) Ti–6.2Mo–15Sn, showing the characteristic reflections of the α-Ti (HCP) phase.

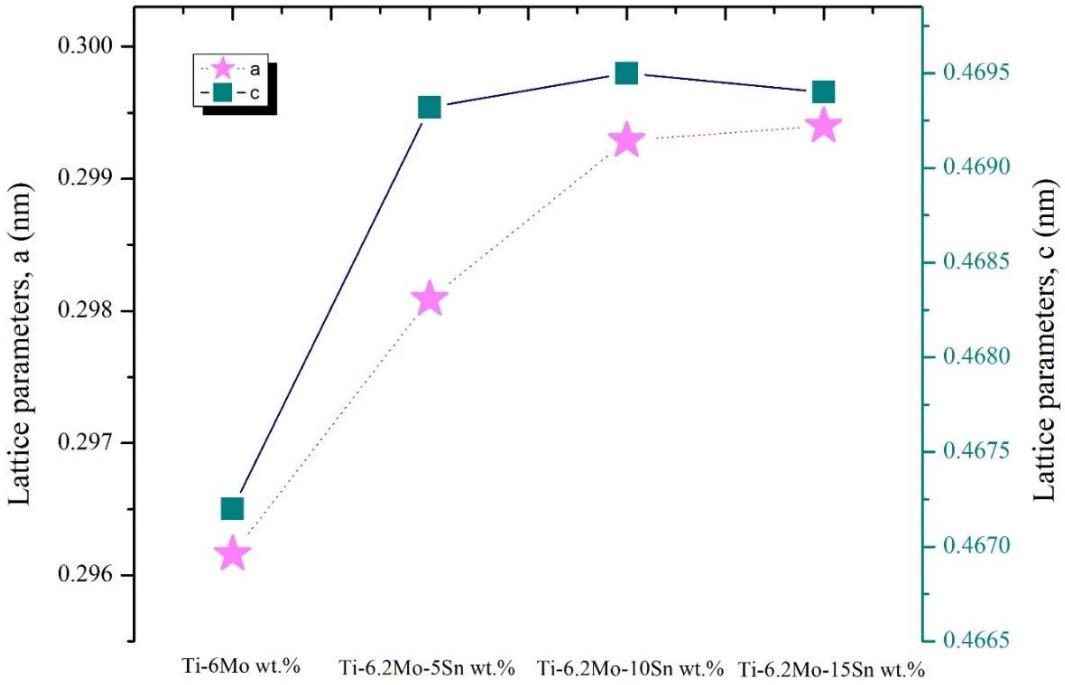

Figure 4.18. Variation of the lattice parameters *a* and *c* of the α-Ti phase as a function of Sn content determined from XRD analysis.

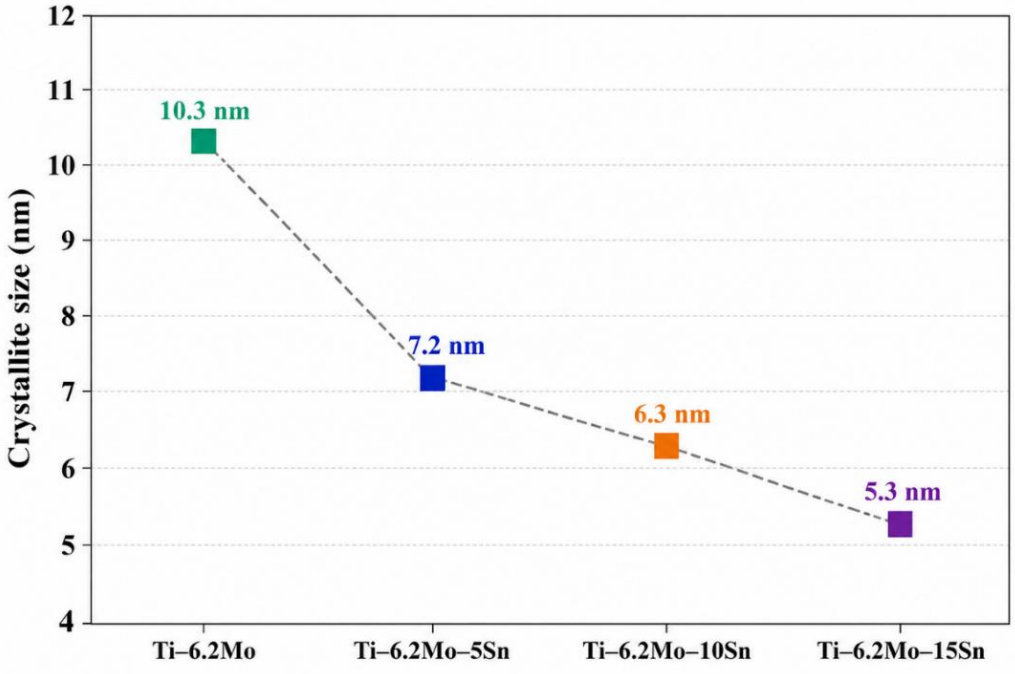

Figure 4.19. Variation of crystallite size with increasing Sn content determined from XRD peak broadening analysis.

The diffraction pattern of the TiMo alloy exhibited the characteristic reflections of the α-Ti phase with a hexagonal close-packed crystal structure. The most intense peaks observed at approximately 38.5° and 40.2° were indexed as the (002) and (101) reflections, respectively, while the weaker reflections at higher diffraction angles corresponded to the (102), (200), and (211) planes. It should be noted that highest reflection of (102) plane was recorded for TiMo15Sn sample indicating presence of preferred orientation. The overall diffraction pattern showed good agreement with the reference α-Ti structure ($P6_3/mmc$), with no reflections attributable to retained β-Ti.

The addition of Sn resulted in noticeable modifications of the diffraction behavior. In the TiMo5Sn alloy the broadening of peaks increased, especially in the region of 35-45° where the main α-Ti reflections are located. Some reflections were slightly shifted with respect to the reference α-Ti pattern, indicating modifications of the crystal lattice due to the presence of alloying elements. The positions of the diffraction peaks are directly related to the interplanar distance by the well known Bragg's law:

$$n\lambda = 2d\,sin\theta, \tag{20}$$

where n is the diffraction order, λ is the X-ray wavelength, d is the interplanar spacing, and θ is the Bragg angle. Accordingly, changes in diffraction peak positions reflect changes in the corresponding interplanar spacings and lattice parameters.

The shifts were not identical for all reflections, with some peaks shifting towards lower diffraction angles while others remained nearly unchanged. These non-uniform shifts are consistent with changes in the lattice parameters of the α-Ti phase following alloying with Mo and Sn. The diffraction pattern of the TiMo10Sn alloy was characterized by a more pronounced (101) reflection and a decrease in the intensity of several secondary reflections. Compared with the TiMo5Sn alloy, the diffraction peaks were more localized and the background intensity was reduced. Variations in the relative peak intensities may also indicate the presence of preferred crystallographic orientations developed during alloy processing.

Among the investigated alloys, TiMo15Sn exhibited the most pronounced changes in the relative intensities of the diffraction peaks. The intensity of the (102) reflection increased considerably, while the relative intensity of the (101) reflection decreased compared with the other alloys. Such variations in relative peak intensities may indicate changes in the preferred orientation of the α-Ti crystallites. Broader peak profiles observed in several regions of the diffraction pattern may reflect contributions from reduced crystallite size and lattice strain.

The lattice parameters obtained from XRD pattern (Figure 4.18) showed an overall increase in both *a* and *c* with increasing Sn content. The lattice parameter *a* increased from 2.962 Å for the TiMo alloy to 2.994 Å for the TiMo15Sn alloy, while the *c* parameter increased from 4.672 Å to approximately 4.694–4.695 Å. This trend is consistent with changes in the α-Ti lattice associated with increasing Sn incorporation and the corresponding modification of the interplanar spacings.

A progressive decrease in the XRD-derived crystallite size was observed with increasing Sn content (Figure 4.19). The estimated crystallite size decreased from 10.3 nm in the TiMo alloy to 7.2, 6.3, and 5.3 nm in the TiMo5Sn, TiMo10Sn, and TiMo15Sn alloys, respectively. This trend is consistent with the increased diffraction-peak broadening observed in the Sn-containing alloys.

Within the detection capability of the XRD analysis, all investigated alloys therefore exhibited a predominantly α-Ti structure, accompanied by changes in the lattice parameters and XRD-derived crystallite size with increasing Sn content.

4.7.3 Microstructure and EBSD characterization

The reduced elastic modulus determined by nanoindentation at 24 different locations of the Ti–6.2Mo alloy ranged from 98.11 to 108.56 GPa, with an average of 103.87 GPa. Despite the relatively small overall variation of the elastic modulus, pronounced local variations of the elastic response were observed over the investigated area.

To investigate the origin of these variations, the nanoindentation results were correlated with the EBSD inverse pole figure (IPF) and image quality (IQ) maps shown in Figure 4.20. The highest measured modulus value (108.56 GPa) was obtained within a grain exhibiting a pink coloration in the IPF map. According to the crystallographic color coding, this orientation is closer to the [0001] direction, for which higher reduced elastic modulus values are generally expected due to the intrinsic

elastic anisotropy of α-titanium. This observation is therefore consistent with the known orientation dependence of elastic properties in HCP titanium.

In contrast, the lowest modulus values were measured at locations situated directly on or very close to grain and lamella boundaries. As indicated in Figure 4.20, these indentation sites coincide with interfaces separating neighboring α lamellae and regions of different crystallographic orientation. Under such conditions, the indentation response may be influenced simultaneously by adjacent microstructural regions, resulting in a measured modulus that does not represent the behavior of a single orientation. In addition, these interfaces are characterized by increased local heterogeneity, which may further contribute to the observed reduction in modulus.

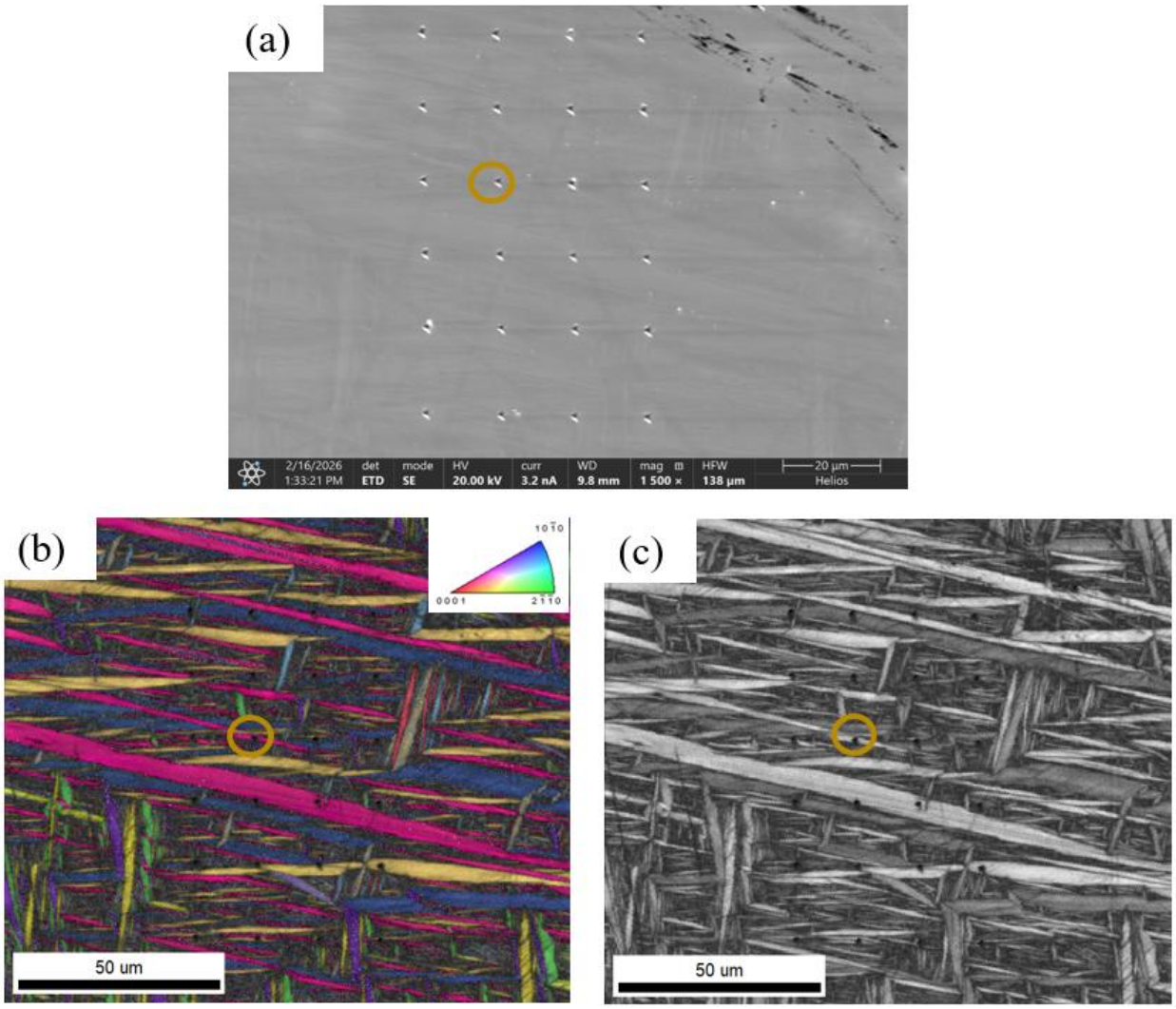

Figure 4.20. Nanoindentation locations and corresponding EBSD maps of the Ti–6.2Mo alloy: (a) SEM image, (b) IPF map, and (c) IQ map. Highlighted points indicate locations used for detailed analysis of the elastic modulus.

Nanoindentation measurements performed on the Ti–6.2Mo–5Sn alloy showed reduced elastic modulus values ranging from 74.08 to 93.25 GPa, with an average value of 83.12 GPa. Compared with the Ti–6.2Mo alloy, this represents a pronounced decrease in the average modulus, indicating that the addition of 5 wt.% Sn contributes to a reduction in the local elastic stiffness of the alloy.

The indentation point located within the yellow-colored grain exhibited a modulus of 83.84 GPa, which is very close to the average value obtained for this sample. According to the IPF color coding, this grain corresponds to an intermediate crystallographic orientation between the [0001] and

$[10\bar{1}0]$ directions (Figure 4.21). Therefore, its modulus can be interpreted as an intermediate elastic response, rather than as an unusually high or low value.

In contrast, the lowest modulus values were mainly associated with darker regions in the microstructural/EBSD image. These areas may correspond to regions of reduced image quality, local lattice distortion, surface relief, or interfaces between fine α lamellae. Therefore, the lowest values should not be attributed only to crystallographic orientation. They more likely reflect the combined influence of local microstructural heterogeneity, lamellar interfaces, and possible surface/topographic effects on the nanoindentation response.

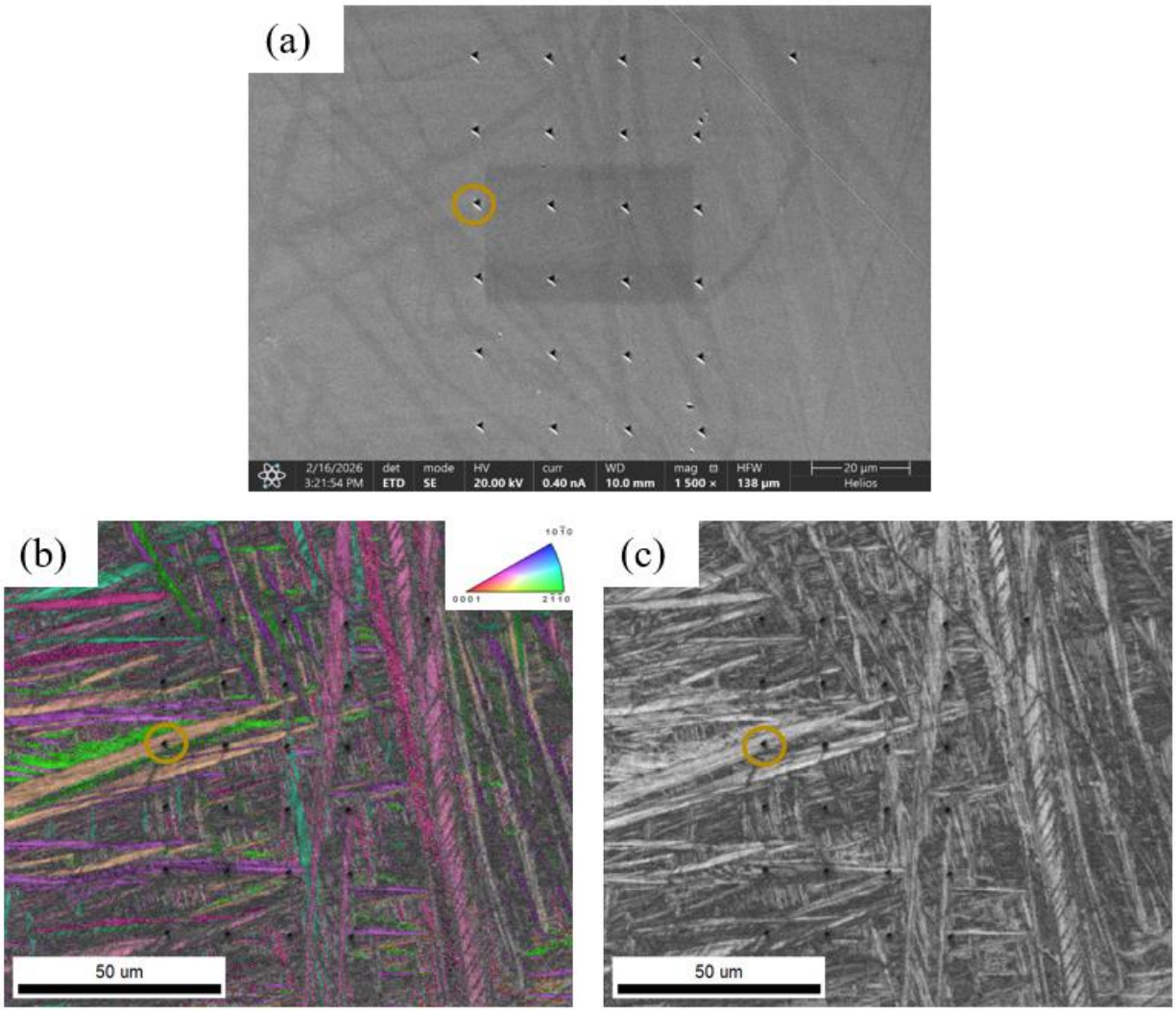

Figure 4.21. Nanoindentation locations and corresponding EBSD maps of the Ti–6.2Mo-5Sn alloy: (a) SEM image, (b) IPF map, and (c) IQ map. Highlighted points indicate locations used for detailed analysis of the elastic modulus.

Nanoindentation measurements performed on the Ti–6.2Mo–10Sn alloy revealed reduced elastic modulus values ranging from 85.57 to 92.85 GPa, with an average value of 88.97 GPa. Compared with the Ti–6.2Mo–5Sn alloy, the modulus distribution was noticeably narrower, indicating a more uniform local elastic response.

A correlation between crystallographic orientation and reduced elastic modulus was observed. The indentation point located within a green-colored grain, corresponding to an orientation closer to the $[10\bar{1}0]$ direction, exhibited a modulus of 87.42 GPa. In contrast, the indentation point positioned within an orange-colored grain, associated with an orientation closer to the [0001] direction, showed a higher modulus of 91.14 GPa (Figure 4.22). This trend is consistent with the known elastic

anisotropy of α-titanium, where orientations closer to the c-axis generally exhibit higher elastic modulus values than those aligned with a-directions.

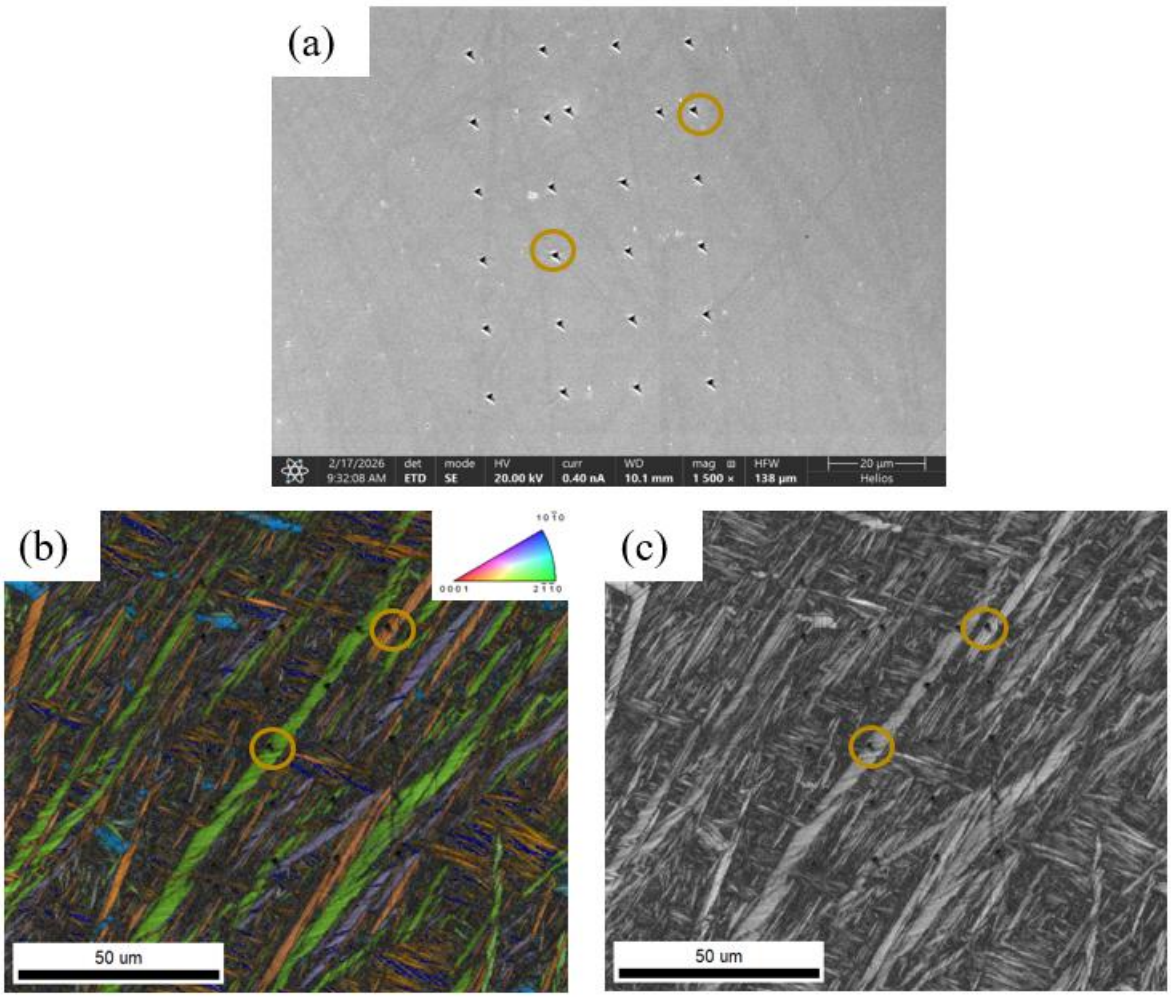

Figure 4.22. Nanoindentation locations and corresponding EBSD maps of the Ti–6.2Mo-10Sn alloy: (a) SEM image, (b) IPF map, and (c) IQ map. Highlighted points indicate locations used for detailed analysis of the elastic modulus.

Nanoindentation measurements performed on the Ti–6.2Mo–15Sn alloy revealed reduced elastic modulus values ranging from 82.35 to 92.02 GPa, with an average value of 87.37 GPa. Similar to the Ti–6.2Mo–10Sn alloy, the modulus values were distributed within a relatively narrow range, indicating a fairly uniform elastic response across the investigated microstructure.

The selected indentation points exhibited only minor variations in reduced elastic modulus despite being located in grains with different crystallographic orientations. The green-colored grain, corresponding to an orientation close to the $[2\bar{1}\bar{1}0]$ direction, exhibited a modulus of 86.00 GPa, whereas the turquoise-colored grain, positioned between the $[2\bar{1}\bar{1}0]$ and $[10\bar{1}0]$ corners of the IPF triangle, showed a slightly smaller value of 84.84 GPa (Figure 4.23). The relatively small difference between the measured values is expected, since both orientations are located within the a-direction sector of the IPF triangle and are therefore associated with similar elastic responses.

Overall, the EBSD assisted nanoindentation analysis indicates that local variations in elastic modulus are influenced by both crystallographic orientation and microstructural heterogeneity. In particular, orientations approaching the [0001] direction generally exhibit higher modulus values, whereas measurements performed near lamellar or grain boundaries tend to show lower and more scattered responses.

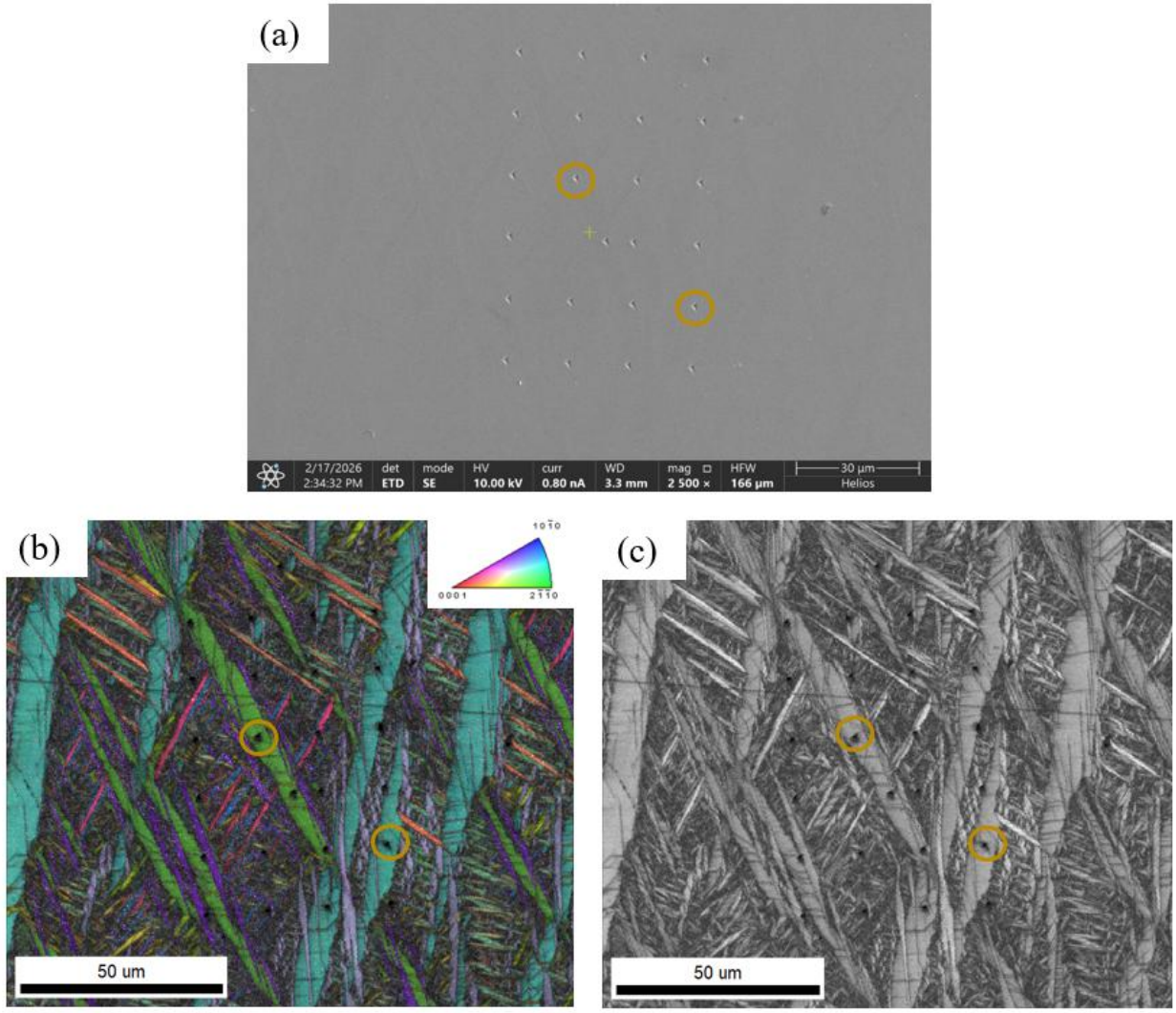

Figure 4.23. Nanoindentation locations and corresponding EBSD maps of the Ti–6.2Mo-15Sn alloy: (a) SEM image, (b) IPF map, and (c) IQ map. Highlighted points indicate locations used for detailed analysis of the elastic modulus.

4.7.4 Quantitative characterization of α-lamella morphology and orientation distribution

4.7.4.1 Orientation distribution

The orientation distribution of α lamellae within the analysed regions changed considerably with increasing Sn content (Figure 4.24). In the Ti–6.2Mo alloy, the microstructure was dominated by lamellae oriented close to the [0001] direction, which occupied 42.5% of the analyzed area. With increasing Sn content, the fraction of this orientation gradually decreased, reaching only 9.4% in the Ti–6.2Mo–15Sn alloy.

In contrast, the fraction of lamellae oriented close to the $[2\bar{1}\bar{1}0]$ direction increased continuously from 3.0% in Ti–6.2Mo to 33.5% in Ti–6.2Mo–15Sn. The $[10\bar{1}0]$ orientation group exhibited less systematic behavior, showing a sharp decrease in the Ti–6.2Mo–5Sn alloy followed by a gradual increase at higher Sn contents.

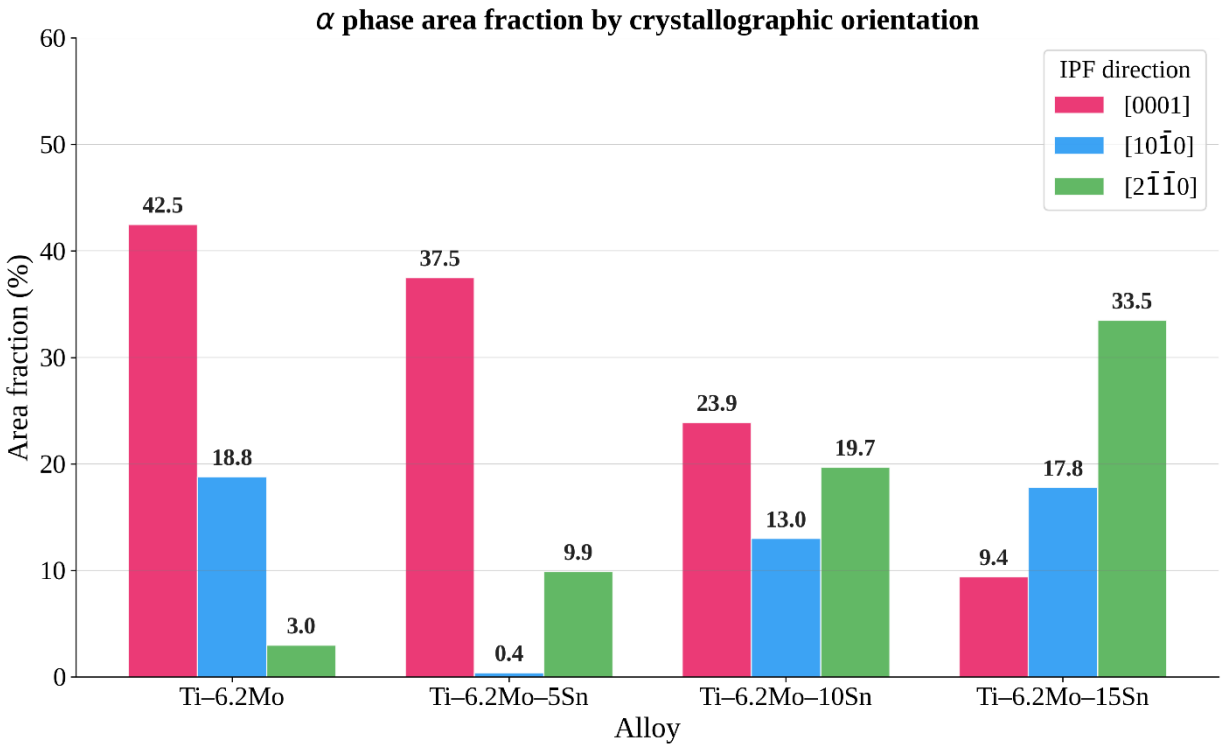

Figure 4.24. Orientation distribution of α lamellae determined by MIPAR analysis for Ti–6.2Mo and Ti–6.2Mo–xSn alloys. The values represent the area fraction of lamellae associated with the [0001], [10$\bar{1}$0], and [2$\bar{1}\bar{1}$0]orientation groups.

4.7.4.2 α-Lamellar thickness

The average thickness of α lamellae belonging to the three dominant crystallographic orientation groups is presented in Figure 4.25. The results show that the variation in lamellar thickness with increasing Sn content differs among the three crystallographic orientation groups.

The [0001] orientation group exhibited a continuous decrease in mean lamellar thickness with increasing Sn content. The average thickness decreased from 1.45 ± 1.19 μm in the Ti–6.2Mo alloy to 0.60 ± 0.30 μm in the Ti–6.2Mo–15Sn alloy, indicating progressive refinement of lamellae associated with this orientation. A similar tendency was observed for the [10$\bar{1}$0] group, whose average thickness decreased from 1.10 ± 0.91 μm to values below 0.75 μm after Sn addition. On the other side, the [2$\bar{1}\bar{1}$0] orientation group exhibited the opposite behavior. The average thickness increased from 0.73 ± 0.53 μm in Ti–6.2Mo to 1.32 ± 1.32 μm in Ti–6.2Mo–15Sn, becoming the coarsest lamellar population in the alloy with the highest Sn content.

Despite the relatively large scatter in the measured values, systematic trends with Sn content can be observed for some orientation groups. In addition to changing the distribution of the orientation groups, Sn also affects the thickness of α lamellae associated with each orientation.

The combined analysis of the orientation distribution and lamellar thickness suggests that Sn addition influences both the morphology and crystallographic distribution of α phase. The decrease in the fraction of lamellae oriented close to the [0001] direction, accompanied by an increase in the proportion of [2$\bar{1}\bar{1}$0]-oriented lamellae, indicates a systematic change in the crystallographic orientation distribution within the analysed regions. The mean lamellar thickness of the [0001] and [10$\bar{1}$0] orientation groups generally decreased with Sn addition, whereas the [2$\bar{1}\bar{1}$0] group showed an increasing tendency.

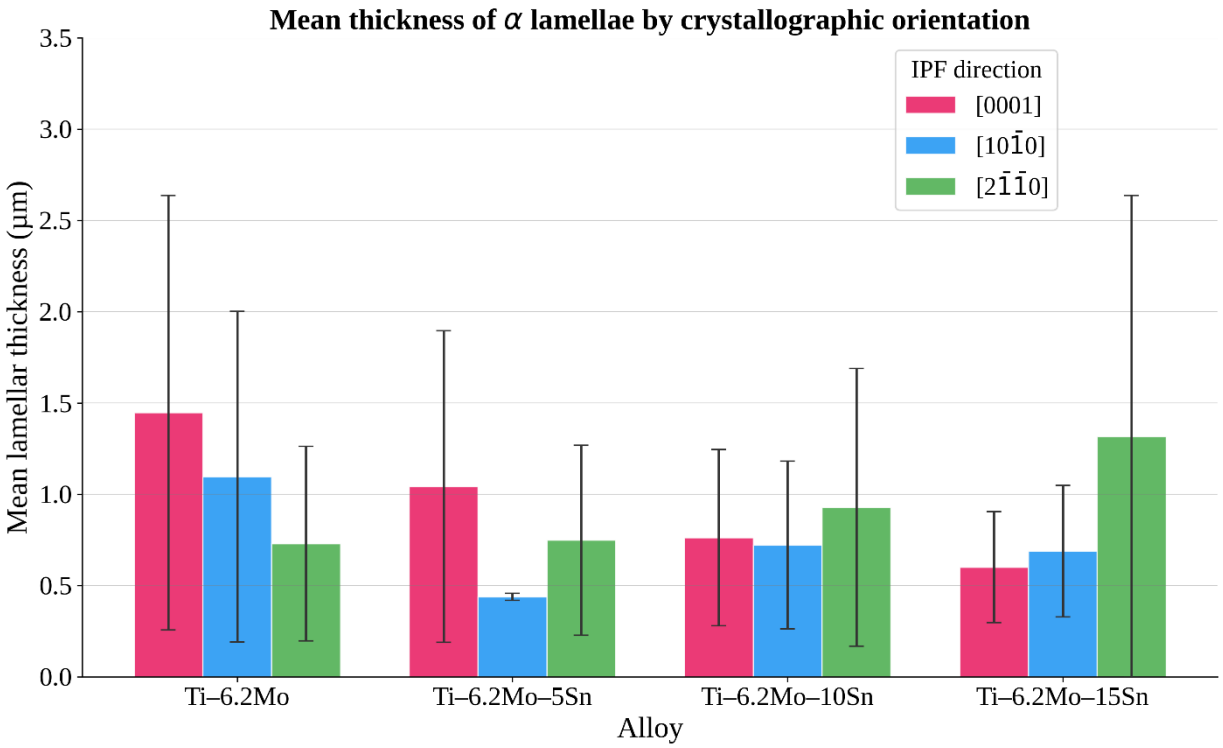

Figure 4.25. Mean thickness of α lamellae associated with the [0001], [10$\bar{1}$0], and [2$\bar{1}\bar{1}$0] crystallographic orientation groups in Ti–6.2Mo and Ti–6.2Mo–xSn alloys determined by MIPAR analysis. Error bars represent one standard deviation.

Considering the elastic anisotropy of α-titanium, these microstructural changes may contribute to the differences in Young's modulus observed among the investigated alloys. In particular, the reduction in the fraction of [0001]-oriented lamellae and the increasing contribution of [2$\bar{1}\bar{1}$0] orientations could influence the overall elastic response of the material. However, it should be noted that the present analysis was performed on a limited number of representative EBSD regions, and therefore the observed trends should be considered indicative rather than definitive. Consequently, the elastic behavior is likely affected by the combined influence of crystallographic orientation, lamellar morphology, and local microstructural heterogeneity.

4.7.5 Nanoindentation response

The measured nanoindentation properties exhibited a certain degree of local variability across the analysed areas (Figure 4.26), consistent with the heterogeneous α-lamellar microstructure observed by EBSD. The largest spatial variations in reduced modulus were observed in the Ti–6.2Mo and Ti–6.2Mo–5Sn alloys, whereas the Ti–6.2Mo–10Sn and Ti–6.2Mo–15Sn alloys exhibited a more uniform distribution of indentation properties. Compared to reduced modulus and hardness, the plasticity index remained relatively uniform within each alloy.

Nanoindentation results for all investigated alloys are summarized in Figure 4.27. The Ti–6.2Mo alloy exhibited the highest average reduced elastic modulus (103.87 GPa) and hardness (4.15 GPa). The Sn-containing alloys exhibited lower average elastic modulus values than the Sn-free Ti–6.2Mo alloy, with average values of 83.12, 88.97, and 87.37 GPa for Ti–6.2Mo–5Sn, Ti–6.2Mo–10Sn, and Ti–6.2Mo–15Sn, respectively. Although the dependence on Sn content was not monotonic, all three Sn-containing alloys showed a pronounced reduction in average modulus relative to Ti–6.2Mo (103.87 GPa). The addition of 5 wt.% Sn caused a pronounced decrease in hardness from 4.15 to approximately 3.00 GPa. Further increases in Sn content resulted in a slight recovery of hardness, reaching average values of 3.14 and 3.23 GPa for the Ti–6.2Mo–10Sn and Ti–6.2Mo–15Sn alloys, respectively.

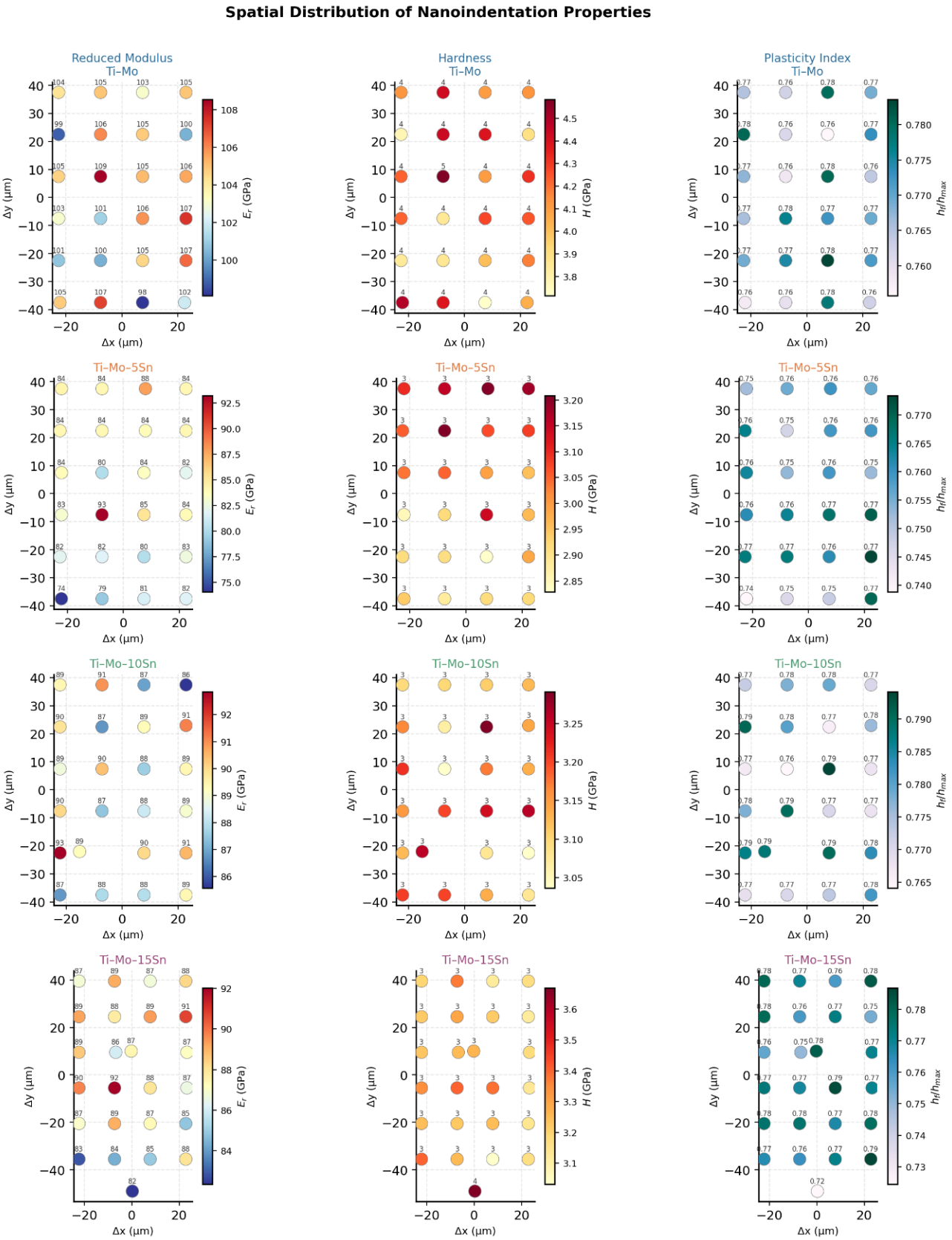

Figure 4.26. Spatial distribution of nanoindentation properties across the investigated Ti–6.2Mo and Ti–6.2Mo–xSn alloys: reduced modulus (Er), hardness (H), and plasticity index (hr/hmax).

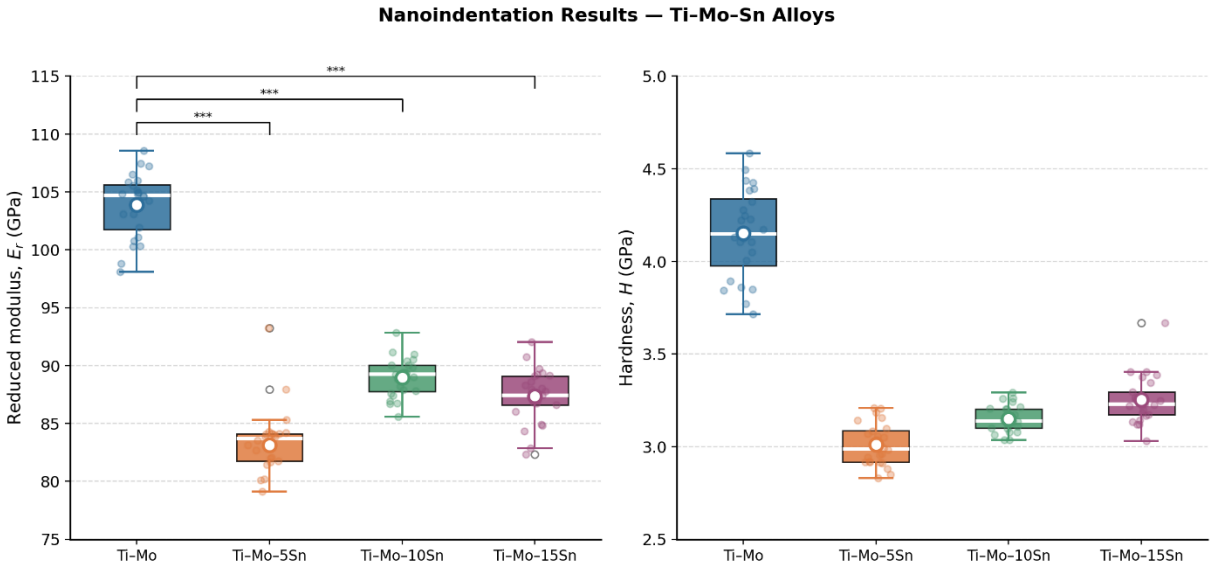

Figure 4.27. Nanoindentation results showing the reduced elastic modulus (Er) and hardness (H) of the Ti–6.2Mo and Ti–6.2Mo–xSn alloys.

The nanoindentation measurements revealed differences not only in average values but also in the distribution of the obtained data. The Ti–6.2Mo–5Sn alloy exhibited the largest scatter in reduced elastic modulus values, consistent with a greater variability of the local indentation response. Conversely, the Ti-6.2Mo-10Sn and Ti-6.2Mo-15Sn alloys showed narrower distributions of modulus, indicating a more homogeneous local elastic response. The nanoindentation results were correlated to EBSD analysis and showed that grains oriented closer to the [0001] direction generally showed higher modulus values than grains closer to the a-directions, in agreement with the elastic anisotropy of α-titanium. Local variations in response related to grain boundaries, lamellar interfaces and regions of poor image quality were also observed. The lower modulus values of the Sn-containing alloys cannot be attributed solely to the local crystallographic orientations examined by EBSD. The XRD results also showed changes in the α-Ti lattice parameters with increasing Sn content, indicating that alloying modifies the crystal structure of the α phase. The measured modulus values may therefore reflect the combined influence of composition, crystallographic orientation, and local microstructural features. Therefore, the measured modulus values are likely governed by a combination of crystallographic orientation, local microstructural features, and Sn-induced modifications of the crystal lattice.

The plasticity index remained within a relatively narrow range for all investigated alloys, with no clear systematic variation with Sn content (Figure 4.28). In contrast to the plasticity index, the Oliver–Pharr exponent exhibited a noticeable increase after Sn addition. While the Ti–6.2Mo alloy displayed average values below the ideal elastic-plastic reference (m = 1.5), the Sn-containing alloys exhibited values close to or above this threshold. This behavior suggests a modification of the indentation response and indicates that Sn addition affects the balance between elastic recovery and irreversible deformation.

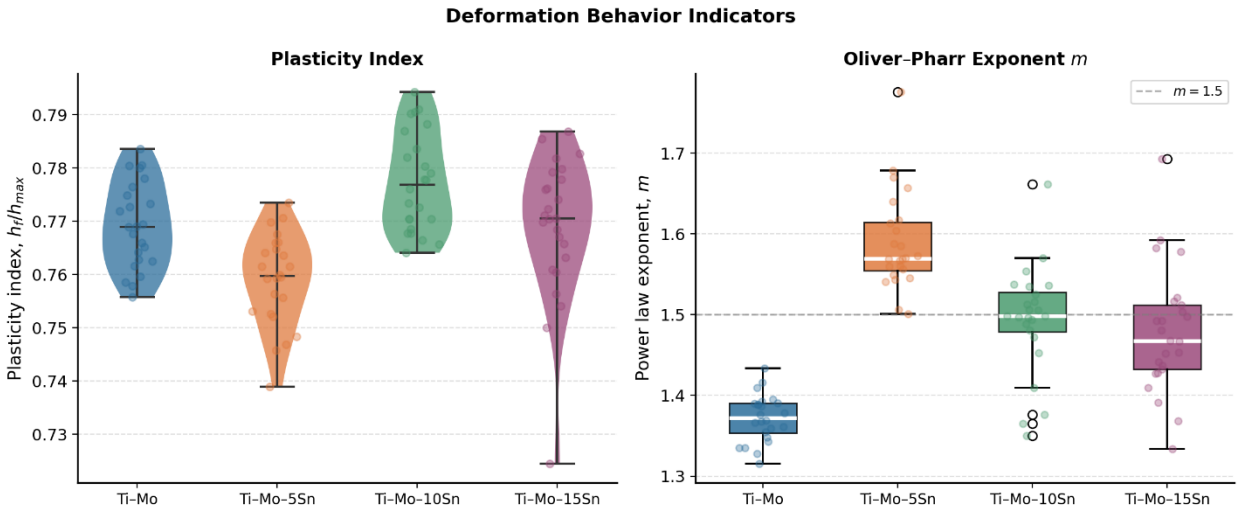

Figure 4.28. Comparison of deformation behavior parameters obtained from nanoindentation for Ti–Mo–Sn alloys: plasticity index (h_r/h_{max}) and Oliver–Pharr exponent (m).

Figure 4.29 shows the reduced modulus plotted against hardness for all the indentation measurements. The results clearly distinguish the investigated alloys into different groups based on their mechanical behavior. The Ti–6.2Mo alloy displayed the highest reduced modulus and hardness, with the majority of measurements in the range of ~100–109 GPa and 3.7–4.6 GPa, respectively. In contrast, all Sn-containing alloys were shifted toward lower modulus and hardness values.

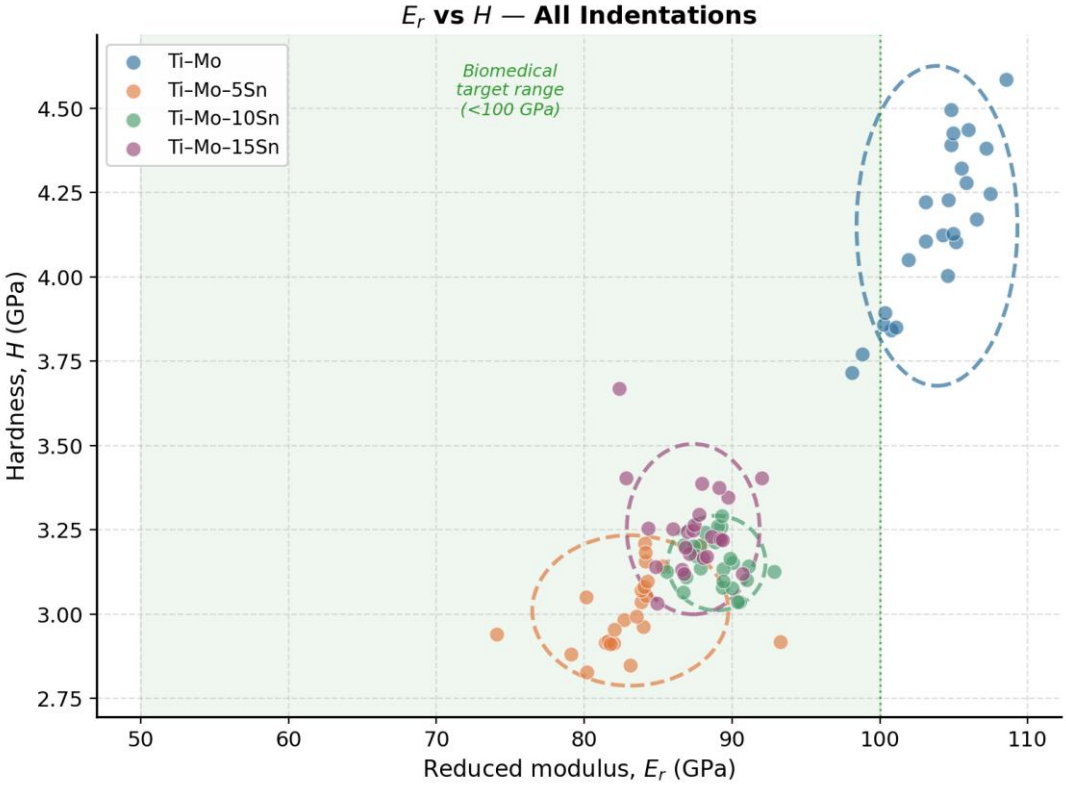

Figure 4.29. Scatter plot showing the relationship between reduced modulus (Er) and hardness (H) for all nanoindentation measurements performed on Ti–6.2Mo and Ti–6.2Mo–xSn alloys. The shaded area represents the targeted modulus range for biomedical applications (Er < 100 GPa).

The most pronounced change was observed after the addition of 5 wt.% Sn. Compared with Ti–6.2Mo, the Ti–6.2Mo–5Sn alloy showed a substantial decrease in reduced modulus accompanied by a reduction in hardness. This shift is reflected not only in the average values but also in the position of the entire data cluster, indicating that the decrease in stiffness represents a systematic effect of alloying rather than the influence of a limited number of individual measurements.

Further increasing the Sn content from 5 to 10 and 15 wt.% did not produce an additional significant reduction in modulus. The Ti–6.2Mo–10Sn and Ti–6.2Mo–15Sn alloys exhibited similar distributions of indentation data, with reduced modulus values predominantly between 85 and 92 GPa and hardness values around 3.0–3.4 GPa. This behavior suggests that the largest modification of the local mechanical behavior occurs after the initial addition of Sn, whereas further increases in Sn content mainly maintain the reduced stiffness achieved in the Ti–6.2Mo–5Sn alloy.

From the perspective of biomedical applications, all Sn-containing alloys exhibited reduced modulus values below 100 GPa, whereas the Ti–6.2Mo alloy remained predominantly above this level. Considering that the elastic modulus of conventional Ti–6Al–4V is typically reported to be around 110 GPa, the lower indentation modulus values obtained for the Sn-containing alloys indicate a shift towards lower elastic stiffness compared with the Sn-free Ti–6.2Mo alloy. At the same time, the reduction in modulus was accompanied by lower, but still clearly measurable, hardness values of approximately 3.0–3.3 GPa. Overall, these results demonstrate that the incorporation of Sn modifies the local mechanical behavior of the investigated Ti–6.2Mo–xSn alloys, producing a substantial reduction in indentation modulus while maintaining measurable resistance to localized plastic deformation.

4.8 CALPHAD analysis of phase stability in the Ti–Mo–Sn system

The CALPHAD analysis was used to place the experimentally observed phase constitution of the Ti–6.2Mo–xSn alloys in a thermodynamic context. Although the XRD analysis showed a predominantly α-Ti structure in the processed alloys, the samples were homogenised at 1000 °C before water quenching and subsequent cold rolling. The calculated binary and ternary phase diagrams were therefore examined to identify the equilibrium phase fields relevant to the homogenisation temperature and to assess how the addition of Sn modifies phase stability within the Ti–Mo–Sn system.The calculated Ti–Mo (Figure 4.30) binary diagram reproduces the β-isomorphous behaviour of the system, with a broad body-centered cubic (BCC) solid-solution field extending over a large compositional range at elevated temperatures. Ordered Mo–Ti phases appear only at lower temperatures in the calculated diagram. The calculated phase relations are consistent with the well-established β-stabilising role of Mo in titanium alloys and provide the binary reference for the subsequent ternary analysis.

The calculated Ti–Sn binary diagram shows markedly different phase behaviour (Figure 4.31). In contrast to the broad BCC solid-solution field observed in the Ti–Mo system, the Ti–Sn system contains several intermediate phases and a more restricted Ti-rich solid-solution region. The calculated binary diagram therefore shows that the role of Sn cannot be described simply in terms of β-phase stabilisation, and its combined effect with Mo must be considered within the ternary Ti–Mo–Sn system.

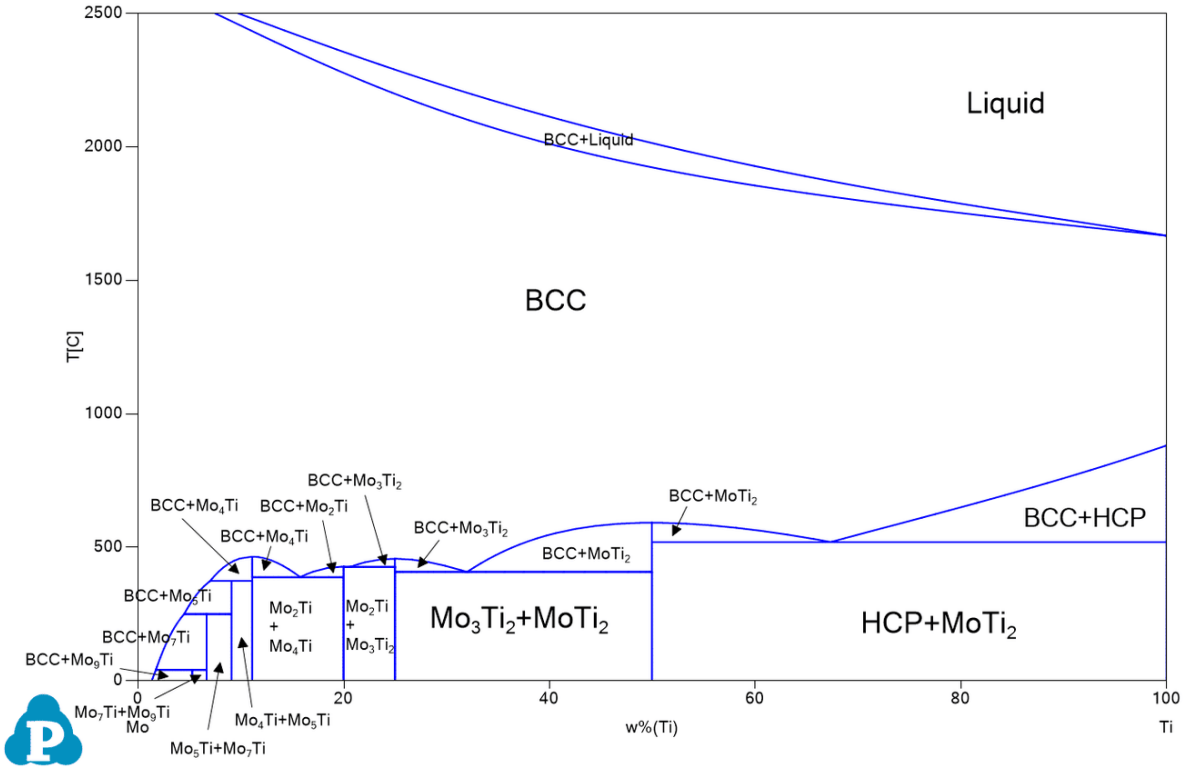

Figure 4.30. Ti–Mo binary phase diagram calculated using the PANDAT software.

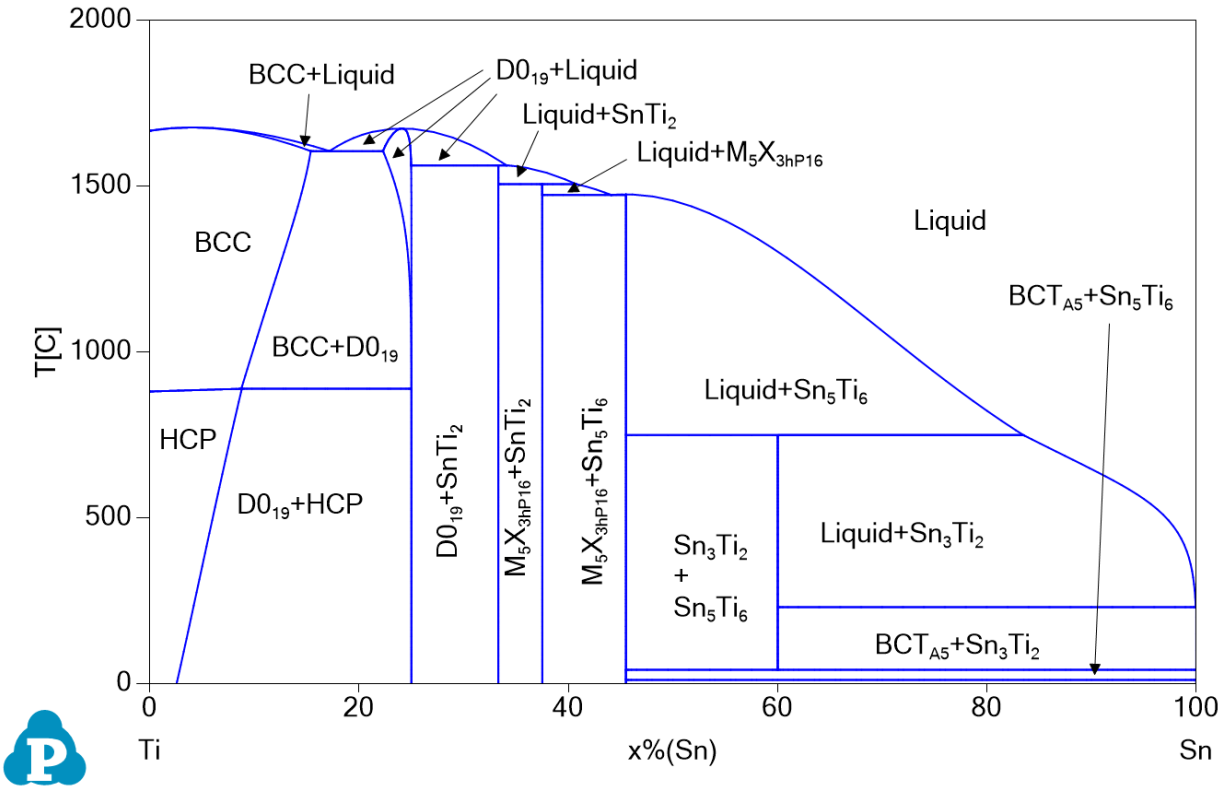

Figure 4.31. Ti–Sn binary phase diagram calculated using the PANDAT software.

At 1000 °C, corresponding to the homogenisation temperature used for the investigated alloys, the Ti–Mo–Sn isothermal section shows a broad BCC phase field on the Ti-rich side of the ternary system (Figure 4.32). The equilibrium phase constitution at this temperature therefore differs substantially from that subsequently observed at room temperature by XRD. Importantly, the 1000

°C section describes equilibrium phase stability during homogenisation and should not be interpreted as the final phase constitution after water quenching and cold rolling.

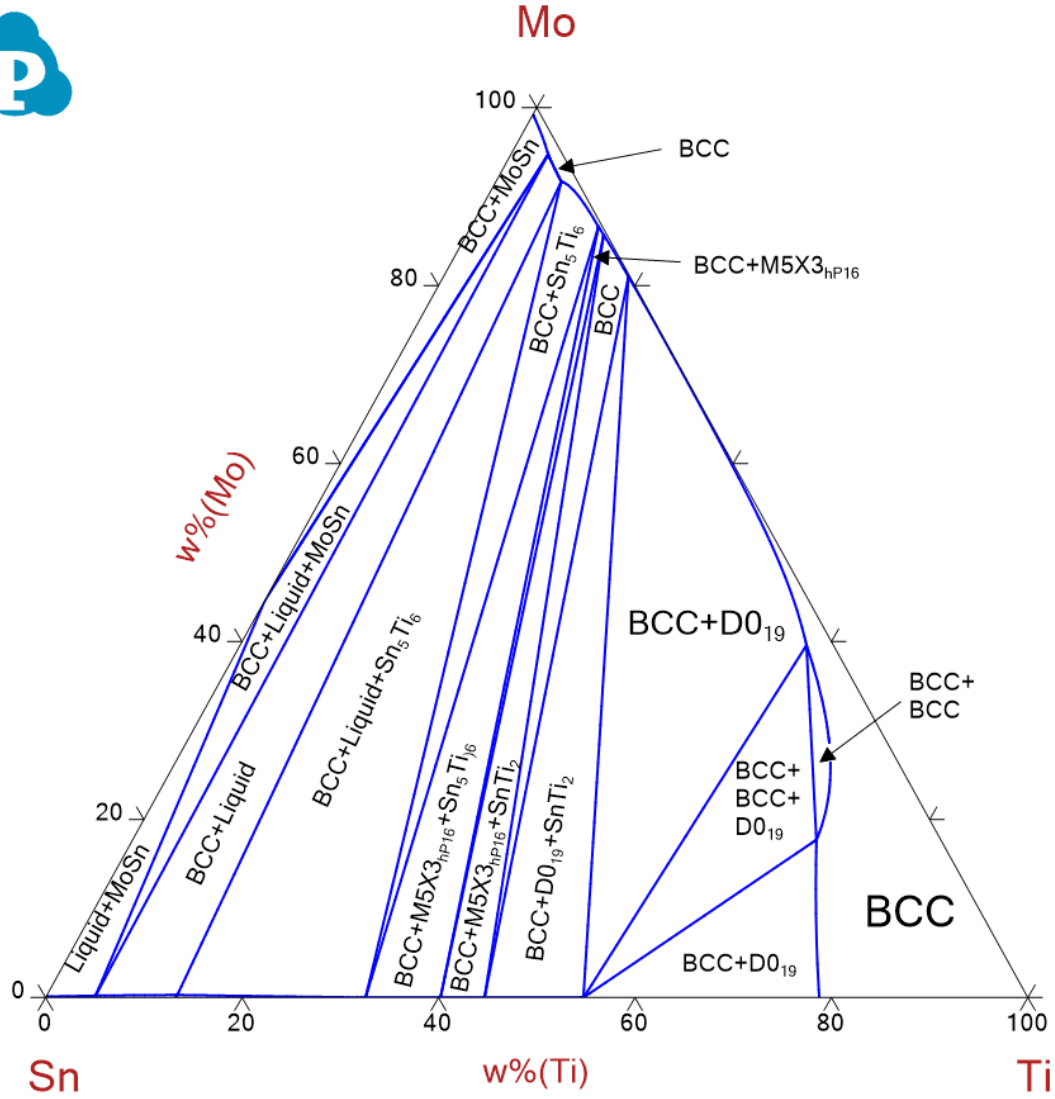

Figure 4.32. Calculated isothermal section of the Ti–Mo–Sn system at 1000 °C (PANDAT).

A substantially different phase distribution is obtained at 100 °C (Figure 4.33). The BCC phase field is strongly reduced compared with the high-temperature section, while several multiphase regions containing HCP and intermetallic phases become thermodynamically stable. Of particular relevance to the present alloys is the Ti-rich region of the diagram, where the HCP + $MoTi_2$ phase field extends over a broad compositional range. The Ti–6.2Mo–xSn compositions investigated experimentally are located close to this Ti-rich region, which is qualitatively consistent with the predominantly HCP α-Ti structure identified by XRD. However, no clearly distinguishable reflections corresponding to $MoTi_2$ were detected experimentally. This difference is not unexpected, since the CALPHAD section represents equilibrium phase stability at 100 °C, whereas the experimental alloys were water quenched from 1000 °C and subsequently cold rolled. The final phase constitution may therefore differ from the equilibrium state predicted at low temperature because of kinetic limitations and the applied processing route.

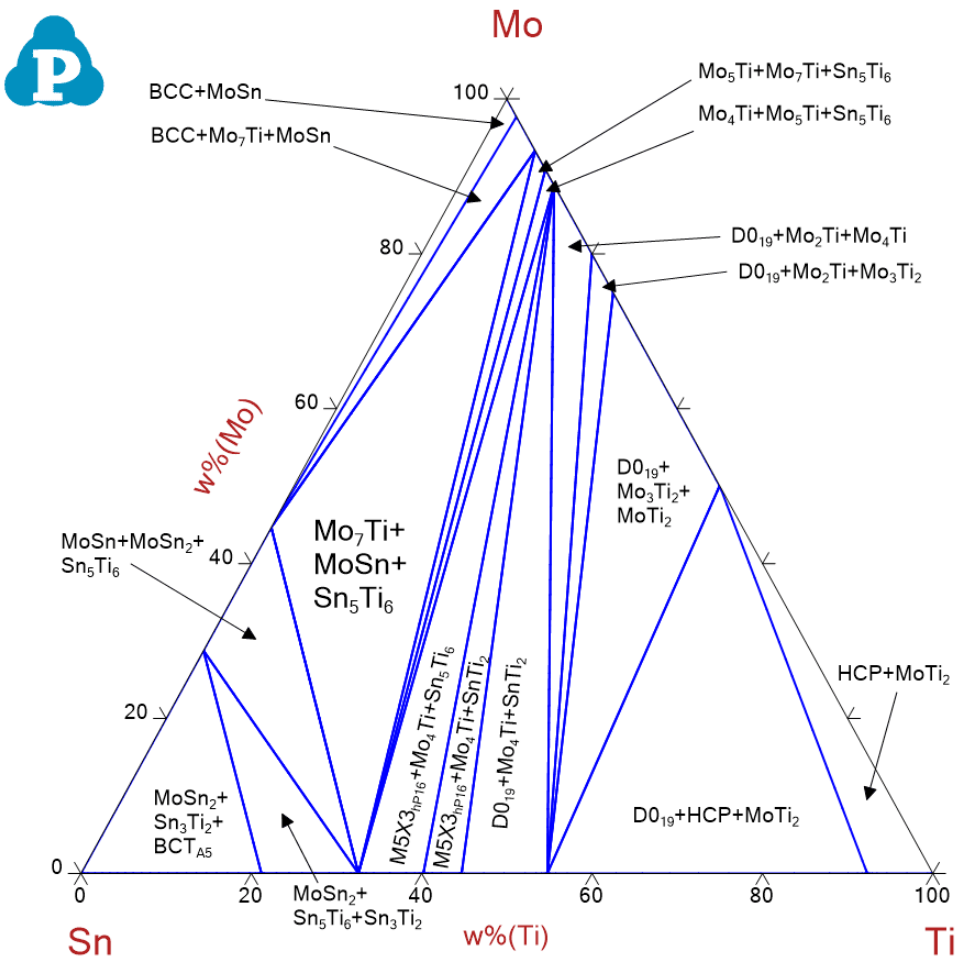

Figure 4.33. Calculated isothermal section of the Ti–Mo–Sn system at 100 °C (PANDAT).

Taken together, the CALPHAD and XRD results provide complementary information on the phase behaviour of the investigated alloys. The phase diagrams describe equilibrium phase stability at selected temperatures, whereas XRD characterizes the final processed state after homogenisation, water quenching, and cold rolling. The predominance of α-Ti observed experimentally indicates that the high-temperature equilibrium phase constitution was not retained unchanged during subsequent processing. At the same time, the thermodynamic calculations demonstrate the strong dependence of phase stability on temperature and composition. CALPHAD therefore provides a thermodynamic framework for interpreting the experimentally observed phase constitution rather than a direct prediction of the final microstructure.

4.9 Atomistic interpretation of orientation-dependent nanoindentation response

The orientation-dependent deformation behaviour of α-titanium introduced in the literature review (Section 2.2) can be examined at the atomistic scale through molecular-dynamics simulations, which provide insight into the early stages of deformation that are difficult to access experimentally. The results presented here, obtained from nanoindentation simulations of single crystalline α-Ti (Markovic and Dominguez-Gutierrez, 2026), are used to provide a qualitative atomistic interpretation of the orientation-dependent response observed in the EBSD assisted nanoindentation experiments. Since the simulations represent pure single crystalline α-Ti, they are not intended to reproduce directly the response of the processed Ti–6.2Mo and Ti–6.2Mo–xSn alloys.

The Schmid factor maps reveal a pronounced dependence of the resolved shear conditions on crystallographic orientation. For the [0001] orientation, regions with high Schmid factors remain strongly localized beneath the indenter, indicating less favourable conditions for widespread basal and prismatic slip. In contrast, the $[10\bar{1}0]$ and $[2\bar{1}10]$ orientations exhibit broader regions with high

Schmid factors, providing more favourable conditions for the activation of basal and prismatic slip systems and a more distributed plastic response (Figure 4.34).

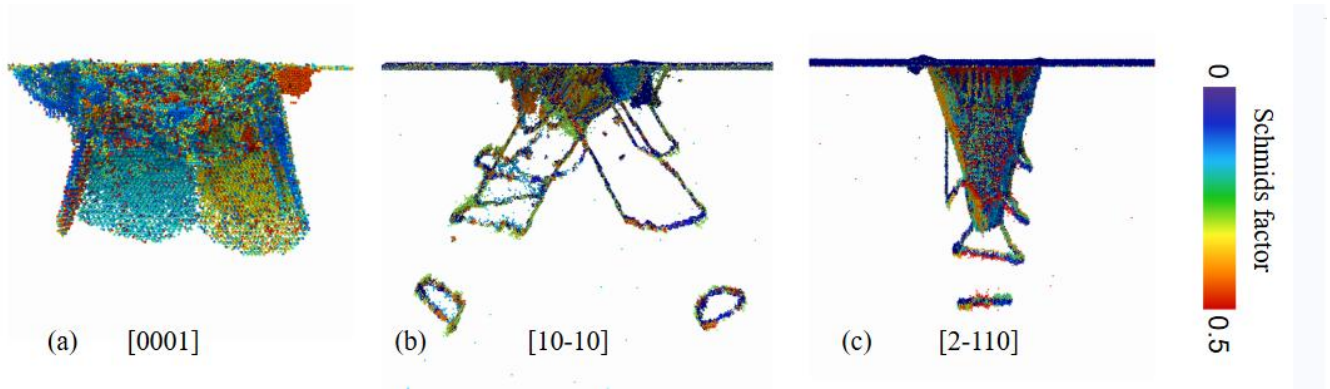

Figure 4.34. Orientation-dependent deformation behavior in single crystalline α-Ti during nanoindentation at 300 K for three crystallographic orientations: (a) [0001], (b) $[10\bar{1}0]$, and (c) $[2\bar{1}\bar{1}0]$. The color scale represents the Schmid factor, highlighting regions favorable for slip activation.

The shear strain maps further illustrate how crystallographic orientation governs the evolution of plastic deformation. In the [0001] orientation, strain remains highly concentrated beneath the indenter, consistent with restricted slip activity and stronger localization of plasticity. Conversely, the $[10\bar{1}0]$ and $[2\bar{1}10]$ orientations develop broader deformation regions associated with enhanced dislocation mobility and the simultaneous activation of multiple slip systems. The more diffuse strain distribution in these orientations indicates more effective strain accommodation and reduced confinement of plastic flow. Representative atomic shear strain maps for different crystallographic orientations are shown in Figure 4.35.

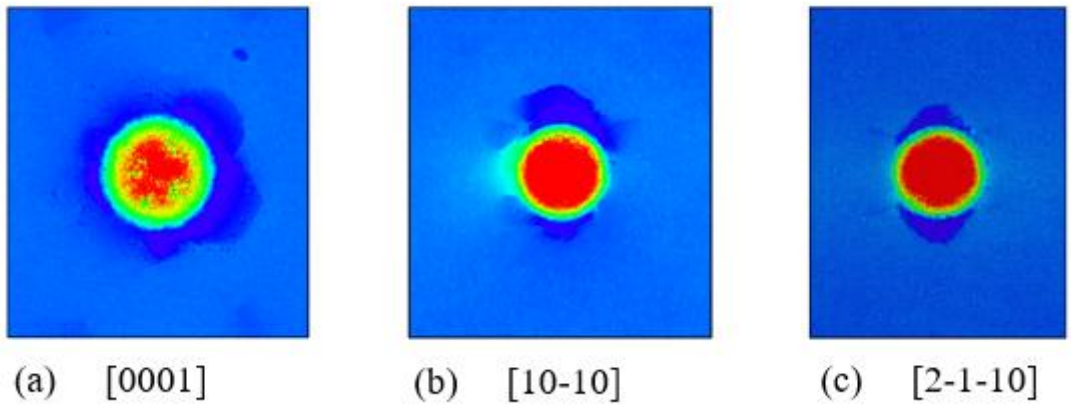

Figure 4.35. Orientation-dependent strain localization in single crystalline α-Ti during nanoindentation at 300 K for three crystallographic orientations: (a) [0001], (b) $[10\bar{1}0]$, and (c) $[2\bar{1}\bar{1}0]$. The color scale represents the local atomic shear strain, highlighting regions of plastic deformation.

This orientation dependence is consistent with the EBSD assisted nanoindentation results, where indentation sites with different crystallographic orientations exhibited different local modulus values. However, the experimental response additionally includes the effects of alloying, lamellar boundaries, neighbouring grains, and local microstructural heterogeneity, which are absent from the single-crystal MD model.

Together, these observations show that the local plastic response of single crystalline α-Ti is strongly dependent on crystallographic orientation, with different loading directions producing different degrees of strain localization and slip activity.

Nanoindentation simulations of single crystalline α-Ti further showed that the onset of plasticity was strongly orientation-dependent. The corresponding load–displacement curves and the evolution of contact pressure at 300 K are presented in Figure 4.36 (a) and 4.36 (b), respectively. For indentation along the [0001] direction, where basal and prismatic slip are geometrically less favourable, the transition from elastic to plastic deformation was associated with a discrete load-drop event, visible as a short plateau in the load–displacement curve at an indentation depth of approximately 1.2 nm. At the atomistic level, this event corresponded to the sudden nucleation of a localized defected region directly beneath the indenter, in which the atoms departed from their HCP coordination. In contrast, indentation along the prismatic orientations showed a more gradual transition to plastic deformation, associated with the formation and evolution of dislocation loops through the lasso-like mechanism identified in the atomistic simulations.

The differences in deformation mechanisms are also reflected in the mechanical response shown in Figure 4.36. Throughout the indentation, the [0001] orientation sustained systematically higher loads than the two prismatic orientations, reaching 2.14 μN at a depth of 4 nm compared with 1.87 μN for $[10\bar{1}0]$ and 1.83 μN for $[2\bar{1}10]$, and it exhibited a correspondingly higher contact pressure over the entire depth range (Figure 4.36b). The [0001] curve also showed a sharper deviation from the initial elastic response, whereas the prismatic orientations displayed a smoother, more serrated evolution of the indentation load, indicating that plastic deformation was accommodated through a larger number of smaller, sequential events rather than a single localized instability. These differences are consistent with the orientation-dependent strain localization and slip behaviour observed in the atomistic configurations and shear-strain maps (Markovic and Dominguez-Gutierrez, 2026).

These atomistic results provide additional context for interpreting the orientation-dependent nanoindentation response observed experimentally. The EBSD assisted measurements presented in Section 4.7.3 showed that indentation sites with different crystallographic orientations exhibited different local modulus values. In particular, regions with orientations approaching the [0001] direction generally showed higher modulus values, whereas orientations closer to the a-directions exhibited lower values within the analysed regions. The MD simulations complement these observations by showing that crystallographic orientation also affects the mechanisms by which deformation is accommodated beneath the indenter. However, a direct quantitative correspondence between the simulated and experimental responses should not be expected. The simulations represent pure single crystalline α-Ti, whereas the experimental Ti–6.2Mo and Ti–6.2Mo–xSn alloys contain alloying elements and a complex lamellar microstructure, including grain and lamella boundaries and neighbouring regions of different crystallographic orientation.

Taken together, the atomistic simulations and EBSD assisted nanoindentation experiments provide complementary descriptions of orientation-dependent mechanical behaviour. The simulations demonstrate how crystallographic orientation affects slip activity, strain localization, and the onset of plastic deformation in single crystalline α-Ti, while the experiments show that orientation-dependent variations are also present in the local mechanical behavior of the synthesized Ti–6.2Mo and Ti–6.2Mo–xSn alloys. The correspondence between the two approaches is therefore qualitative rather than quantitative, with the MD simulations providing an atomistic interpretation of orientation-dependent deformation and the experimental response additionally reflecting the effects of alloy composition and the complex lamellar microstructure.

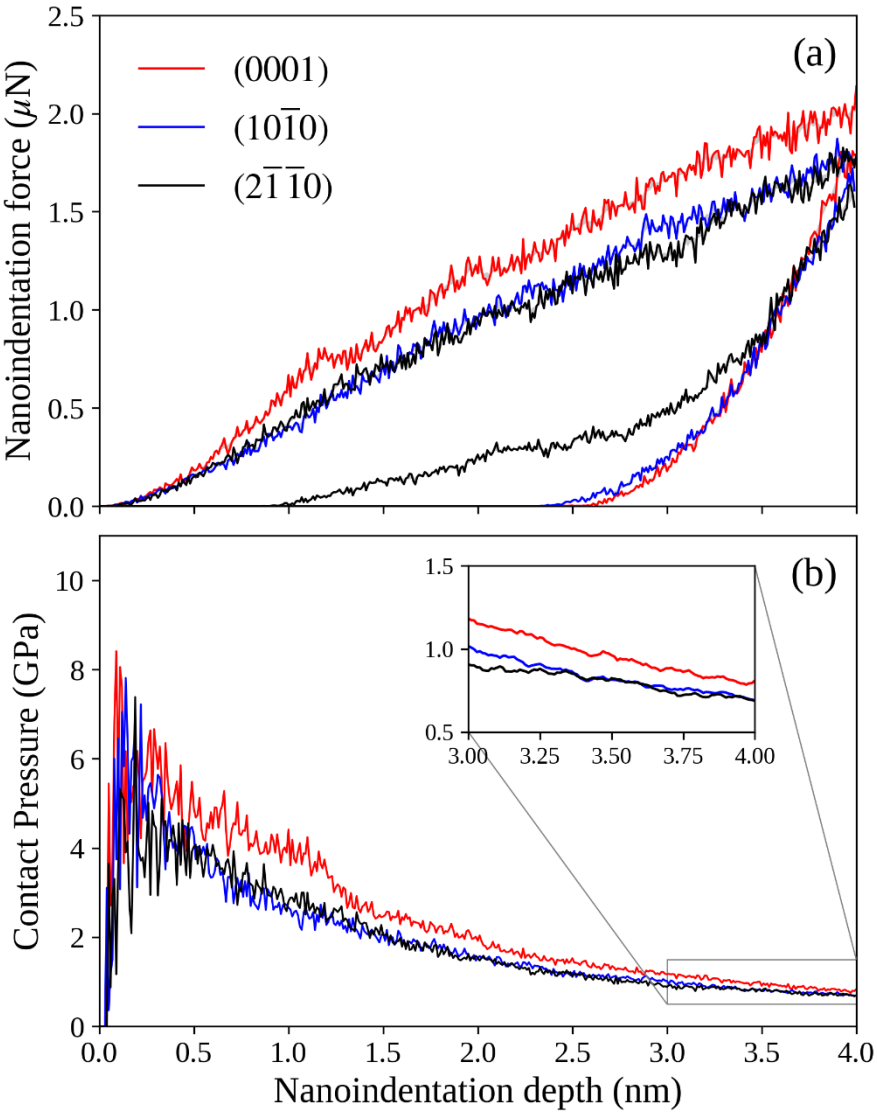

Figure 4.36. Load–displacement curves (a) and contact pressure (b) evolution during nanoindentation of single crystalline α-Ti at 300 K. In both panels, the rows correspond to the [0001], [10$\bar{1}$0], and [2$\bar{1}$10] crystallographic orientations, from top to bottom.

4.10 Comparison with model predictions

4.10.1 Origin of alpha phase formation in designed alloys

The phase analysis showed that all synthesized alloys were predominantly composed of α phase. This result should be considered in relation to both alloy composition and the applied processing route. Although Mo is a well-established β-stabilizing element, the influence of Sn on phase stability is more complex and cannot be described solely in terms of β-phase stabilization, as also indicated by the CALPHAD analysis presented in Section 4.8.

The β-stabilizing tendency of the investigated alloys was first evaluated using the Mo equivalency expression given in Equation (4). Since the investigated compositions contain only Mo and Sn as alloying elements, the calculated values increase from 6.2 for Ti–6.2Mo to 7.7, 9.2, and 10.7 for Ti–6.2Mo–5Sn, Ti–6.2Mo–10Sn, and Ti–6.2Mo–15Sn, respectively. These values indicate an increasing empirical β-stabilizing tendency with increasing Sn content. However, Mo equivalency should be interpreted only as an approximate composition-based indicator and does not directly predict the phase constitution retained after processing. Although Sn contributes positively to the calculated Mo equivalency, its coefficient is considerably lower than that of stronger β-stabilizing

elements. Consequently, the increase in $[Mo]_{eq}$ with Sn addition should not be interpreted as direct evidence for β-phase retention in the processed alloys.

A useful comparison is provided by Li et al. (2023), who investigated the related Ti–8Mo–xSn system. In that alloy series, compositions containing up to 9 wt.% Sn exhibited α″ martensite, while a β + α″ structure was reported at 11 wt.% Sn and predominantly β structures at higher Sn contents, particularly for Ti–8Mo–13Sn and Ti–8Mo–15Sn. The present alloys contain 6.2 wt.% Mo, and direct comparison with the Ti–8Mo–xSn series should therefore be made cautiously. Nevertheless, these literature results illustrate that the final phase constitution depends on the combined Mo and Sn contents rather than on Sn concentration alone.

The CALPHAD results presented in Section 4.8 provide additional thermodynamic context for the experimentally observed phase constitution. At 1000 °C, corresponding to the homogenisation temperature used in this work, the Ti-rich region of the ternary Ti–Mo–Sn system contains a broad BCC stability field. At lower temperature, however, the calculated equilibrium phase relations shift towards HCP-containing regions. In particular, the Ti-rich region of the 100 °C isothermal section contains an HCP + $MoTi_2$ phase field, which is qualitatively consistent with the predominance of the HCP α-Ti phase identified experimentally by XRD. No clearly distinguishable reflections corresponding to $MoTi_2$ were detected experimentally.

The possible presence of a small fraction of α″ martensite cannot be completely excluded. Unlike α-Ti, which has an HCP crystal structure, α″ martensite has an orthorhombic structure and can, in principle, be distinguished by XRD. However, no clearly resolved diffraction reflections attributable to α″ were observed in the present XRD patterns. If present only in a small fraction, its reflections may be weak and partially overlap with the dominant α-Ti reflections, making unambiguous identification difficult under the present experimental conditions. The XRD results therefore support a predominantly α-Ti structure but do not provide sufficient evidence to confirm the presence of α″ martensite. Additional high-resolution characterization would be required to determine whether a minor martensitic fraction is present.

4.10.2 Comparison between machine-learning predictions and experiments

The Ti–6.2Mo–xSn series provides an experimental assessment of whether composition-based screening can identify alloys with reduced elastic stiffness after synthesis and thermomechanical processing. None of the four investigated compositions was present as an experimental record in the model-training database. Their experimental characterization therefore provides an independent assessment of the predictions obtained from the literature-based dataset. Since the model represents each candidate through elemental composition and composition-derived descriptors, the predicted values reflect the phase and processing states represented indirectly within the available literature data.

For comparison with the experimental results, the model inputs were recalculated using the compositions determined by EDS. The measured EDS totals of 100.0, 100.1, 99.9, and 100.1 wt.% were first normalised to 100 wt.%, resulting in Ti–Mo–Sn compositions of 94.30–5.70–0.00, 88.31–5.79–5.89, 82.38–6.41–11.21, and 77.62–6.09–16.28 wt.%, respectively. All 16 composition-derived descriptors were then recalculated using these values. The corresponding mean five-neighbour distances were 0.62, 0.85, 0.75, and 1.12, all below the applicability-domain threshold of 1.407. Although the highest experimentally measured Sn content slightly exceeds the 16 wt.% limit used during compositional screening, it therefore remains within the descriptor-based applicability domain. Phase analysis revealed predominantly α-phase lamellar microstructures in all four experimental alloys.

The [Mo]eq,W1 descriptor calculated from the normalised EDS compositions increased from 5.70 for Ti–6.2Mo to 7.56, 9.77, and 10.98 for the three Sn-containing alloys, indicating an increasing empirical β-stabilising tendency. However, as discussed in Section 4.10.1, the final phase constitution

cannot be interpreted from Mo equivalency alone and also reflects alloy composition and processing history. In the related Ti–8Mo–xSn system, Li et al. (2023) reported α″ martensite and β + α″ structures, with predominantly β structures at the highest Sn contents. The lower Mo content and different processing route applied in the present work resulted in a different final phase constitution. The present comparison therefore evaluates the model for compositions located within its applicability domain, but exhibiting a microstructural state that is not explicitly represented by the composition-derived descriptors. Nanoindentation provided the reduced elastic modulus, Er, which was converted to Young's modulus, E, as described in Section 3.6.5. The resulting values are presented in Table 4.15.

Table 4.15. Average reduced elastic modulus (E_r) and corresponding Young's modulus (E_s) obtained from nanoindentation measurements for the investigated alloys.

Alloy	(E_r) (GPa)	(E_s) (GPa)
Ti–6.2Mo	103.87	101.02
Ti–6.2Mo–5Sn	83.12	79.26
Ti–6.2Mo–10Sn	88.97	85.31
Ti–6.2Mo–15Sn	87.37	83.65

Figure 4.37 compares the experimentally determined Young's modulus values with the model predictions calculated using the normalised EDS compositions. The vertical bars represent the empirical 90% prediction range derived from absolute errors obtained for publications excluded during grouped validation. This range provides an estimate of the prediction uncertainty when the model is applied to data from an unseen publication and therefore represents a more appropriate uncertainty measure for experimental comparison than the variation among individual trees within the fitted Random Forest.

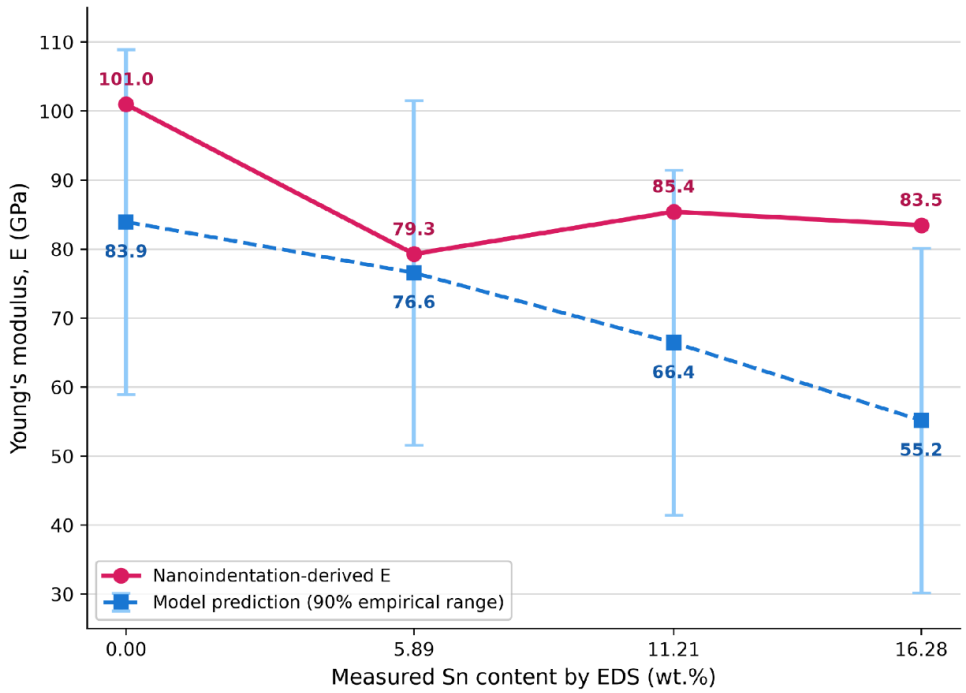

Figure 4.37. Comparison of machine-learning predictions and experimentally measured Young's modulus values for Ti–6.2Mo–xSn alloys.

For the experimentally determined compositions, the predicted Young's modulus values were 83.9, 76.6, 66.4, and 55.2 GPa with increasing Sn content. The corresponding differences between the experimental and predicted values were +17.1, +2.7, +18.9, and +28.5 GPa, respectively. All experimental values were therefore higher than the corresponding predictions. The mean absolute error for the four experimental compositions was approximately 16.8 GPa, while the root-mean-square error was approximately 19.1 GPa, reflecting the greater contribution of the larger deviations. The closest agreement was obtained for Ti–6.2Mo–5Sn, for which the experimental and predicted values differed by only 2.7 GPa.

The first three experimental values fall within the empirical 90% prediction ranges, whereas Ti–6.2Mo–15Sn slightly exceeds the upper boundary of its 90% range while remaining within the empirical 95% range. The experimental results are therefore generally consistent with the broader prediction uncertainty established through publication grouped validation. At the same time, the common positive direction of the residuals indicates that the model systematically underestimated Young's modulus for this experimental alloy series.

Part of this systematic difference may be associated with the measurement method. The earlier analysis of method-labelled literature data indicated that nanoindentation derived modulus values were approximately 5.0–7.5 GPa higher than tensile-derived values when assessed against the same composition models. However, the available dataset contained only a limited number of explicitly labelled measurements, and the group-level analysis did not identify a statistically significant separation between measurement methods ($\eta 2=0.014$, permutation $p=0.339$). The observed method-associated difference should therefore be regarded as an approximate empirical scale rather than a correction applied to the present measurements. Nevertheless, it may contribute to part of the positive difference between the predicted and experimentally determined values.

An important agreement between the predicted and experimental results is observed after the introduction of Sn. Experimentally, Young's modulus decreased from 101.02 GPa for Ti–6.2Mo to 79.26 GPa for the alloy containing 5.89 wt.% Sn, corresponding to a reduction of approximately 21.8 GPa. Further increases in Sn content resulted in comparatively smaller variations, with all three Sn-containing alloys exhibiting modulus values between approximately 79 and 85 GPa. The model similarly predicted a decrease following Sn addition, but continued to predict progressively lower modulus values with increasing Sn content. Thus, the model captured the initial tendency towards modulus reduction associated with the introduction of Sn, while overestimating the magnitude of the continued decrease at higher Sn concentrations.

The source-exclusion analysis performed during Ti–Mo–Sn screening provides further insight into this behavior. When the Ti–8Mo–xSn series reported by Li et al. (2023) was excluded from model development, the predicted modulus for the experimentally measured Ti–6.2Mo–15Sn composition increased from 55.2 to 68.7 GPa. This change of approximately 13.5 GPa demonstrates the strong influence of the principal literature source covering the high-Sn region on the predicted trend. The experimentally determined value of 83.65 GPa remained higher, suggesting that differences in the phase constitution and processing state of the synthesized alloy also contribute to the observed discrepancy.

The predominantly α-lamellar microstructures observed experimentally provide additional context for these differences. The investigated alloys were homogenised at 1000 °C for 2 h, water quenched, and subsequently cold rolled by approximately 20%. These processing conditions, together with the resulting phase constitution, lamellar morphology, crystallographic orientation, and local microstructural heterogeneity, are not explicitly included among the model inputs. The composition-derived electronic, atomic-size, and β-stability descriptors describe composition-dependent tendencies, whereas nanoindentation measures the local elastic response of the microstructure produced by the actual processing route.

Overall, the experimental series supports the use of the developed model for identifying a promising reduced modulus compositional region within the Ti–Mo–Sn system. All three Sn-containing alloys exhibited nanoindentation derived Young's modulus values between approximately 79 and 85 GPa, confirming the potential of the compositional space identified through machine-learning screening. The experimental characterization additionally provides the processing- and microstructure-specific information required to establish the elastic response of the selected compositions.

4.10.3 Limitations revealed by the experimental validation

The experimental validation highlights several limitations that should be considered when applying composition-based machine-learning models to titanium alloy design. The developed model uses elemental composition and composition-derived descriptors and therefore captures systematic relationships between alloy chemistry and Young's modulus represented in the literature database. As demonstrated by the Ti–6.2Mo–xSn experimental series, however, the elastic response of a processed alloy also reflects its final phase constitution and microstructural state. These effects are only indirectly represented in a composition-based model.

A broader limitation arises from the structure of the available literature data. Chemical composition and mechanical properties are commonly reported, whereas processing conditions and quantitative microstructural information are less consistently documented. Consequently, variables describing phase fractions, crystallographic texture, grain and lamella dimensions, heat-treatment conditions, and deformation history cannot be incorporated systematically across the complete dataset. The experimental results obtained in this work illustrate the importance of such information, particularly when alloys with similar compositions develop different structural states.

The publication grouped validation strategy and the applicability-domain analysis partly address these limitations by providing a more realistic estimate of model transferability and by identifying whether new compositions are represented within the descriptor space of the training data. The experimental Ti–6.2Mo–xSn compositions were located within this applicability domain, and their results were generally consistent with the broader prediction uncertainty established during grouped validation. At the same time, the systematic underprediction observed for the experimental series shows that compositional similarity does not necessarily imply an equivalent processing or microstructural state.

Further development of predictive models for titanium alloys would therefore benefit from databases in which composition is complemented by consistently reported processing and quantitative microstructural information. Incorporating such variables would allow the relationships between composition, processing, microstructure, and mechanical properties to be represented more explicitly. The present results provide a basis for this development by demonstrating both the effectiveness of composition-based screening for identifying promising alloy systems and the additional information obtained through targeted experimental validation.

5. Conclusions

The main findings of this research work can be summarized as follows:

1. A curated database of biocompatible titanium alloys was assembled under a strict scope that keeps every record to the same measured quantity (Young's modulus) and to conventional, dense products; the Young's modulus modelling domain comprised 240 experimental records.
2. Composition-based machine-learning models were developed under publication grouped (leave-publication-out) validation. For Young's modulus, a Random Forest with the 16 composition-derived descriptors gave the best compact model (nested $R^2 = 0.417$, MAE = 11.50 GPa), whereas a conventional random split gave a higher but over-optimistic $R^2 = 0.597$.
3. The share of modulus variance associated with alloy-system identity (~40%; $\eta^2 = 0.457$, $\omega^2 = 0.417$) is close to the model's explained variance, showing that the model captures approximately as much as composition alone can explain; the remainder is governed by processing, phase constitution, texture and microstructure.
4. Yield strength ($R^2 = 0.277$) and ultimate tensile strength ($R^2 = 0.149$, rising to 0.268 with processing variables) were predicted with larger uncertainty and are treated as exploratory.
5. Feature analysis identified the d-orbital energy Md and the correlated electronic and β-stability descriptors as the most consistent predictors, while the classical Bo–Md and e/a–Δr classifications carried little direct modulus information.
6. Computational screening of the Ti–Mo–Sn system located a low-modulus region and selected Ti–6.2Mo–xSn (x = 5, 10, 15 wt.%) for synthesis.
7. The alloys were arc-melted and showed high relative density, homogeneous composition and a predominantly α-lamellar microstructure (no β detected by XRD). The nanoindentation derived Young's modulus was 101.02 (Ti–6.2Mo), 79.26 (5Sn), 85.31 (10Sn) and 83.65 GPa (15Sn); Sn reduced the modulus relative to Ti–6.2Mo, with the lowest value at 5 wt.% Sn.
8. Against the model predictions at the measured EDS compositions (83.9, 76.6, 66.4 and 55.2 GPa), all four experimental values were higher (residuals +2.7 to +28.5 GPa; MAE 16.8 GPa, RMSE 19.1 GPa). The model captured the direction of the initial modulus reduction with Sn but exaggerated the continued decrease at higher Sn content; part of the systematic positive offset is consistent with the 5–7.5 GPa nanoindentation-versus-tensile scale difference, and part with the metastable α microstructure that composition descriptors cannot resolve.
9. Excluding the principal Ti–8Mo–xSn source (Li et al., 2023) raised the Ti–6.2Mo–15Sn prediction from 55.2 to 68.7 GPa, showing that the model's steep high-Sn behaviour depends strongly on a single publication.
10. EBSD assisted nanoindentation and microstructural quantification linked the local modulus to the crystallographic orientation of the α lamellae ([0001]-near grains being stiffer), and atomistic simulations of single-crystal α-Ti reproduced this orientation dependence, providing the mechanism behind the measured anisotropy; CALPHAD analysis provided the thermodynamic context, with the equilibrium β field versus the experimental α phase consistent with the low molybdenum-equivalency and the metastable, quenched state.
11. Overall, machine learning successfully identified a promising low-modulus system, while the experiments showed that the realized modulus is controlled by microstructure and processing, not by composition alone; composition-based screening therefore narrows the search but cannot replace experimental validation.

12. Future work should enlarge and more completely annotate the database with quantitative microstructural and processing data, add process- and phase-aware descriptors, and extend validation to heat-treated and deformed states.

In summary, this research work demonstrates the potential of the relatively unexplored Ti–Mo–Sn system for the development of biomedical titanium alloys with reduced elastic modulus. The results provide new insight into the influence of Sn on the structural and elastic behavior of Ti–Mo-based alloys and demonstrate the effectiveness of a machine-learning-guided strategy for identifying and experimentally validating promising alloy compositions. Therefore, obtained results strongly support further research in the field of biomaterials based on titanium alloys.

References

1. Abdel-Hady, M.; Hinoshita, K.; Morinaga, M. General approach to phase stability and elastic properties of β-type Ti-alloys using electronic parameters. Scripta Materialia 55(5) (2006), 477–480. https://doi.org/10.1016/j.scriptamat.2006.04.022

2. Ahmad, F.N.; Hussain, Z.; A Brief Review on the Properties of Titanium as a Metallic Biomaterials; International Journal of Electroactive Materials; 8 (2020), 63–67.

3. Apaza-Bedoya, K.; Tarce, M.; Benfatti, C. A.; Henriques, B.; Mathew, M. T.; Teughels, W.; Souza, J. C. Synergistic interactions between corrosion and wear at titanium-based dental implant connections: a scoping review. Journal of Periodontal Research 52(6) (2017), 946–954. https://doi.org/10.1111/jre.12469

4. Bahl, S.; Suwas, S.; Chatterjee, K. Comprehensive review on alloy design, processing, and performance of β titanium alloys as biomedical materials. International Materials Reviews 66(2) (2021), 114–139. https://doi.org/10.1080/09506608.2020.1735829

5. Banerjee, D.; Williams, J. C. Perspectives on titanium science and technology. Acta Materialia 61(3) (2013), 844–879. https://doi.org/10.1016/j.actamat.2012.10.043

6. Bania, P. J. Beta titanium alloys and their role in the titanium industry. JOM 46(7) (1994), 16–19. https://doi.org/10.1007/bf03220742

7. Banumathy, S.; Prasad, K. S.; Mandal, R. K.; Singh, A. K. Effect of thermomechanical processing on evolution of various phases in Ti-Nb alloys. Bulletin of Materials Science 34(7) (2011), 1421–1434. https://doi.org/10.1007/s12034-011-0338-3

8. Beese, A. M. Microstructure and mechanical properties of AM builds. In: Thermo-Mechanical Modeling of Additive Manufacturing. Butterworth-Heinemann (2018), 81–92. https://doi.org/10.1016/b978-0-12-811820-7.00007-0

9. Beisekenov, N.; Sadenova, M.; Azamatov, B.; Syrnev, B. Analysis of biomechanical characteristics of bone tissues using a Bayesian neural network: A narrative review. Journal of Functional Biomaterials 16(5) (2025), 168. https://doi.org/10.3390/jfb16050168

10. Bignon, M.; Bertrand, E.; Rivera-Díaz-Del-Castillo, P. E. J.; Tancret, F. Martensite formation in titanium alloys: Crystallographic and compositional effects. Journal of Alloys and Compounds 872 (2021), 159636. https://doi.org/10.1016/j.jallcom.2021.159636

11. Bocchetta, P.; Chen, L.-Y.; Tardelli, J. D. C.; dos Reis, A. C.; Almeraya-Calderón, F.; Leo, P. Passive layers and corrosion resistance of biomedical Ti-6Al-4V and β-Ti alloys. Coatings 11(5) (2021), 487. https://doi.org/10.3390/coatings11050487

12. Brumbauer, F.; Okamoto, N. L.; Ichitsubo, T.; Sprengel, W.; Luckabauer, M. Minor additions of Sn suppress the omega phase formation in beta titanium alloys. Acta Materialia 262 (2024), 119466. https://doi.org/10.1016/j.actamat.2023.119466

13. Cao, W.; Chen, S.-L.; Zhang, F.; Wu, K.; Yang, Y.; Chang, Y. A.; Schmid-Fetzer, R.; Oates, W. A. PANDAT software with PanEngine, PanOptimizer and PanPrecipitation for multi-component phase diagram calculation and materials property simulation. Calphad 33(2) (2009), 328–

342.
https://doi.org/10.1016/j.calphad.2008.08.004

14. Cardoso, G. C.; de Almeida, G. S.; Corrêa, D. O. G.; Zambuzzi, W. F.; Buzalaf, M. A. R.; Correa, D. R. N.; Grandini, C. R. Preparation and characterization of novel as-cast Ti-Mo-Nb alloys for biomedical applications. Scientific Reports 12 (2022). https://doi.org/10.1038/s41598-022-14820-8

15. Cawse, J. N. Experimental strategies for combinatorial and high-throughput materials development. Accounts of Chemical Research 34(3) (2001), 213–221. https://doi.org/10.1021/ar000117s

16. Chen, L.; Tong, Z.; Luo, H.; Qu, Y.; Gu, X.; Si, M. Titanium particles in peri-implantitis: distribution, pathogenesis and prospects. International Journal of Oral Science 15(1) (2023), 49. https://doi.org/10.1038/s41368-023-00256-x

17. Chen, N.; Kou, H.; Wu, Z.; Qiang, F.; Wang, C.; Li, J.; Molina-Aldareguia, J. M. Stress-induced α″ martensitic phase transformation and martensitic twinning in a metastable β titanium alloy. Journal of Alloys and Compounds 859 (2021), 157809. https://doi.org/10.1016/j.jallcom.2020.157809

18. Chen, Z.; Liu, Y.; Jiang, H.; Liu, M.; Wang, C. H.; Cao, G. H. Microstructures and mechanical properties of Mn modified, Ti-Nb-based alloys. Journal of Alloys and Compounds 723 (2017), 1091–1097. https://doi.org/10.1016/j.jallcom.2017.06.311

19. Cheng, Y.-T.; Cheng, C.-M. Relationships between hardness, elastic modulus, and the work of indentation. Applied Physics Letters 73(5) (1998), 614–616. https://doi.org/10.1063/1.121873

20. Chmielewska, A.; Dean, D. The role of stiffness-matching in avoiding stress shielding-induced bone loss and stress concentration-induced skeletal reconstruction device failure. Acta Biomaterialia 173 (2024), 51–65. https://doi.org/10.1016/j.actbio.2023.11.011

21. Christian, J. W.; Mahajan, S. Deformation twinning. Progress in Materials Science 39(1–2) (1995), 1–157. https://doi.org/10.1016/0079-6425(94)00007-7

22. Cotton, J. D.; Briggs, R. D.; Boyer, R. R.; Tamirisakandala, S.; Russo, P.; Shchetnikov, N.; Fanning, J. C. State of the art in beta titanium alloys for airframe applications. JOM 67(6) (2015), 1281–1303. https://doi.org/10.1007/s11837-015-1442-4

23. Ding, C.; Liu, C.; Zhang, L.; Wu, D.; Liu, L. Design of low-cost and high-strength titanium alloys using pseudo-spinodal mechanism through diffusion couple technology and CALPHAD. Materials 14(11) (2021), 2910. https://doi.org/10.3390/ma14112910

24. Eliaz, N. Corrosion of metallic biomaterials: A review. Materials 12(3) (2019), 407. https://doi.org/10.3390/ma12030407

25. Emelianova, E.; Pisarev, M.; Balokhonov, R.; Romanova, V. Crystal plasticity simulations of dislocation slip and twinning in α-Ti single and polycrystals. Metals 15(11) (2025), 1243. https://doi.org/10.3390/met15111243

26. Fan, J. Microstructural study of the β→α phase transformation induced by thermo-mechanical treatments in metastable β Ti-5553 alloy. PhD dissertation. Université de Lorraine (2016). https://doi.org/10.70675/961c3a21z1c71z494bz95e0zb603ebf7d453

27. Farrokhi, A. Titanium and its alloys. In: Bălțatu, M. S.; Vizureanu, P. (Eds.), Titanium Alloys – Research and Future Trends. IntechOpen (2026). https://doi.org/10.5772/intechopen.1010907

28. Fitzner, A.; Prakash, D. G. L.; da Fonseca, J. Q.; Thomas, M.; Zhang, S.-Y.; Kelleher, J.; Manuel, P.; Preuss, M. The effect of aluminium on twinning in binary alpha-titanium. Acta Materialia 103 (2016), 341–351. https://doi.org/10.1016/j.actamat.2015.09.048

29. Fratila, A.; Jiménez-Marcos, C.; Mirza-Rosca, J.; Saceleanu, A. Mechanical properties and biocompatibility of various cobalt chromium dental alloys. Materials Chemistry and Physics (2023), 127867. https://doi.org/10.1016/j.matchemphys.2023.127867

30. Frost, H. M. Wolff's law and bone's structural adaptations to mechanical usage: an overview for clinicians. The Angle Orthodontist 64(3) (1994), 175–188. https://doi.org/10.1043/0003-3219(1994)064<0175:WLABSA>2.0.CO;2

31. Fu, Y.; Gao, Y.; Jiang, W.; Xiao, W.; Zhao, X.; Ma, C. A review of deformation mechanisms, compositional design, and development of titanium alloys with transformation-induced plasticity and twinning-induced plasticity effects. Metals 14(1) (2024), 97. https://doi.org/10.3390/met14010097

32. Fukuhara, M.; Sanpei, A. Elastic moduli and internal frictions of Inconel 718 and Ti-6Al-4V as a function of temperature. Journal of Materials Science Letters 12(14) (1993), 1122–1124. https://doi.org/10.1007/BF00420541

33. Gao, F.; Zhang, W.; Liu, X.; Luo, X.; Wang, Z.; Li, N.; Liu, L. Review: Recent progress in titanium alloys development via machine learning and high-throughput preparation. Journal of Materials Science 60(37) (2025), 16655–16683. https://doi.org/10.1007/s10853-025-11441-0

34. Gaur, S.; Agnihotri, R.; Albin, S. Bio-tribocorrosion of titanium dental implants and its toxicological implications: A scoping review. The Scientific World Journal 2022 (2022), 1–15. https://doi.org/10.1155/2022/4498613

35. Golesorkhtabar, R.; Pavone, P.; Spitaler, J.; Puschnig, P.; Draxl, C. ElaStic: A tool for calculating second-order elastic constants from first principles. Computer Physics Communications 184 (2013), 1861–1873. https://doi.org/10.1016/j.cpc.2013.03.010

36. Gomes, C. C.; Moreira, L. M.; Santos, V. J. S. V.; Ramos, A. S.; Lyon, J. P.; Soares, C. P.; Santos, F. V. Assessment of the genetic risks of a metallic alloy used in medical implants. Genetics and Molecular Biology 34(1) (2011), 116–121. https://doi.org/10.1590/s1415-47572010005000118

37. Hermann, A.; Kurzydłowski, D. First-principles prediction of structures and properties in crystals. Crystals 9(9) (2019), 463. https://doi.org/10.3390/cryst9090463

38. Huzum, B.; Puha, B.; Necoara, R. M.; Gheorghevici, S.; Puha, G.; Filip, A.; Sirbu, P. D.; Alexa, O. Biocompatibility assessment of biomaterials used in orthopedic devices: An overview. Experimental and Therapeutic Medicine 22(5) (2021), 1315. https://doi.org/10.3892/etm.2021.10750

39. Ikehata, H.; Nagasako, N.; Furuta, T.; Fukumoto, A.; Miwa, K.; Saito, T. First-principles calculations for development of low elastic modulus Ti alloys. Physical Review B 70(17) (2004). https://doi.org/10.1103/physrevb.70.174113

40. Irimescu, R. E.; Raducanu, D.; Nocivin, A.; Cojocaru, E. M.; Cojocaru, V. D.; Zarnescu-Ivan, N. Optimizing suitable mechanical properties for a biocompatible beta-titanium alloy by combining plastic deformation with solution treatment. Materials 17(23) (2024), 5828. https://doi.org/10.3390/ma17235828

41. Karre, R.; Niranjan, M. K.; Dey, S. R. First principles theoretical investigations of low Young's modulus beta Ti–Nb and Ti–Nb–Zr alloys compositions for biomedical applications. Materials Science and Engineering: C 50 (2015), 52–58. https://doi.org/10.1016/j.msec.2015.01.061

42. Kattner, U. R. The CALPHAD method and its role in material and process development. Tecnologia em Metalurgia Materiais e Mineração 13(1) (2016), 3–15. https://doi.org/10.4322/2176-1523.1059

43. Kattner, U. R. The need for reliable data in computational thermodynamics. High Temperatures–High Pressures 49(1–2) (2020), 31–47. https://doi.org/10.32908/hthp.v49.853

44. Keppens, V. Structure of materials: An introduction to crystallography, diffraction, and symmetry. The Journal of the Acoustical Society of America 124(3) (2008), 1385–1386. https://doi.org/10.1121/1.2953315

45. Kolli, R. P.; Devaraj, A. A review of metastable beta titanium alloys. Metals 8(7) (2018), 506. https://doi.org/10.3390/met8070506

46. Korkmaz, H. E.; Erdoğan, M. The effects of different beta stabilizers on the mechanical and thermal properties of titanium alloys. Journal of Alloys and Compounds 1064 (2026), 187899. https://doi.org/10.1016/j.jallcom.2026.187899

47. Kotsakis, G.; Xie, L.; Siddiqui, D. A.; Daubert, D.; Graham, D. J.; Gil, F. J. Dynamic assessment of titanium surface oxides following mechanical damage reveals only partial passivation under inflammatory conditions. npj Materials Degradation 8 (2024). https://doi.org/10.1038/s41529-024-00514-1

48. Koul, M. K.; Breedis, J. F. Phase transformations in beta isomorphous titanium alloys. Acta Metallurgica 18(6) (1970), 579–588. https://doi.org/10.1016/0001-6160(70)90087-8

49. Kroupa, A. Modelling of phase diagrams and thermodynamic properties using CALPHAD method – Development of thermodynamic databases. Computational Materials Science 66 (2013), 3–13. https://doi.org/10.1016/j.commatsci.2012.02.003

50. Kuroda, P. A. B.; Lourenço, M. L.; Correa, D. R. N.; Grandini, C. R. Thermomechanical treatments influence on the phase composition, microstructure, and selected mechanical properties of Ti–20Zr–Mo alloys system for biomedical applications. Journal of Alloys and Compounds 812 (2020), 152108. https://doi.org/10.1016/j.jallcom.2019.152108

51. Lee, C. M.; Ju, C. P.; Chern Lin, J. H. Structure–property relationship of cast Ti–Nb alloys. Journal of Oral Rehabilitation 29(4) (2002), 314–322. https://doi.org/10.1046/j.1365-2842.2002.00825.x

52. Leyens, C.; Peters, M., eds. Titanium and titanium alloys: fundamentals and applications. Wiley-VCH: Weinheim, Germany, 2006. https://doi.org/10.1002/3527602119

53. Li, P.; Tong, X.; Wang, Y. Microstructural and mechanical properties of β-type Ti–Mo–Nb biomedical alloys with low elastic modulus. Journal of Alloys and Compounds (2020),

152412.
https://doi.org/10.1016/j.jallcom.2019.152412

54. Li, S.; Kim, J. H.; Kang, S. W.; Kim, J. H.; Nam, T.-H.; Yeom, J.-T. Superelastic metastable Ti-Mo-Sn alloys with high elastic admissible strain for potential bio-implant applications. Journal of Materials Science & Technology 163 (2023), 45–58. https://doi.org/10.1016/j.jmst.2023.01.061

55. Liang, S. Review of the design of titanium alloys with low elastic modulus as implant materials. Advanced Engineering Materials 22(11) (2020), 2000555. https://doi.org/10.1002/adem.202000555

56. Limzider, N.; Rittel, D.; Shemtov-Yona, K. Bone morphology and mechanical behavior: New insights into cortical and trabecular failure under compression. Journal of the Mechanical Behavior of Biomedical Materials (2025), 107214. https://doi.org/10.2139/ssrn.5239869

57. Liu, X.; Xu, P.; Zhao, J.; Lu, W.; Li, M.; Wang, G. Material machine learning for alloys: Applications, challenges and perspectives. Journal of Alloys and Compounds 921 (2022), 165984.
https://doi.org/10.1016/j.jallcom.2022.165984

58. Liu, Y. H.; Hu, Z. H.; Suo, Z. G.; Hu, L. Z.; Feng, L. Y.; Gong, X. Q.; Liu, Y.; Zhang, J. C. High-throughput experiments facilitate materials innovation: A review. Science China Technological Sciences 62(4) (2019), 521–545. https://doi.org/10.1007/s11431-018-9369-9

59. Liu, Z.; Zhang, H.; Zhang, S.; Cheng, J.; He, Y.; Zhou, G.; Liu, J.; Song, S.; Chen, L. A machine learning method approach for designing novel high strength and plasticity metastable β titanium alloys. Progress in Natural Science: Materials International 35(1) (2025), 156–165.

60. Lu, S.; et al. Phase transformation induced twinning in commercially pure titanium: An in-situ study. Scripta Materialia 229 (2023), 115350. https://doi.org/10.1016/j.scriptamat.2023.115350

61. Luo, J.; Jia, X.; Gu, R.; Zhou, P.; Huang, Y.-J.; Sun, J.; Yan, M. 316L stainless steel manufactured by selective laser melting and its biocompatibility with or without hydroxyapatite coating. Metals 8(7) (2018), 548. https://doi.org/10.3390/met8070548

62. Lütjering, G.; Williams, J. C. Fundamental aspects. In: Titanium. Springer, Berlin, Heidelberg (2003), 13–50. https://doi.org/10.1007/978-3-540-71398-2_2

63. Manojlović, V. D.; Marković, G. Titanium alloys database for medical applications. Metallurgical and Materials Data 1(1) (2023), 1–6. https://doi.org/10.30544/mmd5

64. Manojlović, V. D.; Marković, G. Titanium alloys database for medical applications. Zenodo (2023). https://doi.org/10.5281/zenodo.7802694

65. Marin, E.; Lanzutti, A. Biomedical applications of titanium alloys: a comprehensive review. Materials 17(1) (2023), 114. https://doi.org/10.3390/ma17010114

66. Marin, E.; Lanzutti, A. History of metallic orthopedic materials. Metals 15(4) (2025), 378.
https://doi.org/10.3390/met15040378

67. Marković, G.; Dominguez-Gutierrez, F. J. Thermally activated plasticity in single-crystal titanium: a molecular dynamics study of nanoscale deformation. Modelling and Simulation in

Materials Science and Engineering 34(1) (2026), 015018. https://doi.org/10.1088/1361-651x/ae2f77

68. Marković, G.; Manojlović, V.; Ružić, J.; Sokić, M. Predicting low-modulus biocompatible titanium alloys using machine learning. Materials 16(19) (2023), 6355. https://doi.org/10.3390/ma16196355

69. Marković, G.; Ruzic, J.; Sokic, M.; Milojkov, D.; Manojlovic, V. D. Prediction of elastic modulus, yield strength, and tensile strength in biocompatible titanium alloys. Journal of Mining and Metallurgy, Section B: Metallurgy 60(2) (2024), 273–282. https://doi.org/10.2298/jmmb240221019m

70. Martins Junior, J. R. S.; Kuroda, P. A. B.; Grandini, C. R. Investigation of the chemical composition, microstructure, density, microhardness, and elastic modulus of the new β Ti-50Nb-xMo alloys for biomedical applications. Materials 17(1) (2024), 250. https://doi.org/10.3390/ma17010250

71. McQuillan, A. D. Allotropic transformations in titanium. Nature 164(4157) (1949), 24–24.
https://doi.org/10.1038/164024a0

72. Mendelev, M. I.; Underwood, T. L.; Ackland, G. J. Development of an interatomic potential for the simulation of defects, plasticity, and phase transformations in titanium. The Journal of Chemical Physics 145(15) (2016), 154102. https://doi.org/10.1063/1.4964654

73. Mohapatra, N. C.; Rana, R.; Sahoo, S. K. Evolution of metals and alloys in orthopedics with their relevance in osteoporosis. Indian Journal of Orthopaedics 59(3) (2025), 271–279. https://doi.org/10.1007/s43465-025-01344-2

74. Molchanova, E. K.; Glazunov, S. G. Phase diagrams of titanium alloys (1965).

75. Morinaga, M.; Yukawa, N.; Maya, T.; Sone, K.; Adachi, H. Theoretical design of titanium alloys. In: Proceedings of the Sixth World Conference on Titanium, France (1988).

76. Niinomi, M. Biologically and mechanically biocompatible titanium alloys. Materials Transactions 49(10) (2008), 2170–2178. https://doi.org/10.2320/matertrans.l-mra2008828

77. Niinomi, M.; Nakai, M. Titanium-based biomaterials for preventing stress shielding between implant devices and bone. International Journal of Biomaterials 2011(1) (2011), 836587. https://doi.org/10.1155/2011/836587

78. Niu, Y.; Hong, Z.-Q.; Wang, Y.-Q.; Zhu, Y.-C. Machine learning-based beta transus temperature prediction for titanium alloys. Journal of Materials Research and Technology 23 (2023), 515–529.
https://doi.org/10.1016/j.jmrt.2023.01.019

79. Nnamchi, P. S.; Obayi, C. S. Self-healing in titanium alloys: A materials science perspective. In: Advanced Functional Materials. IntechOpen (2020). https://doi.org/10.5772/intechopen.92348

80. Oliveira, N.; Guastaldi, A. C. Electrochemical stability and corrosion resistance of Ti-Mo alloys for biomedical applications. Acta Biomaterialia 5(1) (2008), 399–405. https://doi.org/10.1016/j.actbio.2008.07.010

81. Oliver, W. C.; Pharr, G. M. An improved technique for determining hardness and elastic modulus using load and displacement sensing indentation experiments. Journal of Materials Research 7(6) (1992), 1564–1583. https://doi.org/10.1557/JMR.1992.1564

82. Oliver, W. C.; Pharr, G. M. Measurement of hardness and elastic modulus by instrumented indentation: Advances in understanding and refinements to methodology. Journal of

Materials Research 19(1) (2004), 3–20. https://doi.org/10.1557/jmr.2004.19.1.3

83. Pathak, S.; Kalidindi, S. R. Spherical nanoindentation stress–strain curves. Materials Science and Engineering: R: Reports 91 (2015), 1–36. https://doi.org/10.1016/j.mser.2015.02.001

84. Paul, A. R.; Mehla, S.; Mazur, M.; Brandt, M.; Choong, P.; Bhargava, S. K. Reimagining orthopaedic implants: Mechanobiochemical innovations to overcome stress shielding. Progress in Materials Science 160 (2026), 101682. https://doi.org/10.1016/j.pmatsci.2026.101682

85. Perrut, M. Thermodynamic modeling by the CALPHAD method and its applications to innovative materials. Aerospace Lab 9 (2015), p-1. https://doi.org/10.12762/2015.AL09.10

86. Pesode, P.; Barve, S. A review—metastable β titanium alloy for biomedical applications. Journal of Engineering and Applied Science 70(1) (2023), 25. https://doi.org/10.1186/s44147-023-00196-7

87. Quan, G.-Z.; Wang, X.; Li, Y.-L.; Zhang, L. Analytical descriptions of dynamic softening mechanisms for Ti-13Nb-13Zr biomedical alloy in single phase and two phase regions. Archives of Metallurgy and Materials 62(4) (2017), 2029–2043. https://doi.org/10.1515/amm-2017-0302

88. Raabe, D.; Sander, B.; Friák, M.; Ma, D.; Neugebauer, J. Theory-guided bottom-up design of β-titanium alloys as biomaterials based on first principles calculations: Theory and experiments. Acta Materialia 55(13) (2007), 4475–4487. https://doi.org/10.1016/j.actamat.2007.04.024

89. Rabadia, C. D.; Jawed, S. F.; Wang, J.; Siddhpura, M.; Siddhpura, A. Revised semiempirical approach to predict the occurrence of twinning in titanium alloys. ACS Omega 6(49) (2021), 34056–34064. https://doi.org/10.1021/acsomega.1c05474

90. Ramprasad, R.; Batra, R.; Pilania, G.; Mannodi-Kanakkithodi, A.; Kim, C. Machine learning in materials informatics: recent applications and prospects. npj Computational Materials 3(1) (2017). https://doi.org/10.1038/s41524-017-0056-5

91. Ratner, Buddy D. "A perspective on titanium biocompatibility." In Titanium in medicine: Material science, surface science, engineering, biological responses and medical applications, pp. 1-12. Berlin, Heidelberg: Springer Berlin Heidelberg, 2001.

92. Reddy, N. S.; Choi, H. J.; Bo Young, H. Practical model for predicting beta transus temperature of titanium alloys. Korean Journal of Materials Research 24(7) (2014), 381–387. https://doi.org/10.3740/mrsk.2014.24.7.381

93. Ren, Y.; Xu, J.; Wei, Y.; Liu, Y.; Zhu, J.; Liu, S. Effect of interstitial oxygen on the microstructure and mechanical properties of titanium alloys: A review. Crystals 15(7) (2025), 618. https://doi.org/10.3390/cryst15070618

94. Ruzic, J.; Emura, S.; Ji, X.; Watanabe, I. Mo segregation and distribution in Ti–Mo alloy investigated using nanoindentation. Materials Science and Engineering: A 718 (2018), 48–55. https://doi.org/10.1016/j.msea.2018.01.098

95. Sarraf, M.; Ghomi, E. R.; Alipour, S.; Ramakrishna, S.; Sukiman, N. L. A state-of-the-art review of the fabrication and characteristics of titanium and its alloys for biomedical applications. Bio-Design and Manufacturing 5(2) (2022). https://doi.org/10.1007/s42242-021-00170-3

96. Seagle, S. R. Titanium processing. Encyclopedia Britannica (2019). https://www.britannica.com/technology/titanium-processing Accessed 2 May 2026

97. Shang, G.; Gan, X.; Wang, X.; Ge, J.; Li, C.; Zhu, Z.; Zhang, X.; Zhou, K. Effect of cooling rate on α variant selection and microstructure evolution in TB17 titanium alloy. Materials 17(20) (2024), 5010. https://doi.org/10.3390/ma17205010

98. Shemtov-Yona, K.; Miara, Y.; Rittel, D. Investigating the integrity of titanium-oxide nanolayers of Ti6Al4V under chemo-mechanical stress. Dental Materials (2025). https://doi.org/10.1016/j.dental.2025.10.014

99. Siemers, C.; Bäker, M.; Brunke, F.; Wolter, D.; Sibum, H. Aluminum- and vanadium-free titanium alloys for application in medical engineering. In: Titanium in Medical and Dental Applications. Woodhead Publishing (2018), 477–492. https://doi.org/10.1016/B978-0-12-812456-7.00021-4

100. Sivakumar, T.; Chandrasekaran, K.; Sridhar, C.; Tharanikumar, N. Titanium alloys and their disadvantages in medical and dental implants. In: Titanium Alloys – Research and Future Trends. IntechOpen (2026). https://doi.org/10.5772/intechopen.1010633

101. Smith, D.; Pickett, P.; Grabowski, T.; Thorpe, J.; Azarmi, F. Mechanical properties of cobalt chromium alloy manufactured by direct energy deposition technology. Journal of Thermal Spray Technology 34 (2024), 674–689. https://doi.org/10.1007/s11666-024-01913-1

102. Sosa, J. M.; Huber, D. E.; Welk, B.; Fraser, H. L. Development and application of MIPAR™: A novel software package for two- and three-dimensional microstructural characterization. Integrating Materials and Manufacturing Innovation 3(1) (2014), 123–140. https://doi.org/10.1186/2193-9772-3-10

103. Spataru, M. C.; Baltatu, M. S.; Sandu, A. V.; Vizureanu, P. General trends on biomaterials applications: advantages and limitations. In: Novel Biomaterials for Tissue Engineering. IntechOpen (2024). https://doi.org/10.5772/intechopen.114838

104. Stráský, J.; et al. Increasing strength of a biomedical Ti-Nb-Ta-Zr alloy by alloying with Fe, Si and O. Journal of the Mechanical Behavior of Biomedical Materials 71 (2017), 329–336. https://doi.org/10.1016/j.jmbbm.2017.03.026

105. Stukowski, A. Visualization and analysis of atomistic simulation data with OVITO–the Open Visualization Tool. Modelling and Simulation in Materials Science and Engineering 18(1) (2010), 015012. https://doi.org/10.1088/0965-0393/18/1/015012

106. Tane, M.; Akita, S.; Nakano, T.; Hagihara, K.; Umakoshi, Y.; Niinomi, M.; Nakajima, H. Peculiar elastic behavior of Ti–Nb–Ta–Zr single crystals. Acta Materialia 56(12) (2008), 2856–2863. https://doi.org/10.1016/j.actamat.2008.02.017

107. Tane, M.; et al. Low Young's modulus in Ti–Nb–Ta–Zr–O alloys: Cold working and oxygen effects. Acta Materialia 59(18) (2011), 6975–6988. https://doi.org/10.1016/j.actamat.2011.07.050

108. Thompson, A. P.; Aktulga, H. M.; Berger, R.; Bolintineanu, D. S.; Brown, W. M.; Crozier, P. S.; in 't Veld, P. J.; Kohlmeyer, A.; Moore, S. G.; Nguyen, T. D.; Shan, R.; Stevens, M. J.; Tranchida, J.; Trott, C.; Plimpton, S. J. LAMMPS - a flexible simulation tool for particle-based materials modeling at the atomic, meso, and continuum scales. Computer Physics Communications

271 (2022), 108171. https://doi.org/10.1016/j.cpc.2021.108171

109. Tiwari, G. P.; Ramanujan, R. V. The relation between the electron to atom ratio and some properties of metallic systems. Journal of Materials Science 36(2) (2001), 271–283. https://doi.org/10.1023/a:1004853304704

110. Tsuchiya, H.; Miyabe, S.; Doi, K.; Fujimoto, S. Corrosion resistance of titanium. Journal of The Surface Finishing Society of Japan 73 (2022), 33–38. https://doi.org/10.4139/sfj.73.33

111. Vaiani, L.; Boccaccio, A.; Uva, A. E.; Palumbo, G.; Piccininni, A.; Guglielmi, P.; Cantore, S.; Santacroce, L.; Charitos, I. A.; Ballini, A. Ceramic materials for biomedical applications: an overview on properties and fabrication processes. Journal of Functional Biomaterials 14(3) (2023), 146.
https://doi.org/10.3390/jfb14030146

112. van Mourik, T.; Bühl, M.; Gaigeot, M.-P. Density functional theory across chemistry, physics and biology. Philosophical Transactions of the Royal Society A: Mathematical, Physical and Engineering Sciences 372(2011) (2014), 20120488. https://doi.org/10.1098/rsta.2012.0488

113. Vecchio, K. S.; Dippo, O. F.; Kaufmann, K. R.; Liu, X. High-throughput rapid experimental alloy development (HT-READ). Acta Materialia 221 (2021), 117352. https://doi.org/10.1016/j.actamat.2021.117352

114. Wang, Q.; Dong, C.; Liaw, P. K. Structural stabilities of β-Ti alloys studied using a new Mo equivalent derived from [β/(α + β)] phase-boundary slopes. Metallurgical and Materials Transactions A 46(8) (2015), 3440–3447. https://doi.org/10.1007/s11661-015-2923-3

115. Wang, Z.; Chen, A.; Tao, K.; Cai, J.; Han, Y.; Gao, J.; Ye, S.; Wang, S.; Ali, I.; Li, J. AlphaMat: a material informatics hub connecting data, features, models and applications. npj Computational Materials 9(1) (2023). https://doi.org/10.1038/s41524-023-01086-5

116. Wheelis, S. E.; Wilson, T. G. Jr.; Valderrama, P.; Rodrigues, D. C. Surface characterization of titanium implant healing abutments before and after placement. Clinical Implant Dentistry and Related Research 20(2) (2018), 180–190. https://doi.org/10.1111/cid.12566

117. Wu, C.-T.; Chang, H.-T.; Wu, C.-Y.; Chen, S.-W.; Huang, S.-Y.; Huang, M.; Pan, Y.-T.; Bradbury, P.; Chou, J.; Yen, H.-W. Machine learning recommends affordable new Ti alloy with bone-like modulus. Materials Today 34 (2020), 41–50. https://doi.org/10.1016/j.mattod.2019.08.008

118. Zhang, Y.; Xue, D.; Xin, S.; Wang, X.; Zhou, W.; Pan, X.; Li, X.; Zhang, B.; Hao, M. Research progress of machine learning aided titanium alloys design. Materials China 44(4) (2025), 319–329.
https://doi.org/10.7502/j.issn.1674-3962.202501004

119. Zhao, G.; Xu, X.; Dye, D.; Rivera-Díaz-del-Castillo, P. E. J.; Petrinic, N. Facile route to implement transformation strengthening in titanium alloys. Scripta Materialia 208 (2022), 114362. https://doi.org/10.1016/j.scriptamat.2021.114362

120. Zhao, J.; Liu, K.; Ding, M.; Yin, L.; Liang, S. Relationship between the composition and elastic modulus of TiZrTa alloys for implant materials. Metals 12(10) (2022), 1582. https://doi.org/10.3390/met12101582

121. Zhou, Y. B. Titanium alloy casting (2000). https://doi.org/10.31399/asm.hb.v15.a0005337

122. Zhou, Y.-L.; Luo, D.-M. Microstructures and mechanical properties of Ti–Mo alloys cold-rolled and heat treated. Materials Characterization 62(10) (2011), 931–937. https://doi.org/10.1016/j.matchar.2011.07.010

123. Žitňanský, M.; Čaplovič, L. Effect of the thermomechanical treatment on the structure of titanium alloy Ti6Al4V. Journal of Materials Processing Technology 157–158 (2004), 643–649. https://doi.org/10.1016/j.jmatprotec.2004.07.151

124. Zou, C.; Li, J.; Wang, W. Y.; Zhang, Y.; Lin, D.; Yuan, R.; Wang, X.; Tang, B.; Wang, J.; Gao, X.; Kou, H.; Hui, X.; Zeng, X.; Qian, M.; Song, H.; Liu, Z.-K.; Xu, D. Integrating data mining and machine learning to discover high-strength ductile titanium alloys. Acta Materialia 202 (2021), 211–221.
https://doi.org/10.1016/j.actamat.2020.10.056

Biography

Gordana Marković was born on April 21, 1997, in Belgrade, Serbia. She enrolled at the Faculty of Technology and Metallurgy, University of Belgrade, in the 2016/17 academic year and graduated in 2021 from the Materials Engineering study program with an average grade of 8.75. She completed her Master's studies in Metallurgical Engineering at the same faculty in 2022 with an average grade of 10.00. In the 2022/23 academic year, she enrolled in PhD studies in Metallurgical Engineering and passed all examinations required by the doctoral program with an average grade of 10.00.

Since November 2022, she has been employed at the Institute for Technology of Nuclear and Other Mineral Raw Materials (ITNMS), Belgrade, where she currently holds the position of Research Assistant. Her research focuses on the application of machine learning and molecular dynamics simulations for the design, characterization, and optimization of titanium alloys and other advanced metallic materials.

During her doctoral studies, she completed research internships at the University of Lorraine in France and the National Centre for Nuclear Research in Poland, where she worked on scientific knowledge extraction using artificial intelligence and atomistic simulations of metallic materials. She actively participates in international research collaborations and is a member of the COST Actions EuMINe, MecaNano, and EU-MACE.

She is a member of the Serbian Metallurgical Society and the organizing committee of the 6th Metallurgical & Materials Engineering Congress of South-East Europe. She is the author and co-author of several scientific papers published in international journals and conference proceedings. In 2025, she received the Second Prize – Best Student Paper Award at the BECCSI Conference in Belgrade.

She actively uses Python, VASP, and LAMMPS in her research and is fluent in English, with working knowledge of Spanish.

List of Publications Used in the Dissertation:

1. Manojlović VD; **Marković G**. *Titanium Alloys Database for Medical Applications*. Metallurgical and Materials Data. 1(1) (2023), 1–6. DOI: 10.30544/mmd5

2. **Marković G**; Manojlović V; Ružić J; Sokić M. *Predicting Low-Modulus Biocompatible Titanium Alloys Using Machine Learning*. Materials. 16(19) (2023), 6355. DOI: 10.3390/ma16196355

3. **Marković G**; Ružić J; Sokić M; Milojkov D; Manojlović VD. *Prediction of elastic modulus, yield strength, and tensile strength in biocompatible titanium alloys*. Journal of Mining and Metallurgy, Section B: Metallurgy. 60(2) (2024), 273–282. DOI: 10.2298/JMMB240221019M

4. **Marković G**; Dominguez-Gutierrez FJ. *Thermally activated plasticity in single-crystal titanium: a molecular dynamics study of nanoscale deformation*. Modelling and Simulation in Materials Science and Engineering. 34(1) (2026), 015018. DOI: 10.1088/1361-651X/AE2F77

Прилог 1

Изјава о ауторству

Име и презиме аутора Гордана Марковић

Број индекса 2022/4012

Изјављујем

да је докторска дисертација под насловом

Развој и дизајн нових легура титана применом напредних рачунарских метода

Development and design of new titanium alloys using advanced computational methods

- резултат сопственог истраживачког рада;
- да дисертација у целини ни у деловима није била предложена за стицање друге дипломе према студијским програмима других високошколских установа;
- да су резултати коректно наведени и
- да нисам кршио/ла ауторска права и користио/ла интелектуалну својину других лица.

Потпис аутора

У Београду, _____

_____

Прилог 2.

Изјава о истоветности штампане и електронске верзије докторског рада

Име и презиме аутора Гордана Марковић

Број индекса 2022/4012

Студијски програм металуршко инжењерство

Наслов рада Развој и дизајн нових легура титана применом напредних рачунарских метода

Development and design of new titanium alloys using advanced computational methods

Ментор Др Васо Манојловић, ванредни професор Технолошко-металуршког факултета, Универзитета у Београду и Др Јована Ружић, виша научна сарадница Института за нуклеарне науке „Винча“, Института од националног значаја за Републику Србију, Универзитета у Београду

Изјављујем да је штампана верзија мог докторског рада истоветна електронској верзији коју сам предао/ла ради похрањена у **Дигиталном репозиторијуму Универзитета у Београду.**

Дозвољавам да се објаве моји лични подаци везани за добијање академског назива доктора наука, као што су име и презиме, година и место рођења и датум одбране рада.

Ови лични подаци могу се објавити на мрежним страницама дигиталне библиотеке, у електронском каталогу и у публикацијама Универзитета у Београду.

Потпис аутора

У Београду, _____

_____

Прилог 3

Изјава о коришћењу

Овлашћујем Универзитетску библиотеку „Светозар Марковић“ да у Дигитални репозиторијум Универзитета у Београду унесе моју докторску дисертацију под насловом:

Развој и дизајн нових легура титана применом напредних рачунарских метода

Development and design of new titanium alloys using advanced computational methods

која је моје ауторско дело.

Дисертацију са свим прилозима предао/ла сам у електронском формату погодном за трајно архивирање.

Моју докторску дисертацију похрањену у Дигиталном репозиторијуму Универзитета у Београду и доступну у отвореном приступу могу да користе сви који поштују одредбе садржане у одабраном типу лиценце Креативне заједнице (Creative Commons) за коју сам се одлучио/ла.

1. Ауторство (CC BY)

2. Ауторство – некомерцијално (CC BY-NC)

3. Ауторство – некомерцијално – без прерада (CC BY-NC-ND)

4. Ауторство – некомерцијално – делити под истим условима (CC BY-NC-SA)

5. Ауторство – без прерада (CC BY-ND)

6. Ауторство – делити под истим условима (CC BY-SA)

(Молимо да заокружите само једну од шест понуђених лиценци. Кратак опис лиценци је саставни део ове изјаве).

Потпис аутора

У Београду, _____

_____

1. **Ауторство**. Дозвољавате умножавање, дистрибуцију и јавно саопштавање дела, и прераде, ако се наведе име аутора на начин одређен од стране аутора или даваоца лиценце, чак и у комерцијалне сврхе. Ово је најслободнија од свих лиценци.

2. **Ауторство – некомерцијално**. Дозвољавате умножавање, дистрибуцију и јавно саопштавање дела, и прераде, ако се наведе име аутора на начин одређен од стране аутора или даваоца лиценце. Ова лиценца не дозвољава комерцијалну употребу дела.

3. **Ауторство – некомерцијално – без прерада**. Дозвољавате умножавање, дистрибуцију и јавно саопштавање дела, без промена, преобликовања или употребе дела у свом делу, ако се наведе име аутора на начин одређен од стране аутора или даваоца лиценце. Ова лиценца не дозвољава комерцијалну употребу дела. У односу на све остале лиценце, овом лиценцом се ограничава највећи обим права коришћења дела.

4. **Ауторство – некомерцијално – делити под истим условима**. Дозвољавате умножавање, дистрибуцију и јавно саопштавање дела, и прераде, ако се наведе име аутора на начин одређен од стране аутора или даваоца лиценце и ако се прерада дистрибуира под истом или сличном лиценцом. Ова лиценца не дозвољава комерцијалну употребу дела и прерада.

5. **Ауторство – без прерада**. Дозвољавате умножавање, дистрибуцију и јавно саопштавање дела, без промена, преобликовања или употребе дела у свом делу, ако се наведе име аутора на начин одређен од стране аутора или даваоца лиценце. Ова лиценца дозвољава комерцијалну употребу дела.

6. **Ауторство – делити под истим условима**. Дозвољавате умножавање, дистрибуцију и јавно саопштавање дела, и прераде, ако се наведе име аутора на начин одређен од стране аутора или даваоца лиценце и ако се прерада дистрибуира под истом или сличном лиценцом. Ова лиценца дозвољава комерцијалну употребу дела и прерада. Слична је софтверским лиценцама, односно лиценцама отвореног кода.